Developing a High-Flux Atomic Beam Source for Experiments with Ultracold Strontium Quantum Gases

Etienne Staub

München 2019

Entwicklung einer atomaren Quelle für Experimente mit ultrakalten Strontiumquantengasen

Masterarbeit an der Fakultät für Physik
Ludwig-Maximilians-Universität München

vorgelegt von

Etienne Staub

aus Göttingen

München, den 1. Oktober 2019

Abstract

In this thesis we design, build and test a new atomic source for experiments with ultracold strontium quantum gases. Our oven is heated by means of in-vacuum radiative heating, reaching temperatures in excess of 750 °C with a power consumption of 100 W. The oven features a detachable nozzle containing a hexagonal microcapillary array for the collimation of the atomic beam. Temperature gradients of more than 90 °C between the nozzle and the crucible are possible with a double layer of heat shields. We also report on the construction and optimization of a home-built linear external cavity diode laser operating at 461 nm, which we use to perform absorption spectroscopy on the atomic beam emerging from our oven.

Contents

List of Tables

List of Figures

Introduction

Ultracold quantum gases in optical lattices have allowed physicists to study a vast array of phenomena, ranging from the simulation of strongly correlated systems [1, 2] through Rydberg physics [3], topological phases of matter [4] and dipolar quantum gases [5] to optical clocks [6]. This has been possible due to the great degree of control afforded by optical lattices over parameters such as the interaction strength, the lattice potentials, the spin and the dimensionality of the system. The relatively recent development of single-site resolution using high numerical aperture objectives [7–9] further increases the versatility and precision of these experiments by enabling the direct observation of the previously mentioned phenomena [10].

Due to their favorable electronic transitions for laser cooling, the first of these experiments were conducted with alkaline atoms [1]. However, in recent years advances in atomic clocks have led to the emergence of alkaline earth atoms as an interesting class of atoms for experiments with optical lattices. These atoms exhibit a rich electronic structure with an extremely narrow intercombination line between their singlet and triplet states. This transition has allowed atomic clocks to reach unprecedented accuracies, with the newest generation reaching a measurement precision the order of 10^{-19} over a one hour averaging time, by using a degenerate Fermi gas of strontium trapped in a 3D optical lattice [11].

In our experiment we aim to combine alkaline earth metals in the form of strontium with optical lattices and single-site resolution for quantum simulation experiments. The appearance of tuneout wavelengths in strontium allow for the simulation of state-dependent physics [12, 13]. Furthemore, the fermionic isotope of strontium, ^{87}Sr, possesses a non-zero nuclear spin, leading to proposals of quantum simulations involving SU(N) symmetries [14].

All of these experiments suffer from limitations imposed by the duty cycle of the experimental sequence. In optical clocks the preparation and readout time of the atoms leads to a degradation of the clock stability in what is known as the Dick effect [15, 16], while new quantum simulation schemes, such as variational quantum simulation, require a high repetition rate [17]. One way of combating these problems is to increase the flux of usable atoms that can be trapped and cooled. As we will show, this requires an atomic source with excellent collimation properties and high-temperature capabilities.

Such atom sources, or ovens, have long been used commercially in molecular beam epitaxy and other vapor depositions schemes to grow semiconductors [18]. Usually, these commercially available ovens consist of a container with a hole through which atoms can

effuse when heat is applied. This results in a broad beam of atoms required for uniform crystal growth in large batches but poor collimating properties. The development of collimation via microchannel arrays [19] led to a more widespread use of these ovens in scientific research, including early versions of Cs atomic clocks [20, 21]. Meanwhile, several cold atom experiments have implemented ovens with microchannel arrays [22, 23]. An issue that has dogged many experiments working with such microchannel arrays has been the tendency of the capillaries to clog. This has also been a problem for our own experiment, where the appearance of clogging at our microchannels caused our atomic beam to become more divergent and thus reduced the flux of usable atoms. An additional problem posed by our oven is its short lifetime. Running at a standard operating temperature of 550 °C, our oven requires reloading every three to four months.

The aim of this thesis is to design, build and test a new oven that can generate a high flux of usable atoms for our experiment. Ideally, this new oven should also exhibit a longer lifetime than our current oven, as well as a simplified reloading procedure and reduced outgassing in vacuum via the use of a heat shield and in-vacuum water cooling. To test our oven we will build a diode laser at 461 nm in a linear external cavity configuration, which will allow us to perform absorption spectroscopy on the atoms effusing from our oven. This laser can also be used to provide the light for a 2D magneto-optical trap, which would further increase the efficiency of our oven by collimating the atomic beam and enhancing the flux of usable atoms. The 2D MOT could also be used to deviate the atomic beam so as to block any line-of-sight between the hot oven and our in-trap atoms. This would reduce the detrimental effect of black-body radiation of the in-trap lifetime of our atoms.

These two techniques are examples of the interaction of light and matter, which will be explored in Chapter 1 of this thesis. We then move on to discuss the expected results and of our absorption spectroscopy by means of a theoretical discussion of the characteristic properties of our atomic beam in Chapter 2. This discussion will allow us to derive an optimal set of parameters for our new oven which we can implement in its design and construction as described in Chapter 3. Having thus treated the matter aspect of our light-matter interaction, we will move on to the theory of lasers in Chapter 4, before reporting on the construction of our blue linear laser in Chapter 5. Finally, we will combine our oven and our laser to test the properties of our atomic beam in Chapter 6.

Chapter 1

Light-Matter Interaction

The characterization of our new oven is fundamentally reliant on the interaction between light and matter. In this opening chapter, we will explore some of the basic processes of light-matter interaction and their significance for our experiment. In particular, we will focus on absorption spectroscopy as the one of the simplest measurement technique for extracting information from atoms and magneto-optical traps as way to improve the efficiency of our oven. Our discussion of absorption spectroscopy will largely follow that of Ref.[24].

1.1 Absorption Spectroscopy

Much of the physics governing the behavior of an atom exposed to an electromagnetic field can be deduced by considering the following system. We imagine an electron of mass m_e bound to a much heavier nucleus of mass m_n via a Hookean spring with spring constant k. This will serve as our classical analog to an atom and is known as a Lorentz oscillator . The interaction of this atom with a monochromatic electromagnetic field of the form

$$E(t) = E_0 e^{-i\omega t}, \tag{1.1}$$

can then be modeled as a driven damped harmonic oscillator where the average position of the electron x, obeys the following equation of motion

$$\ddot{x} + \Gamma\dot{x} + \omega_0^2 x = -\frac{qE_0}{m} e^{-i\omega t}. \tag{1.2}$$

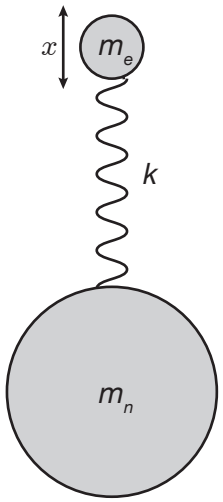

Figure 1.1 A schematic representation of the Lorentz oscillator model. An electron of mass m_e is tied to a nucleus of mass $m_n \gg m_e$ via a spring with spring constant k. The driving of this system by an external electric field leads to an oscillation of the average electron position x.

In the above equation we have used the fact
that $m_n \gg m_e$ to transform to center-of-mass coordinates, where we can work with the reduced electron mass $m = \frac{m_e m_n}{m_e + m_n}$. Together with the spring constant, the reduced mass defines the undamped angular frequency $\omega_0 = \sqrt{\frac{k}{m}}$ of the oscillator. The damping of the system is quantified by the constant Γ and represents the damping of the motion by the radiation. The factor q is the charge of the electron. To solve Eq. (1.2) we make the standard exponential Ansatz

$$x(t) = x_0 e^{-i\omega t}, \tag{1.3}$$

which leads to

$$x_0 = \frac{qE_0}{m} \frac{1}{\omega^2 - \omega_0^2 + i\Gamma\omega}. \tag{1.4}$$

Using this solution, we can quantify the response of our system to an applied electromagnetic field by introducing the polarizability

$$\alpha(\omega) = -q\frac{x_0}{E_0}, \tag{1.5}$$

which is a measure for the ease with which an electromagnetic field is able to induce a dipole moment in our system, that is to say, a separation of positive and negative charges. To understand the effect of the transmission of light through a medium consisting of a collection of Lorentz oscillators, we have to generalize from the microscopic quantity of polarizability to its macroscopic counterpart, the susceptibility $\chi(\omega)$. This is defined as

$$\chi(\omega) = \frac{n}{\epsilon_0}\alpha(\omega), \tag{1.6}$$

where n is the number of atoms per unit volume and ϵ_0 is the vacuum permittivity. The susceptibility allows us to determine the absorptivity of our medium which is a measure for the attenuation of light incident on the atoms and obeys the following differential equation

$$\frac{dI}{dz} = -aI \tag{1.7}$$

with an attenuation factor a, known as the absorption coefficient. This absorption coefficient is related to the imaginary part of the susceptibility according to

$$a(\omega) \propto \mathrm{Im}\left\{\frac{\chi(\omega)}{2}\right\} = \frac{\Gamma\omega}{\left(\omega^2 - \omega_0^2\right)^2 + \Gamma^2\omega^2}. \tag{1.8}$$

Close to the resonance frequency, $|\omega - \omega_0| \ll \omega_0$, and hence

$$\frac{\Gamma\omega}{\left(\omega^2 - \omega_0^2\right)^2 + \Gamma^2\omega^2} \approx \frac{1}{\Gamma\omega_0} \frac{\left(\frac{\Gamma}{2}\right)^2}{\left(\omega - \omega_0\right)^2 + \left(\frac{\Gamma}{2}\right)^2}. \tag{1.9}$$

Equation (1.9) describes a Lorentzian with a full width at half maximum (FWHM) of Γ. In an ideal scenario, we would expect to see just such a Lorenztian dip in the frequency of the transmitted light, centered at the resonance frequency of the atoms. However, as we will come to see, this spectrum is modified by certain real-world effects, such that a measurement of a Lorentzian spectrum requires significant effort.

1.1.1 Broadening Mechanisms

Doppler Broadening

An atom moving towards a counterpropagating electromagnetic wave with velocity $\mathbf{v}$, will see the frequency of the incoming light, ω, shifted by an amount $-\mathbf{k}\cdot\mathbf{v}$, such that its resonance frequency is given by

$$\omega_0 = \omega - \mathbf{k}\cdot\mathbf{v}, \tag{1.10}$$

where $\mathbf{k}$ is the wavevector of the incident field. To understand why this leads to a broadening of the observed absorption profile, we observe that the transmitted intensity of light is proportional to the density n of our medium via the absorption coefficient defined above. More specifically

$$I = I_0 e^{-a(\omega)z} = I_0 e^{-\sigma \int_0^L n(v)dv}, \tag{1.11}$$

where σ is the scattering cross-section of our atoms. Equation (1.11) is the solution to Equation (1.7) and is known as the Lambert-Beer law. As we will come to see in the following chapter, neither the density distribution nor the scattering cross-section is easily measured in the case of atoms exiting our oven. However, even without knowledge of the explicit form of σ and $n(v)$, it is clear to see that a distribution of velocities will lead to a distribution of frequencies according to Eq. (1.10) and thus a broadening of the absorption profile.

Transit-time Broadening

Another effect for us to consider is transit-time broadening. Atoms passing through our spectroscopy beam with waist w_0, with a velocity v perpendicular to the beam, will experience an electric field from the laser for a duration $T = \frac{w_0}{v}$. Given a laser beam with a Gaussian field distribution

$$E(t) = E_0 e^{-\frac{r}{w_0}^2} \cos(\omega_0 t), \tag{1.12}$$

where r is the radial distance to the center axis of the beam, the frequency spectrum of the transmitted light $\widetilde{E}(\omega)$, is given by the Fourier transform of Eq. (1.12). Since the

Fourier transform of a Gaussian is another Gaussian, we obtain for the measured intensity $I(\omega) = |\tilde{E}(\omega)|^2$:

$$I(\omega) \propto \exp\left[-\frac{w_0(\omega - \omega_0)}{2v\sqrt{2}}\right]. \tag{1.13}$$

This is a Gaussian with a FWHM = $\frac{4v}{w_0}\sqrt{2\ln 2}$.

Power Broadening

One final broadening effect which cannot be deduced from a purely classical oscillator model is that of power broadening. Here we must turn to a quantized notion of the atom as a discrete two level system consisting of a lower energy ground state $|g\rangle$ and a higher energy excited state, $|e\rangle$. The scattering of light in this atomic model is equivalent to an absorption and re-emission of a photon by the atom. Since the remainder of this thesis deals with light of a low intensity, power broadening is unlikey to contribute significantly to our transmission signal. We therefore offer only a brief ovrview of this mechanism and refert to [24] for a full derivation. As the incident light intensity increases, the atoms begin to oscillate between the ground and exited state [25]. At most, half of the population is allowed to be in the excited state at one time. The intensity corresponding to this limit is known as the saturation intensity and is defined as $I_{\text{sat}} = \frac{\hbar\omega_0\Gamma}{2\sigma}$. At this point it becomes convenient to introduce the saturation parameter, $s_0 := \frac{I}{I_{\text{sat}}}$. As the intensity of light increases, saturation is achieved for an ever greater range of detunings leading to a broadening of the absorption spectrum with FWHM = $\Gamma\sqrt{1 + s_0}$. To prevent this broadening, we would like to operate in a regime where $s_0 \ll 1$, that is, where $I \ll I_{\text{sat}}$.

1.2 Laser Cooling and Trapping

In the previous section, our discussion of the transmitted intensity in the context of the Lorentz oscillator led us to a derivation of the expected lineshape for our planned absorption spectroscopy measurements. In a similar fashion to the intensity, we can now consider the forces acting on our atoms due to the absorption of radiation. This will lead us to the topic of magneto-optical traps. This is a mechanism for the trapping and cooling of atoms using laser light which we can use in the testing of our oven to potentially increase its efficiency. The following discussion is based on Ref. [25]

1.2.1 Radiation Pressure

Electromagnetic radiation incident on our atoms exerts a force on our atoms that is proportional to the scattering rate R_{sc}, describing the rate of absorption and re-emission of

the light incident on our atoms. This force is given by

$$\mathbf{F}_{\text{sc}} = \frac{\Gamma}{2} \frac{\hbar \mathbf{k} s_0}{1 + s_0 + \left(\frac{2\Delta}{\Gamma}\right)^2}, \tag{1.14}$$

where δ is the detuning of our laser from the atomic resonance frequency. This force describes the pressure exerted by the light on our atoms during a scattering process. Since light is always incident on the atoms from a particular direction, but scattered into a random direction, over many such scattering processes the atoms will experience a force acting along the direction of the incident light. This property allows us to cool our atoms using a configuration known as optical molasses.

Optical Molasses

Let us consider light from two opposing directions impinging on atoms traveling along the same axis as the incident light, as illustrated in Fig. 1.2(a). According to the logic of our previous discussion on Doppler broadening, the atoms in such a scenario will encounter Doppler shifted light from both directions. Our atoms will therefore experience two opposing scattering forces, modified by the respective Doppler shifts. The sum of these forces is given by

$$\mathbf{F} = \frac{\hbar \mathbf{k} \Gamma}{2} \left[\frac{s_0}{1 + s_0 + \left[2\left(\Delta - \mathbf{k} \cdot \mathbf{v}\right)/\Gamma\right]^2} - \frac{s_0}{1 + s_0 + \left[2\left(\Delta + \mathbf{k} \cdot \mathbf{v}\right)/\Gamma\right]^2} \right] \approx -\beta \mathbf{v} \tag{1.15}$$

and is known as an optical molasses. For negative detunings (red detuning), the counter-propagating light is shifted into resonance and slows down the motion of the atoms. This leads to a reduction in the average kinetic energy of the atoms and a subsequent decrease in the temperature of the atomic ensemble via the equipartition theorem (note that although the atomic ensemble is not in thermal equilibrium due to its interaction with the laser light, the definition of a temperature for our atomic ensemble via the equipartition theorem is justified by the Maxwell-Boltzmann velocity distribution of the atoms [25]). This cooling action is, however, limited to a range of velocities bounded by the capture velocity, $v_{\text{cap}} = \frac{\Delta}{k}$, as illustrated in Fig. 1.2(b). In other words, the linear approximation made in Eq. (1.15) is only valid in a limited range of velocities around the zero-crossing. The principle of optical molasses can easily be generalized to three dimensions, thus enabling cooling of the atoms in all spatial directions.

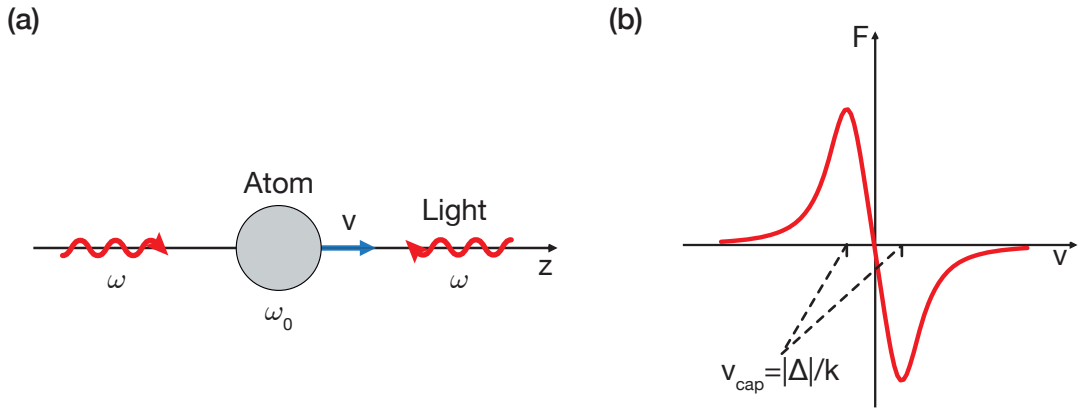

Figure 1.2 (a) A schematic of the optical molasses principle. An atom traveling towards red detuned light, counterpropagating along the axis of its motion, will see this light shifted into resonance and experience a frictive force due to the resonant scattering of the light. (b) A plot of the optical molasses force with the capture area indicated by v_{cap}. Atoms with velocities outside of this area are not cooled by the molasses. Figure adapted from Ref.[26].

From Eq. (1.15) we would expect the optical molasses to slow our atoms all the way to $v = 0$ i.e. to $T = 0$, which is clearly an unphysical result. What, then, are the limits on this type of laser cooling? Here we have to consider the effect of additional stochastic forces acting on our atoms. Firstly, the scattering of light into random spatial directions as well as intensity fluctuations of the incident light lead to a random walk in momentum space and consequently a heating of the atoms proportional to the scattering rate. A limiting temperature is reached when this heating rate is equal to the cooling rate due to the optical molasses. This limiting temperature is known as the Doppler temperature T_D and is minimized for $\Delta = \frac{\Gamma}{2}$, where it takes the form [25]:

$$T_D = \frac{\hbar\Gamma}{2k_B}, \tag{1.16}$$

where k_B is the Boltzmann constant. Secondly, the recoil on an atom from its last emitted photon leads to a fundamental temperature limit known as the recoil temperature [25]

$$T_R = \frac{\hbar^2 k^2}{2k_B m}. \tag{1.17}$$

While optical molasses are able to cool atoms, they are not able to confine them. This is a consequence of the optical Earnshaw theorem which states that a small dielectric particle cannot be trapped using only radiation pressure [27]. For confinement we can use magnetic trapping techniques, which rely on the interaction of the magnetic moment of the atoms and an externally applied magnetic field. In conjunction with the principle of optical molasses discussed previously, this gives rise to the magneto-optical trap.

1.2.2 Magneto-Optical Traps

Let us again consider the 1D scenario illustrated in Fig. 1.2(a), but this time adding a magnetic field $B(z) = -bz$, with a magnetic field gradient b provided by a pair of anti-Helmholtz coils as shown in Fig. 1.3(a). For a two-level atom with total angular momentum $J_g = 0$ and $J_e = 1$, the Zeeman effect will lead to a splitting of the excited state into three Zeeman substates separated by a position-dependent energy $\Delta E = \mu_B g_{J_e} m_{J_e} bz$, where μ_B is the Bohr magneton, g_{J_e} is the Landé g-factor and m_{J_e} is the magnetic quantum number of the relevant Zeeman substate. If the light from our incident laser beams is $\sigma^-(\sigma^+)$ polarized it will address the $m_{J_e} = -1(m_{J_e} = 1)$ magnetic substate as illustrated in Fig. 1.3(b). Thus, the atoms will experience a force

$$\mathbf{F} = \frac{\hbar \mathbf{k} \Gamma}{2} \left[\frac{s_0}{1 + s_0 + \left[2\left(\Delta - \mathbf{k}\cdot\mathbf{v} - \mu_B g_{J_e} m_{J_e} bz/\hbar\right)/\Gamma\right]^2} - \frac{s_0}{1 + s_0 + \left[2\left(\Delta + \mathbf{k}\cdot\mathbf{v} + \mu_B g_{J_e} m_{J_e} bz/\hbar\right)/\Gamma\right]^2} \right] \approx -\beta \mathbf{v} - \mathbf{k} z, \quad (1.18)$$

where position-dependent part of the force guarantees the localization of the atoms. As was the case with optical molasses, this force can be generalized to two and three dimensions to confine atoms to an axis and a point, respectively. The former lends itself well to our oven, since we want to generate a highly collimated beam of atoms (more details on the precise shape of our atomic beam will follow in Chapter 2).

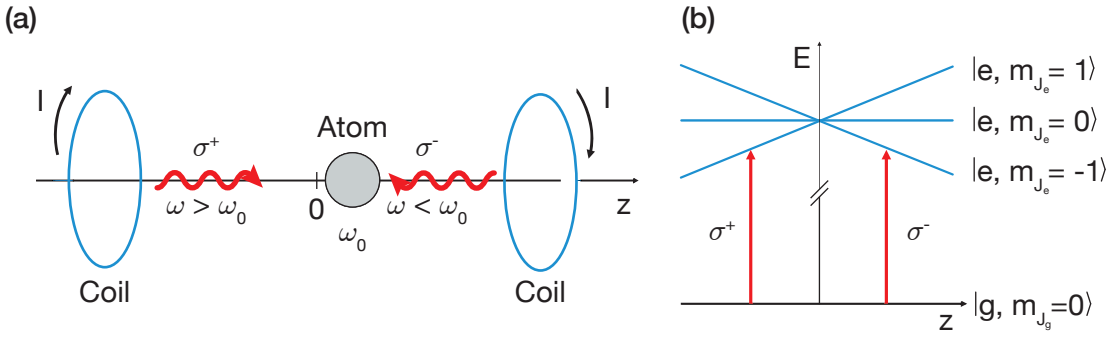

Figure 1.3 (a) A schematic of the working principle of a MOT in 1D. (b) The magnetic field gradient generated by the coils leads to position-dependent Zeeman splitting of the excited state level. Figure adapted from Ref.[26].

1.3 Strontium

Having discussed the general principles of light-matter interaction in the previous sections, we will briefly discuss their application to strontium.

As an alkaline earth metal, strontium possess two valence electrons, which give rise to the rich electronic structure illustrated in Fig. 1.4. The blue and red MOT transitions are employed for the trapping and cooling of strontium in two stages according to the principles discussed in Subsection 1.2.2. Due to its narrow linewidth, the red MOT transition allows for cooling on the order of μK [28]. Since atoms have a small probability of decaying to the $^3P_1$ and $^3P_2$ states via the $^1D_2$ state, repumping transitions are employed to place atoms in the $^3P_1$ state from where they can decay back to the ground state to be addressed by the blue MOT once more. As mentioned in the introduction, the extremely narrow clock transitions is used in atomic clocks [6]

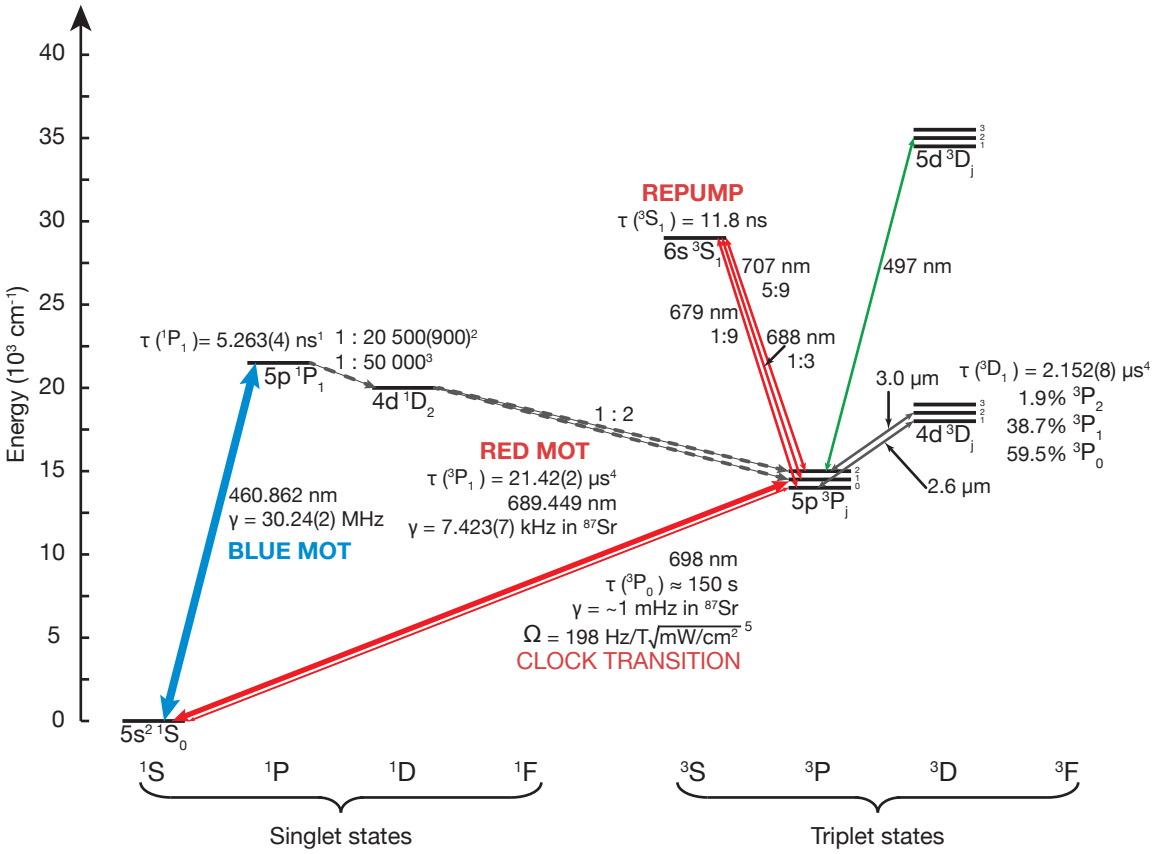

Figure 1.4 The ernegy level diagram of strontium. Spectroscopic data is taken from [1]:[29], [2]:[30], [3]:[31], [4]:[32] and [5]:[33].

Strontium's four naturally occurring isotopes appear with different natural abundances, as recorded in Table 1.1. Another noteworthy feature is the non-zero nuclear spin of ^{87}Sr.

For the purpose of absorption spectroscopy and a 2D MOT, we plan to use the blue MOT transition. Its natural linewidth of 30.24(2) MHz provides the largest radiation pressure on the atoms [see Eq. (1.15)] making it advantadgeous for addressing atoms in a short

Table 1.1 A Table recording the basic feeatures of the four naturally occuring isotopes of strontium.

Isotope	Abundance	Nuclear Spin	Statistics
^{84}Sr	0.56 %	0	Bosonic
^{86}Sr	9.86 %	0	Bosonic
^{87}Sr	7.00 %	$\frac{9}{2}$	Fermionic
^{88}Sr	82.58 %	0	Bosonic

interaction time. The feasibility of a 2D MOT for the compression of strontium atomic beams has been demonstrated by Ref.[34], where stacks of permanent N35 neodymium magnets were used to generate a gradient of 34 G/cm in the trapping region. Permanent magnets are beneficial, since they can be brought much closer to the atoms in the vacuum chamber than electromagnets which consists of a large number of coils and also have to deal with heating due to large driving currents. We therefore plan to implement a similar 2D MOT with our oven setup. Having thus established the basic principles of light-matter interaction, we will now move on to discuss the expected properties of our atomic beam when interrogated by spectroscopic light.

Chapter 2

Atomic Beam Characteristics

In the following we will lay the theoretical groundwork for an understanding of our current oven and more generally for the physics of atoms effusing from an oven through a set of capillary tubes. Once we have developed our model and shown that it accurately reproduces our data, we will make predictions concerning a wide variety of parameters that will be of importance in our new oven. With these predictions we hope to find an optimal set of parameters which we can subsequently implement and measure in our new oven.

We begin our discussion, very concretely, with the absorption spectrum of an atomic beam. This spectrum can be directly measured in an experiment and allows one to calculate most of the relevant beam quantities, such as the beam divergence, atomic flux, velocity spread, forward intensity and the density distribution. It will be our first task, therefore, to derive an expression that allows us to understand the absorption data of our current oven. Our experimental setup is the following: Sr atoms are heated to 550 °C in a steel crucible and effuse through a set of microchannels (diameter: 200 μm, length: 10 mm) into the main vacuum system. The center of the MOT chamber and the center of the microchannel array define an axis, which we denote as the z-axis for all subsequent calculations. Spectroscopy is performed at two different points at axes perpendicular to the z-axis (Fig. 2.2).

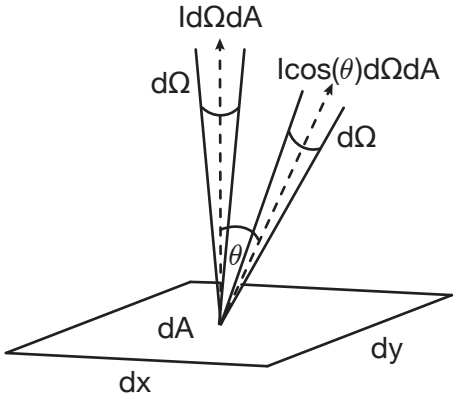

Figure 2.1 A sketch of the principle of Lambert's cosine law. The intensity of atoms scattering from a diffuse surface element dA, into a spatial direction scales with the cosine of the angle of the scattering direction to the normal of the surface.

The microchannels in the oven nozzle serve to collimate the atoms. To understand how, we must first look at the scattering behavior of our atoms at the inner walls of the capillaries. It is reasonable to assume that the inner walls of our capillaries exhibit some

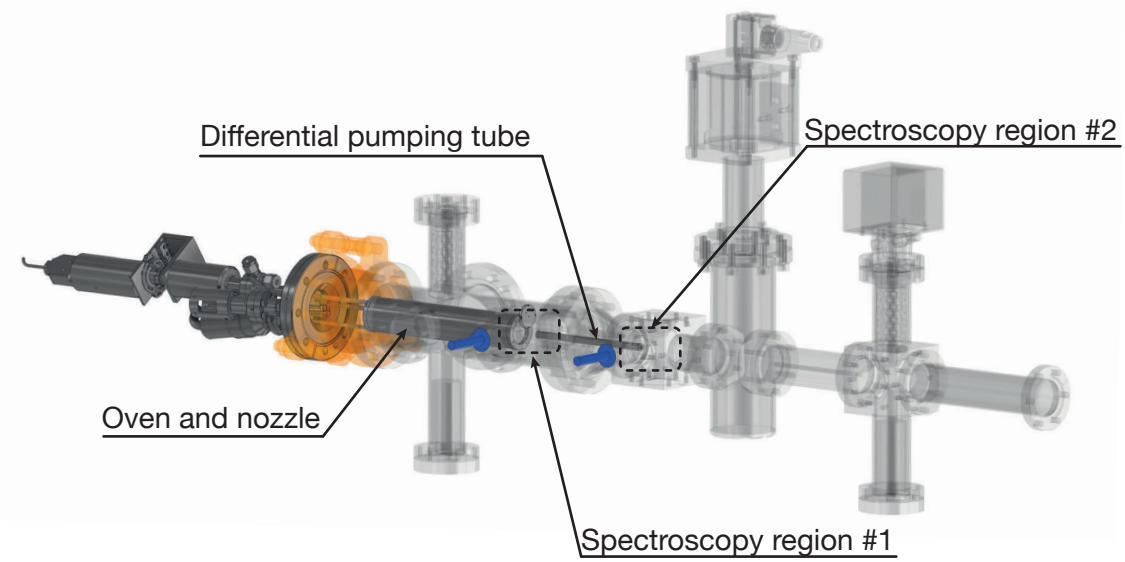

Figure 2.2 A render of the back end of our vacuum system with the parts affecting our atomic beam directly rendered as solid. The nozzle is integrated into at the front of the oven. The blue arrows represent the 461 nm light used to perform spectroscopy in the two indicated regions.

surface roughness when viewed on an atomic scale and that therefore, atoms scatter in an isotropic manner off these walls. More specifically, consider the scattering of atoms at a diffuse surface element dA into a solid angle $d\Omega$ (as illustrated in Fig. 2.1. The intensity of atoms scattered into a solid angle normal to the surface is given by $I d\Omega dA$. At an angle θ, this is scaled by a factor $\cos(\theta)$ to give $I\cos(\theta)d\Omega dA$. For this reason, this scattering behavior is also known as Lambert's cosine law.

Armed with this information on the scattering behavior of the atoms in our capillaries, it is easy to see that atoms impinging on the walls of our capillaries have an equal probability of scattering into the forward and backward directions. For every subsequent scattering event, these probabilities accumulate, such that those atoms undergoing many wall scattering processess have a very low probability of always scattering in the forward direction and reaching the end of the capillaries. By contrast, those atoms that enter the capillaries at very shallow angles suffer no such wall collisions and may travel through the capillaries unhindered. This effectively collimates the atomic beam and gives a defined directionality to the speeds of the effusing atoms. These can then be described by the following modified Maxwell-Boltzmann distribution [20, 35]:

$$f(v) = \frac{2v^3}{a^4} e^{-\frac{v^2}{a^2}}, \tag{2.1}$$

where $a = \sqrt{\frac{2k_B T}{m}}$, k_B is the Boltzmann constant and m is the mass of a strontium atom.

As we discovered in Chapter 1, the intensity of the transmitted spectroscopic laser light incident on the atomic beam obeys the *Lambert-Beer law* [25]:

$$I = I_0 e^{-\mathrm{OD}(\Delta)}, \tag{2.2}$$

with the optical depth

$$\mathrm{OD}(\Delta) = n_0 \sigma(\Delta) D, \tag{2.3}$$

where n_0 is the atomic density at the nozzle exit and D is the diameter of the nozzle.

The absorption cross-section, $\sigma(\Delta)$ takes the following form:

$$\sigma(\Delta) = \frac{\sigma_0}{1 + \frac{4}{\Gamma^2}(\Delta + k v_\perp)^2} \text{ with } \sigma_0 = \frac{3\lambda_0}{2\pi}. \tag{2.4}$$

The difficulty in this expression arises from the transverse velocity, $v_\perp$. A priori, its distribution is unknown, since it depends on the angular distribution of the effusing atoms.

2.1 Angular Distributions

In high-vacuum environments such as those encountered at the exit of our oven, atoms are usually said to obey a molecular flow regime. In this type of regime, interatomic collisions are considered to be negligible due to the low densities of the atomic gas. We can quantify this behavior by defining a characteristic quantity known as the Knudsen number, Kn. The Knudsen number defines the ratio of the mean free path λ_{MF} of an atom traveling through a capillary to the length L of the capillary:

$$\mathrm{Kn} = \frac{\lambda_{\mathrm{MF}}}{L}. \tag{2.5}$$

The mean free path is the average path length that an atom traverses before it collides with another atom. In the molecular flow regime, this quantity is much larger than the any other length scales of the system and hence Kn$\gg$1. Of course, variations in either the mean free path or in the length of the capillaries will results in deviations from this flow regime. For example, at a typical oven operating temperature of $T = 550°$C, the Knudsen number for our capillaries is calculated to be

$$\mathrm{Kn} = \frac{\lambda_{\mathrm{MF}}}{L} = \frac{k_B T}{\pi\sqrt{2} d^2 p L} \approx 0.74, \tag{2.6}$$

using $d = 498$ pm (twice the van-der-Waals radius of strontium), $p = 10^{10.255 - \frac{8324}{T}}$ (the vapor pressure of strontium [36]) and $L = 10$ mm. Here the Knudsen number is approaching 1 and we are therefore in an intermediate regime where collisions are no longer negligible. If we increase the temperature even further, we enter a viscous flow

regime, where Kn$\ll$1 and atomic flow has to be modeled using the Navier-Stokes equation.

Although we find ourselves in the intermediate regime, we will first turn our attention to the molecular flow regime, as the calculations involved are considerably less cumbersome than in the intermediate regime. The reduced complexity of this regime will also help us to gain some basic intuition about the behavior of our atoms. The following derivations are largely taken from Ref. [37].

2.1.1 The Molecular Flow Regime

In the molecular flow regime the following assumptions are made [38]:

- The atoms striking the wall of the microcapillaries follow Lambert's cosine law
- The rate at which atoms strike a unit area of wall, $\nu(z)$ of a microcapillary, at a distance z from the channel entrance, is approximated to be linearly decreasing with L

$$\nu(z) = \nu_0 \left[\zeta_1 - (\zeta_1 - \zeta_0)\frac{z}{L}\right], \tag{2.7}$$

with $\zeta_0 = \alpha(\beta)$ and $\zeta_1 = 1 - \alpha(\beta)$ and ν_0 is the rate at which atoms in the oven enter a unit area of the capillary aperture. The terms α and β are two important geometrical factors fixed by the length L and the radius r of the aperture as follows:

$$\beta = \frac{2r}{L}, \tag{2.8}$$

$$\alpha = \frac{1}{2} - \frac{1}{3\beta^2}\left(\frac{1 - 2\beta^3 + (2\beta^2 - 1)\sqrt{1+\beta^2}}{\sqrt{1+\beta^2} - \beta^2 \operatorname{arsinh}\left(\frac{1}{\beta^2}\right)}\right). \tag{2.9}$$

For the moment, let us consider a single microcapillary. For atoms incident on the capillary, we distinguish between two scenarios: In the first, an atom incident on the capillary at an angle $\theta < \arctan\left(\frac{2r}{L}\right)$ travels through the capillary without any wall collisions. In the second, i.e. for angles $\theta \geq \arctan\left(\frac{2r}{L}\right)$, the atom strikes the wall at least once. With this in mind we introduce the parameter $q := \left(\frac{L}{2r}\right)\tan(\theta)$ and define the angular distribution of atoms emerging from the capillary as

$$j(\theta) := \begin{cases} \alpha\cos(\theta) + \frac{2}{\pi}\cos(\theta)\left[(1-\alpha)R(q) + \frac{2}{3q}(1-2\alpha)\left(1-(1-q^2)^{3/2}\right)\right] & \text{if } q \leq 1 \\ \alpha\cos(\theta) + \frac{4}{3\pi q}(1-2\alpha)\cos(\theta) & \text{if } q \geq 1 \end{cases}$$

with

$$R(q) = \arccos(q) - q\sqrt{1-q^2} \tag{2.10}$$

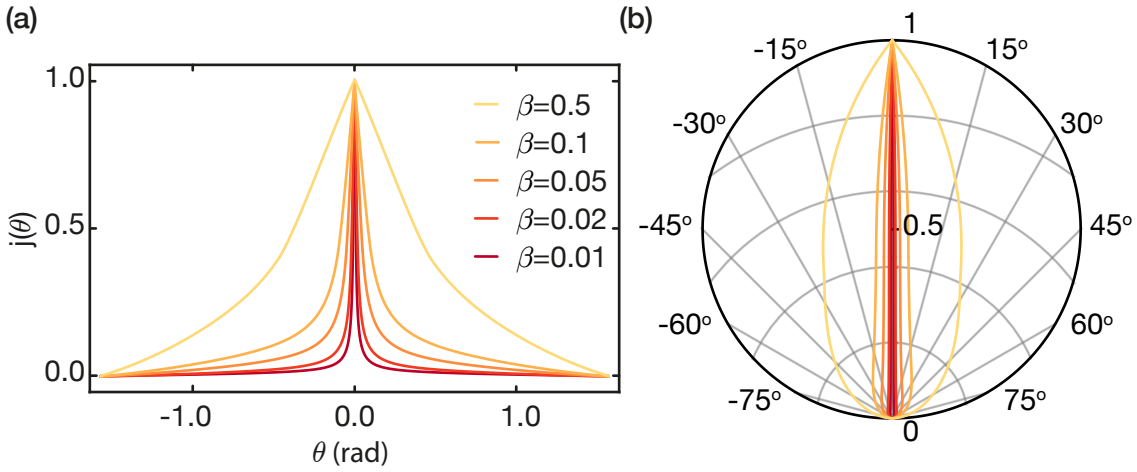

Figure 2.3 (a) A plot of the angular distribution in the molecular flow regime as a function of the exit angle θ. As the length of the capillaries is decreased, i.e. as $\beta \to \infty$, the distribution broadens until a cosine distribution is reached in the limiting case. (b) A polar plot of the same distribution showing the shape of the atomic beam. The cosine distribution is now directly visible as the surrounding circle (thick black line)

This is calculated by the authors of Ref.[37] from Ref.[39]. It is important to note that the angular distribution (Eq. (2.1.1)) is purely dependent on the aspect ratio of the capillaries. In other words, external factors such as the temperature and pressure have no bearing on $j(\theta)$ in the molecular flow regime. Furthermore, we note that $j(\theta)$ is not normalized over a solid angle. More specifically

$$\int_0^{\frac{\pi}{2}} d\theta \, \sin(\theta) \int_0^{2\pi} d\phi \, j(\theta) = \pi W \tag{2.11}$$

where W is known as the Clausing factor and describes the transmission probability of a microcapillary channel for a given β [40]. This factor is given by

$$W = 1 + \frac{2}{3}(1 - 2\alpha)(\beta - \sqrt{1 + \beta^2}) + \frac{2}{3}(1 + \alpha)\beta^{-2}(1 - \sqrt{1 + \beta^2}). \tag{2.12}$$

The normalized angular distribution is shown in Fig. 2.3 for various values of β.

We see that as β increases the distribution becomes wider until at $\beta = \infty$, that is, in the case of an orifice of infinitesimal length, we recover the cosine distribution expected from Lambert's cosine law.

2.1.2 The Intermediate Regime

As in the molecular flow regime atoms striking the wall of a capillary follow Lambert's cosine law. However, the wall collision rate, $\nu(z)$, is no longer sufficient to determine the angular distribution. Rather, we require an additional interatomic collision rate. This rate is closely related to the density profile in the capillary, which is defined in the following manner [41]:

$$n(z) = n_s \left[\xi_1 - (\xi_1 - \xi_0)\frac{z}{L}\right]. \tag{2.13}$$

Furthermore, we will make the crucial approximation $\xi_i \approx \zeta_i$ [37]. Indeed, substantial variations in ξ_i have been shown to be experimentally indistiguishable [41] with the exception of the commonly used model put forth by Giordmaine and Wang [42] wherein $\xi_0 = 0$ (i.e. zero density at the exit of the capillaries). Under these assumptions the angular distribution in the intermediate regime is defined as

$$j(\theta) = \begin{cases} \frac{2}{\sqrt{\pi}}\xi_0\cos(\theta)\frac{e^{\delta'^2}}{\delta'}\left[\frac{R(q)}{2}\left(\operatorname{erf}\left(\delta'\frac{\xi_1}{\xi_0}\right) - \operatorname{erf}(\delta') + F(\xi_0,\xi_1,\delta')\right) + S(q)\right] + \xi_0\cos(\theta) & \text{if } q \le 1 \\ \xi_0\cos(\theta) + \frac{2}{\sqrt{\pi}}\xi_0\cos(\theta)\frac{e^{\delta'^2}}{\delta'}S(1) & \text{if } q \ge 1 \end{cases}$$

with

$$S(q) = \int_0^q \sqrt{(1-t^2)}\left[\operatorname{erf}\left(\delta'\left(1 + \frac{t(\xi_1-\xi_0)}{q\xi_0}\right)\right) - \operatorname{erf}(\delta')\right]dt, \tag{2.14}$$

$$F(\xi_0,\xi_1,\delta') = \frac{2}{\sqrt{\pi}}\delta'\frac{(1-\xi_1)}{\xi_0}e^{-\left(\frac{\delta'\xi_1}{\xi_0}\right)^2}, \tag{2.15}$$

$$\delta' = \frac{\delta}{\sqrt{\cos(\theta)}}, \tag{2.16}$$

$$\delta = \frac{\xi_0}{\sqrt{2Kn(\xi_1-\xi_0)}}. \tag{2.17}$$

As before, the explicit form of this angular distribution is taken from Ref.[37] based on a calculation by Ref.[42].

Whereas the angular distribution in the molecular flow regime was determined only by the geometry of the capillaries, the intermediate regime distribution comes with a temperature dependence in the form of the Knudsen number. Furthermore, the centerline intensity is now no longer unity (as it was in the molecular flow regime) and needs to be normalized accordingly. The intermediate regime distribution is illustrated in Fig. 2.4 for various temperatures.

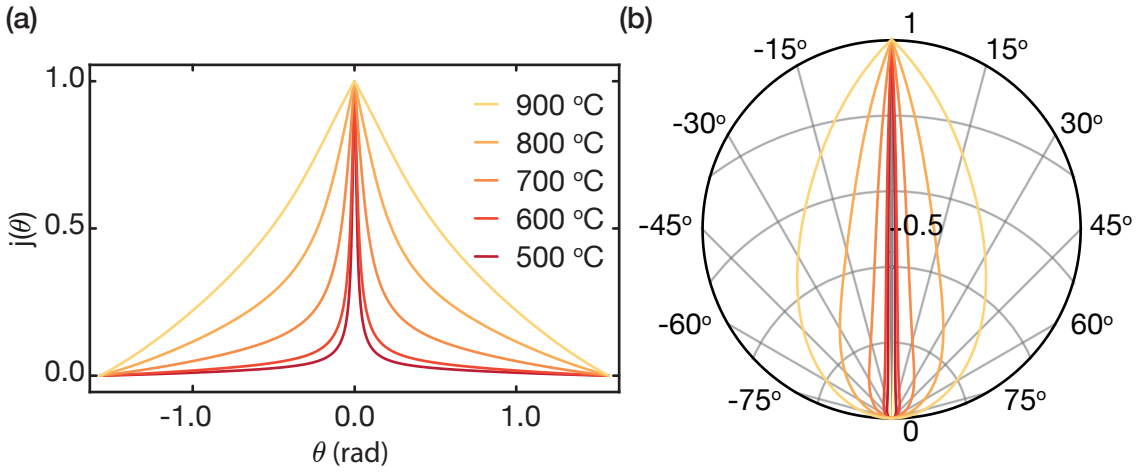

Figure 2.4 (a) A plot of the angular distribution in the intermediate flow regime as a function of the exit angle θ. The distribution now needs to be normalized since the centerline intensity is no longer unity and decreases with increasing temperature. As the temperature increases, inter-atomic collisions become more frequent and the distribution broadens. (b) A polar plot of the same distribution showing the shape of the atomic beam. Again, the cosine distribution is visible as the surrounding circle (thick black line)

2.2 Transmission Spectra

Using the above angular distributions we are now in a place to derive an appropriate expression for the absorption cross-section of atoms emerging from our microcapillary array. Our expression must combine the speed and angular distributions of our atoms, as well as their individual absorption cross-sections. We begin, therefore, with the integral

$$\begin{aligned}\widetilde{\sigma}(\Delta) &= \int_0^\infty dv \int_\Omega d\Omega f(v) j(\theta) \sigma(\Delta) \\ &= \sigma_0 \frac{2}{a^4} \int_0^\infty dv \int_0^{\frac{\pi}{2}} d\theta \sin(\theta) \int_0^{2\pi} d\phi \frac{j(\theta) v^3 e^{-\frac{v^2}{a^2}}}{1 + \frac{4}{\Gamma^2}(\Delta + kv \sin(\theta)\cos(\phi))^2},\end{aligned} \tag{2.18}$$

and simplify this to

$$\sigma(\delta) = 2\sigma_0 \int_0^\infty d\rho \int_0^{\frac{\pi}{2}} d\theta \sin(\theta) \int_0^{2\pi} d\phi \frac{j(\theta) \rho^3 e^{-\rho^2}}{1 + (\delta + \eta\rho \sin(\theta)\cos(\phi))^2}, \tag{2.19}$$

by introducing the parameters $\rho := \frac{v}{a}$, $\delta := \frac{2\Delta}{\Gamma}$ and $\eta := \frac{2ka}{\Gamma}$. This integral can be further

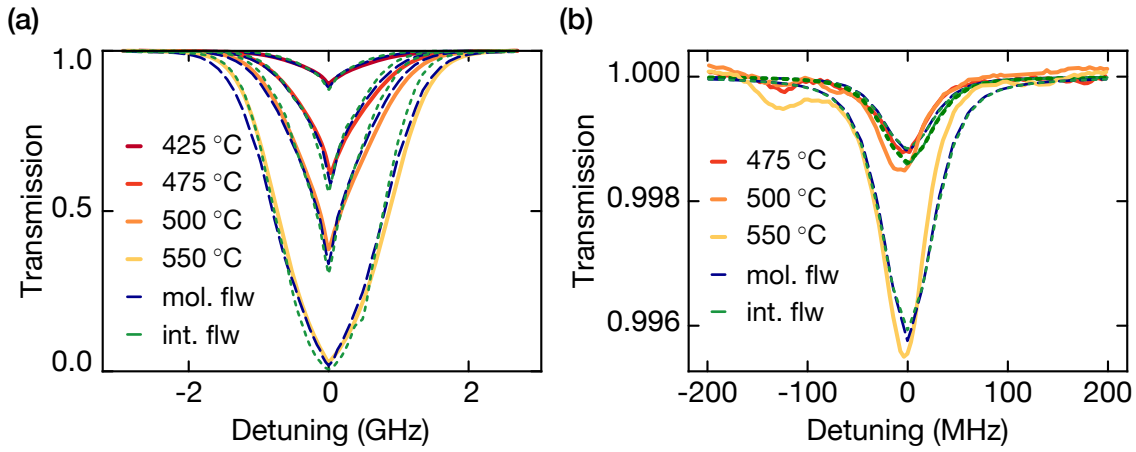

Figure 2.5 (a) Absorption data from our current oven taken at a distance of ≈ 3 mm from the nozzle. The fit of our model to the data is indicated in blue (green) in the case of the molecular flow (intermediate flow) regime. Low temperatures of max. 550°C result in a better fit for the molecular flow model. The systematic skew towards higher detunings is the result of excessive scan frequencies. (b) Absorption data from our current oven taken after the DPT, resulting in a reduced transmission and narrowing of the peak. Additional peaks at lower detunings are the result of the strontium isotopes with a lower natural abundance.

subdivided according to the definition of $j(\theta)$ into

$$\sigma(\delta) = 2\sigma_0 \int_0^\infty d\rho \left(\int_0^{\arctan(\beta)} d\theta \sin(\theta) \int_0^{2\pi} d\phi \frac{j_{q\leq 1}(\theta)\rho^3 e^{-\rho^2}}{1 + (\delta + \eta\rho\sin(\theta)\cos(\phi))^2} + \int_{\arctan(\beta)}^{\frac{\pi}{2}} d\theta \sin(\theta) \int_0^{2\pi} d\phi \frac{j_{q\geq 1}(\theta)\rho^3 e^{-\rho^2}}{1 + (\delta + \eta\rho\sin(\theta)\cos(\phi))^2} \right). \tag{2.20}$$

Having arrived at an expression for the absorption cross-section, we are now in a position to attempt a fit to some absorption data from our current oven. First, we will fit the data collected from absorption spectroscopy in region 1 at a distance of ≈ 3 mm from the nozzle using both the molecular flow and the intermediate flow distributions. For the fits, we insert Eq. (2.20) into the Lambert-Beer law (Eq. (1.11)) and rescale the detuning by $\frac{\Gamma}{2}$. With a nozzle diameter of $D = 12$ mm and the density as the only free parameter one obtains the fits shown in Fig. 2.5(a).

Similarly, we can use our model to fit the data taken in region 2, directly after the differential pumping tube (DPT). However, since the DPT is at room temperature, any atoms that collide with the wall of the tube on the way to spectroscopy region 2 effectively stick to the wall of the DPT for good and are considered lost. This means that only atoms that never strike the wall of the DPT make it into spectroscopy region 2 and hence, the DPT restricts the angular range $d\theta$ over which we should integrate in Eq. (2.20). Modifying

the absorption cross-section accordingly one arrives at Fig. 2.5(b). The narrowing of the signal peaks in Fig. 2.5(b) as well as their reduced transmission values are indicative of a vastly reduced atomic flow; a feature which may be improved in a new oven by a narrower nozzle beam. A further feature of Fig. 2.5(b) is the appearance of additional peaks at lower detunings due to the isotope shifts of the four isotopes in our natural-abundance-sample of strontium.

In general we see that the molecular flow regime seems to describe our data better than the intermediate regime, a fact which we attribute to the relatively low temperatures at which the absorption data was taken. A quantitative analysis of the goodness-of-fit is made difficult by a systematic skew of our data. We attribute the observed skew towards positive detunings in Fig. 2.5(a) to an excessive scan speed and the trappings of our home-built PI-control unit.

In both cases, the values of the density provided by our fits now allow us to calculate the flux of atoms $\mathcal{F}$ in both spectroscopy regions in the following manner:

$$\mathcal{F} = n_0 \overline{v}, \tag{2.21}$$

and this in turn provides us with the total flow-rate $\dot{N}$ via

$$\dot{N} = \frac{\pi R_{\text{cap}}^2}{2} \mathcal{F} N_{\text{cap}}, \tag{2.22}$$

where $\overline{v} = 1.33a$ and the number of microchannels $N_{\text{cap}} = 768$ in our current nozzle.

A theoretical value for the density at the exit of the capillaries (that is, at $z = L$) can also be calculated using $n_0 = \xi_0 n_s$ (Eq. (2.13)), where n_s is the source density. This quantity can be calculated using the ideal gas law and the known expression for the vapor pressure of strontium (see Eq. (2.6)). Using our calculated value of n_0 we can obtain the theoretically expected values for the flux and flow-rate at various temperatures in the above fashion and compare these to the values obtained from our fit. This is tabulated in Table 2.1 for T = 550 °C. In the transverse cooling region a theoretical prediction of the flow is more involved and is derived in Appendix A.

We notice a large discrepancy between the theoretical flow-rate and the fitted flow-rate of 53% (34 %) in the case of the molecular flow (intermediate flow) regime. Since this behavior is the inverse of that displayed by the fits themselves (the intermediate fit is worse than the molecular flow fit), we cannot simply attribute this discrepancy to the systematic skew of our data. Since the source density in our oven is also comparatively low (see Table 2.1), the ideal gas law is assumed to hold. Of course, the theoretically calculated value does not take into account any pressure gradient in the chamber or the capillaries itself. This is reflected in the fact that the same value is predicted for

Table 2.1 A table of atomic beam parameters at the exit of the nozzle as generated by the fits of our absorption data (Fig. 2.5). A comparison with the theoretically predicted value yields a large discrepancy of 53% (34 %) in the case of the molecular flow (intermediate flow) regime.

	Density n_0 (atoms/m^3)	Flux $\mathcal{F}$ (atoms/s/m^2)	Flow-rate $\dot{N}$ (atoms/s)	Theoretical flow-rate (atoms/s)
molecular flow regime	7.2×10^{17}	3.8×10^{20}	4.6×10^{15}	9.6×10^{15}
intermediate regime	1.0×10^{18}	5.3×10^{20}	6.3×10^{15}	9.6×10^{15}

both the intermediate and molecular flow regimes. This could well explain the observed discrepancy between the theoretical value and the fitted values.

2.3 Finding an optimum

Having found a model with which we can describe our current absorption data we would like to use the same model to find an optimal parameter set which we can implement in our new oven. Before embarking on the search for this set of optimal parameters, we have to consider which parameter(s) we would like to optimize. As motivated in the introduction, we are interested in maximizing the number of atoms entering our MOT chamber within a certain time interval e.g. every second. These we denote as "usable atoms". Furthermore, we want to maximize the lifetime of our oven to avoid frequent reloading and the resulting interruption of day-to-day measurements. Put simply, we are interested in:

$$(\text{usable atoms/s}) \times (\text{lifetime})\,. \tag{2.23}$$

Clearly, the number of usable atoms per second depends on the total flow-rate as well as the fraction of atoms that make it through the entire vacuum system without any collisions and that are within the capture velocity. We label this fraction as the "usable fraction". Eq. (2.23) then becomes

$$(\text{usable fraction}) \times (\text{total flow-rate}) \times (\text{lifetime})\,. \tag{2.24}$$

However, since the total flow-rate determines the lifetime for a given sample of strontium, these two quantities cancel and we are simply left with the usable fraction. It is this quantity which we will concentrate on first.

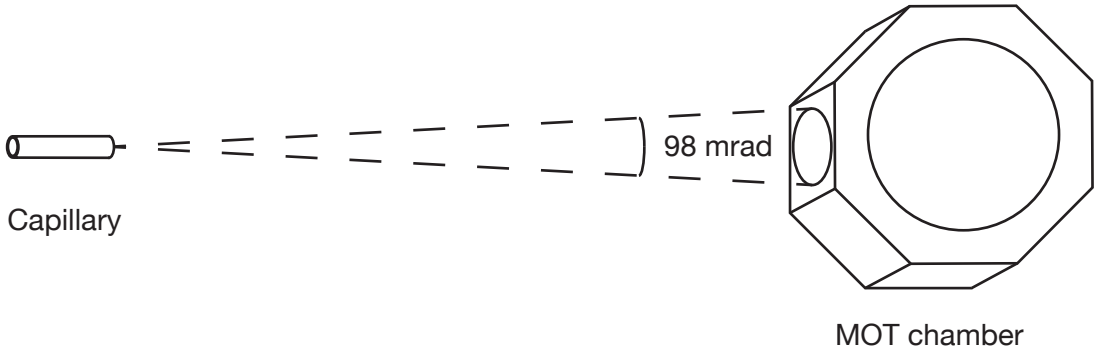

Figure 2.6 Simplified model of our vacuum system used to determine the behavior of the usable atomic fraction and usable atom flow-rate into our MOT chamber. The capillary and the MOT aperture define a 98 mrad cone within which atoms arrive in the chamber.

2.3.1 Usable Fraction of Atoms

We begin by considering an idealized situation where the all DPTs are removed from the vacuum system and the atoms fly unimpeded from the exit of a single capillary all the way to the MOT chamber aperture. Together with the capillary, this aperture defines a 98 mrad cone within which atoms will arrive in the MOT chamber and outside of which they hit the wall of the chamber and are lost (Fig. 2.6). Any further additions to this model, such as DPTs or multiple capillaries only modify the angular boundaries of our cross-section integrals but do not alter the fundamental behavior of such quantities as the usable fraction or the total flow (nonetheless, a detailed treatment of the full scenario as rendered in Fig. 2.2 can be found in Appendix A).

We are now interested in the maximum fraction, $\frac{N'}{N}$, of atoms arriving in our chamber as a function of β. This fraction is given by

$$\frac{N'}{N} = \frac{\int_0^{2\pi} d\phi \int_0^{49\,\text{mrad}} d\theta \sin(\theta) j(\theta)}{\int_0^{2\pi} d\phi \int_0^{\frac{\pi}{2}} d\theta \sin(\theta) j(\theta)}, \tag{2.25}$$

and is dependent on β and the temperature, T. Varying these parameters within reasonable boundary conditions (e.g. $\min\{\beta\} = 0.01$ and $\max\{T\} = 900°\text{C}$) and calculating the resulting usable atom fraction produces Fig. 2.7.

We note a non-linear decay in the fraction with increasing β and conclude that it is advantageous to decrease the aspect ratio of the capillaries if we wish to increase our usable fraction of atoms. The temperature exhibits a similar behavior, albeit with a less pronounced slope than for variable β's. Additionally, a leveling-off at lower temperatures is observed. This behavior corresponds to a transition to the molecular flow regime, wherein

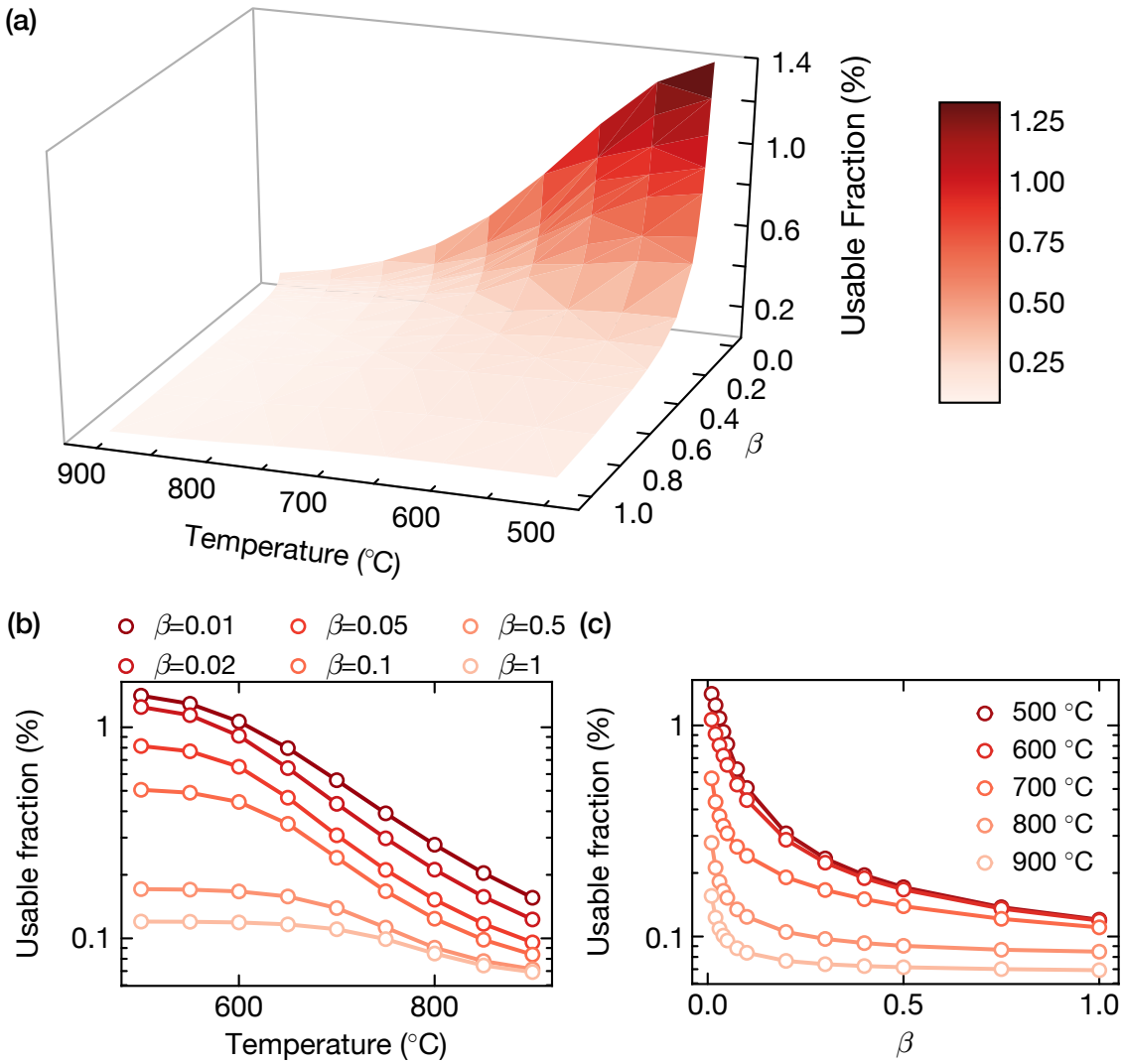

Figure 2.7 (a) A plot of the usable fraction over the parameter space of temperature and capillary aspect ratio, β. (b) and (c) semi-log plots of the usable fraction as a function of temperature and aspect ratio respectively.

the temperature no longer has any effect on the angular distribution and the usable fraction is fixed at a constant value for a given capillary aspect ratio. Though a decrease in β and T certainly yields a higher usable fraction of atoms, it also has an adverse effect on the total flow-rate, stemming from our interest in maximizing the oven lifetime. The precise behavior of the total flow-rate as an isolated quantity is explored in the following.

2.3.2 Total Flow-Rate of Atoms

Subjecting the total flow-rate of atoms to the same treatment as the usable fraction yields Fig. 2.8. The flow-rate was calculated using the same procedure as for the theoretical flow-rate in Table 2.1 and hence overestimates the flow by up to 50%, a fact which we have to keep in mind when we look at the predicted lifetime of our oven at the end of the chapter. For the total flow-rate we observe a markedly different behavior than in the case of the usable fraction. Whereas before, lower β's and lower temperatures were advantageous, now higher values of β and T are necessary to generate a higher total flow-rates. This should not come as a surprise to us, since by increasing the temperature we are effectively increasing the density of atoms effusing from our nozzle and by increasing β we are increasing the transmission probability of our atoms through the capillary.

It now remains to be seen how the flow of usable atoms evolves as a function of β and T.

2.3.3 Flow-Rate of Usable Atoms

Since the flow-rate of usable atoms is a combination of the usable fraction and the total flow-rate (Eq. (2.24)), we combine Figs. 2.7 and 2.8 and arrive at Fig. 2.9.

We see that the usable atom flow-rate exhibits a similar behavior to the total flow-rate. Of course, maximizing the usable atomic flow-rate comes at the cost of the oven lifetime. We therefore have to find a reasonable compromise between oven lifetime and usable atom flow-rate. To this end we plot the lifetime of 5 g of strontium (the standard small ampule size) as a function of temperature for various values of β. The result is shown in Fig. 2.10.

The parameter regime under which our current oven operates is given by T = 550 °C and β = 0.02. This yields a usable atom flow of 10^{14} atoms/s and a lifetime of $\approx$ 1000 h (with a possible upward correction of between 30%-50% - see section 1.2 for details). Figs. 2.9 and 2.10 reveal that although there is no way to significantly increase the usable flow of atoms into our chamber for the same lifetime, an increase of a factor of five is feasible. The necessary conditions are: an increase in the temperature to T = 700 °C and a new aspect ratio of β=0.01. This in and of itself only gives a lifetime of 320 hrs, which could be increased to 1600 hrs by accommodating five times more strontium in our

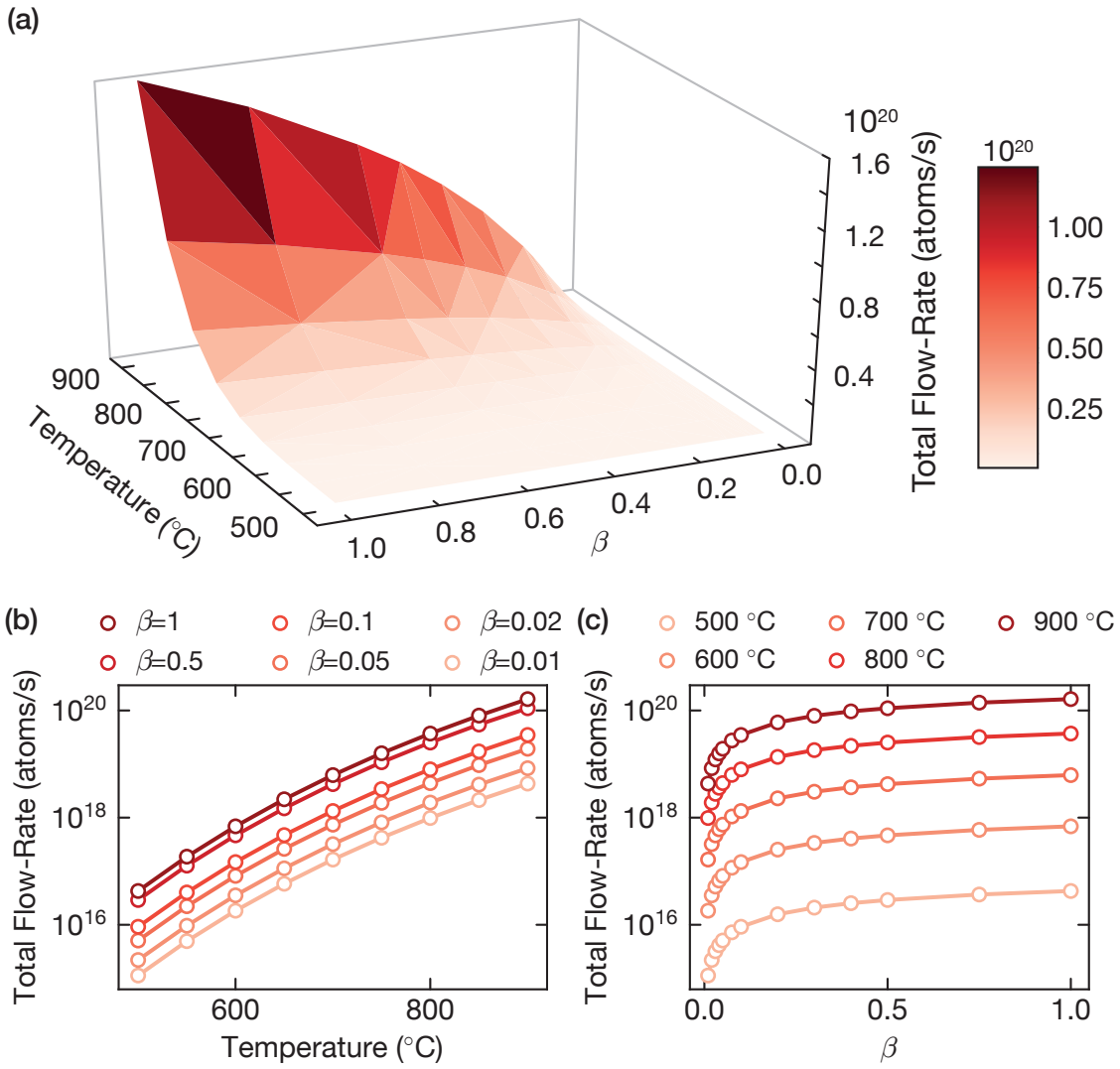

Figure 2.8 (a) A plot of the total flow-rate over the parameter space of temperature and capillary aspect ratio, β. (b) and (c) semi-log plots of the total flow-rate as a function of temperature and aspect ratio respectively.

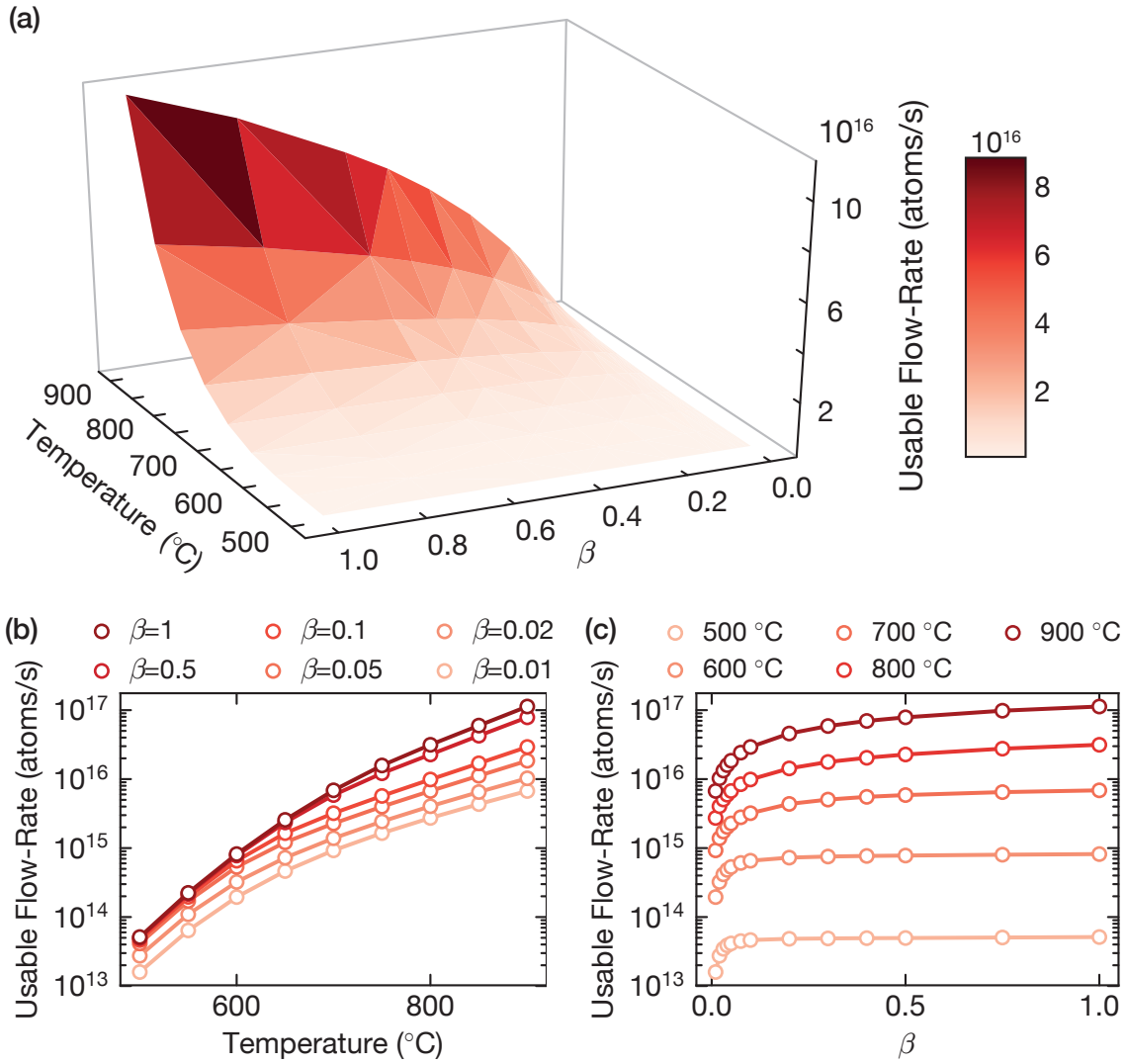

Figure 2.9 (a) A plot of the flow-rate of usable atoms over the parameter space of temperature and capillary aspect ratio, β. (b) and (c) semi-log plots of the usable atom flow-rate as a function of temperature and aspect ratio respectively.

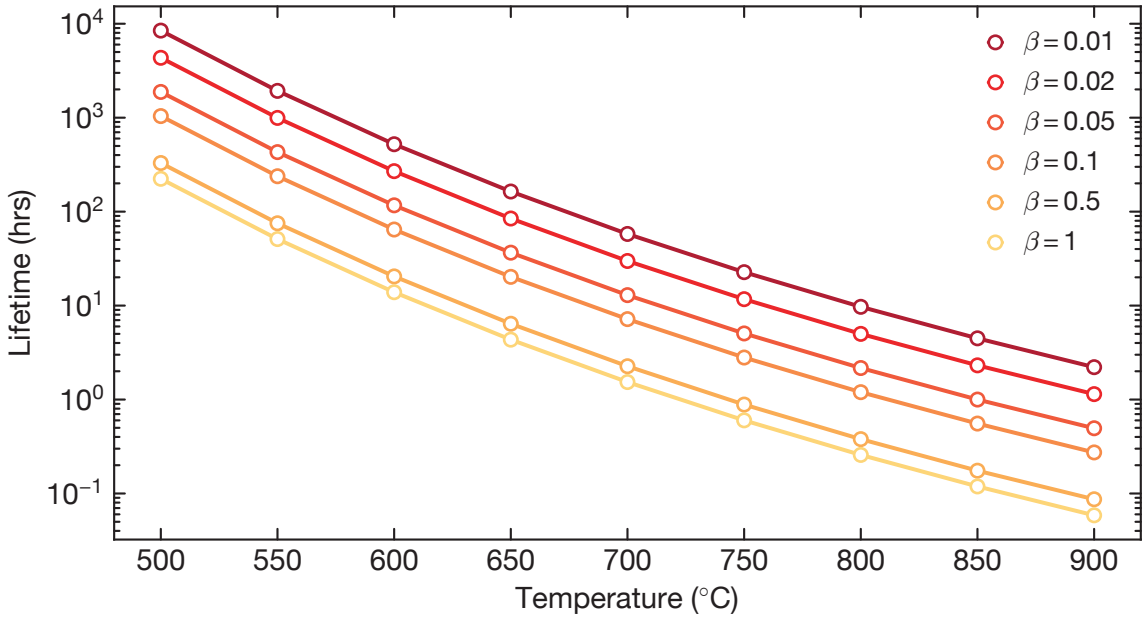

Figure 2.10 A plot of the lifetime of 5g of Strontium as a function of temperature for various values of β

oven. Additionally, we could increase the efficiency of the oven by decreasing the nozzle size so as to be comparable to the DPT diameter, which currently stands at 5 mm (see Appendix A for a detailed description). Our new oven should therefore be able to satisfy these new parameters and ideally be able to test a broad range of parameter regimes to allow for the most comprehensive test of the theory provided in this chapter.

Chapter 3

Oven Design

In the previous chapter we were concerned with finding an optimal set of parameter values to implement in our new oven. Let us quickly recap these desired parameters and see how they influence the design of our new oven. Firstly, we need to be able to test various capillary geometries to assess the accuracy of our theoretical predictions from Chapter 2 concerning the flow-rate of usable atoms. This resulted in the detachable nozzle design described in Subsection 3.4. Secondly, our oven should be able to run at temperatures of up to 900 °C with large temperature gradients between the nozzle and the crucible to prevent any potential clogging of the nozzle. These conditions were realized by the double heating circuits of Subsection 3.3. We also have some secondary requirements for our oven. Among these are the ability to easily reload the oven, straightforward compatibility with our current vacuum system, minimal heating of the surrounding vacuum chamber walls and low power consumption. These secondary requirements led us to attach the entire oven to a conflat (CF) 63 flange and to enclose it in a double layer of heat shields as described in Subsection 3.5.1. We also added water cooling to the outside of our chamber. All major components mentioned above, as well as a number of other parts specific to each of the major components are illustrated in Fig. 3.1 and described in the respective subsections.

3.1 General Features

Our oven can be loaded from the front and used in either vertical or horizontal orientation. It follows a “bottom-up” construction, meaning that components are sequentially stacked on top of each other (as illustrated in the exploded view of Fig. 3.1) with steel support rods holding everything in place. This “bottom-up” approach is designed to make the reloading of the oven easier, since we only need to remove the uppermost layers of the oven (i.e. the heat shields, fixing disk, ceramic nozzle insulation and the nozzle itself) without touching any other components. It also makes any repair processes on the oven much easier, since we have direct access to most of its important components. Finally, the entire oven is fixed to a CF63 flange, allowing us to directly attach the oven to our current vacuum system if so desired.

Prior to any detailed description of the design and construction of the various parts of our oven, two overarching design considerations need to be addressed, namely the dimensions of our oven and the materials used therein.

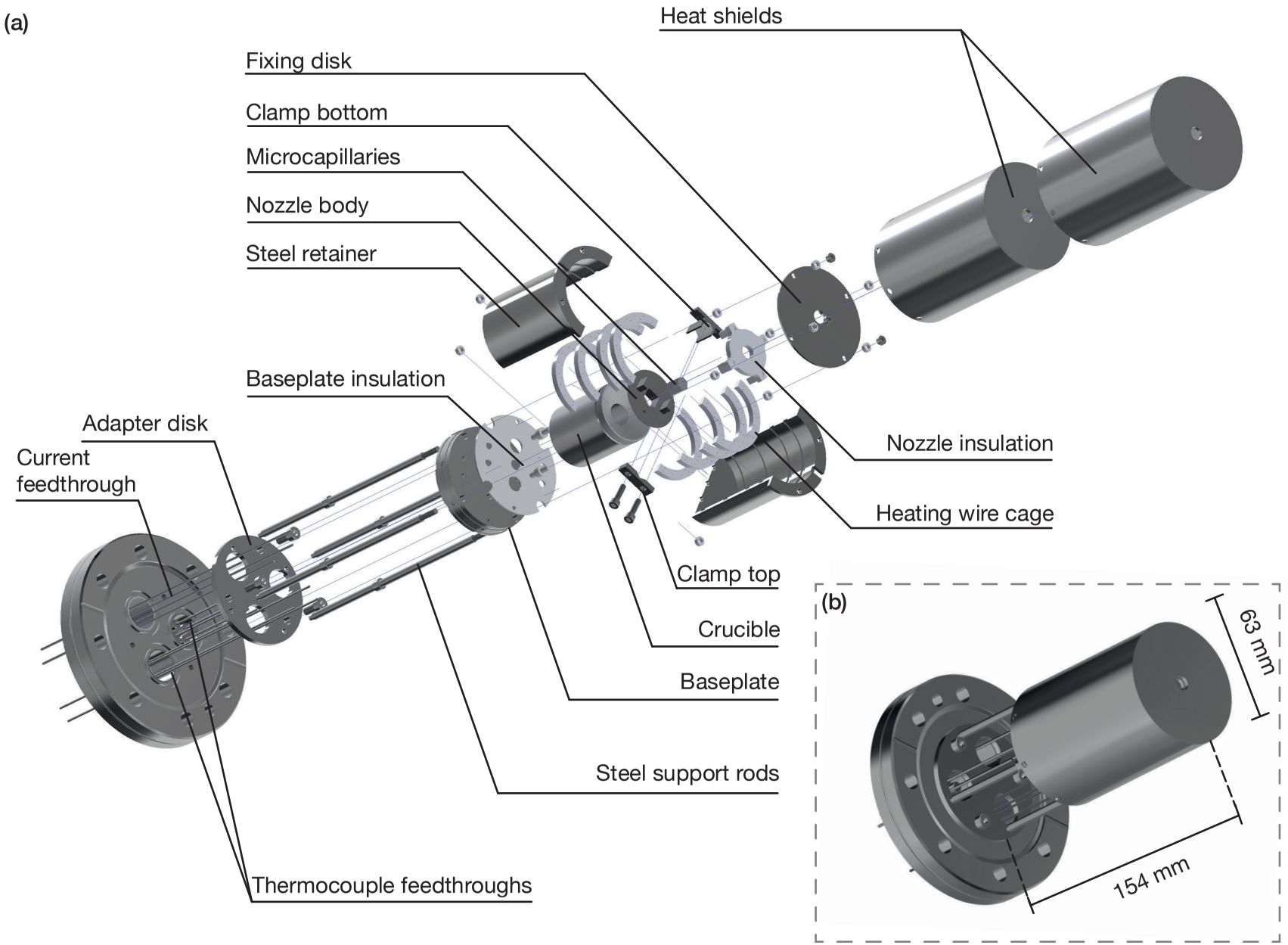

Figure 3.1 (a) An exploded view of our new oven showing all its main components. This view is also meant to highlight a "bottom-up" approach to the construction of our oven. (b) A render of the completed oven as it looks in vacuum.

3.1.1 Dimensions

From the outset, the dimensions of our oven were restricted by two of the requirements mentioned in the introductory paragraph to this chapter. To be compatible with our current vacuum system, the entire oven should ideally fit into CF63 vacuum piping, which has an inner diameter of $\varnothing = 66$ mm. This set the upper limit on the outer diameter of our oven. To increase the oven lifetime, the crucible should be large enough to accommodate 25 g of distilled dendritic strontium (the standard amount contained in a large ampule from Sigma-Aldrich Chemie GmbH: 460346-5G). This effectively provided us with an outer diameter for our crucible. The length of our oven was in principle arbitrary. However, to maintain a compact and easy-to-handle oven, we specified a total length of 154 mm. The combination of inner and outer diameter defined a working space into which the majority of the other oven components needed to fit. It was also for this reason that we decided to mount the entire oven on a CF63 flange, following a similar approach to Ref. [23].

3.1.2 Material Considerations

For the majority of the parts not directly in contact with the heating wire, we decided to use stainless steel. Specifically, we used EN 1.4841 type stainless steel (AISI: 314) due to its mechanical strength at high temperatures and its low magnetic susceptibility as part of the austenitic class of stainless steels [43]. One notable exception were the capillaries. These were manufactured from EN 1.4301 (AISI: 304) steel due to a shortage of commercially available 1.4841 tubing in the required dimensions. EN 1.4301 has a much lower mechanical strength at higher temperatures than 1.4841 and the recommended operating temperature in air is specified at 550 °C. As an alternative, we considered superalloys such as Inconel 600 and Monel 400, which both have high melting points, excellent mechanical strength and high corrosion resistance [44, 45]. Indeed, Monel 400 has previously been used in the construction of an atomic oven [46]. However, due to their material content and bad machinability, these alloys are much more expensive than stainless steel. Since our capillaries would be in vacuum and experience practically no mechanical stress, we decided to forgo these pricier options.

For parts supporting the heating wire or acting as insulation we required an electrical insulator material with very low thermal conductivity. Here, ceramics were the natural choice. Since our ceramic components would have to be machined into non-standard shapes, we decided to use Macor. This is a type of glass ceramic developed by Corning Inc. which can be easily machined using standard metalworking tools. Glass ceramics are not pressed and sintered, making Macor non-porous and which leads to reduced outgassing in vacuum [47]. Furthermore, its thermal expansion coefficient of 12.3×10^{-6} K^{-1} between 25 °C and 800 °C is similar to that of steel at 18.0×10^{-6} K^{-1}. This means that the Macor will experience only small compression forces due to the slightly faster expansion of the

steel at high temperatures in our oven. Its maximum operating temperature is specified at 1000 °C.

As our heating wire material we chose tantalum (Ta). Ta has a melting point of 3017 °C and an electrical resistivity of $\rho \approx 50 \times 10^{-8}$ Ωm at 900 °C [48]. This is twice that of tungsten at the same temperature, another commonly used element for heating elements.

3.2 Crucible

In the crucible of our oven, strontium in the form of distilled dendritic pieces (Sigma-Aldrich Chemie GmbH: 460346-5G) is heated to temperatures between 400 °C-750 °C. This causes sublimation of the strontium subsequent effusion through the capillaries.

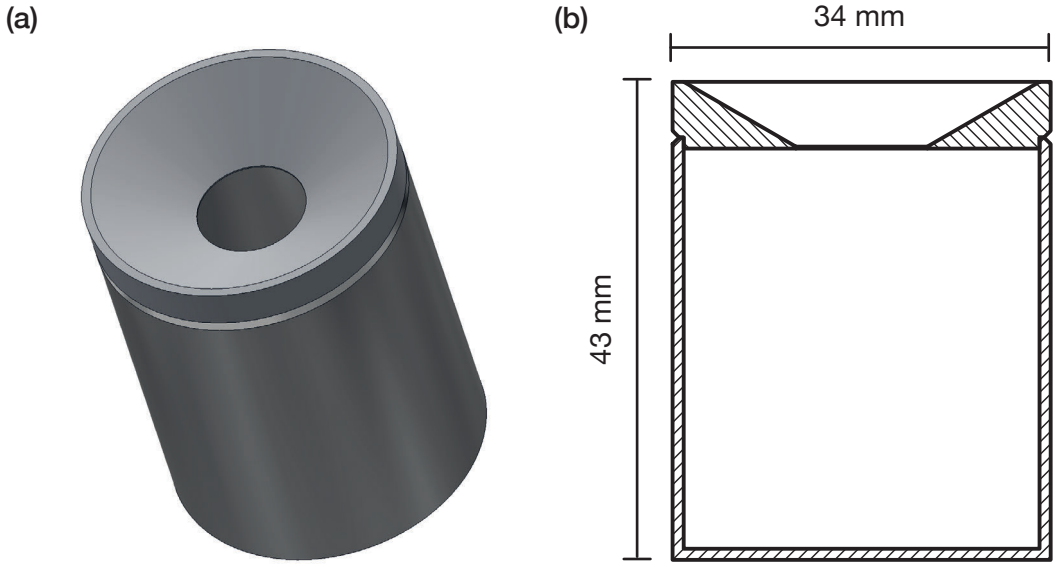

Figure 3.2 (a) A render of the crucible used in our new oven (b) A cross-section of our new crucible, showing the conical top designed to prevent the creeping of strontium to the nozzle as well as the fusing between nozzle and crucible.

The purpose of the conical design of our crucible is threefold. Firstly, any clogging of the nozzle caused by a creeping of the strontium towards the nozzle due to a possible reaction of steel and strontium in vacuum or by means of direct contact between the dendritic strontium and the nozzle, is prevented by the barrier between the strontium and the capillaries created by our conical top of our crucible. Secondly, it inhibits fusing to the nozzle at low pressures (for more details see Sec. 3.4) and thirdly, it funnels any stray pieces of strontium that have not been properly loaded, into the interior of the crucible.

Our crucible had to be manufactured from two separate pieces since its conical shape and small opening would have prevented any cutting tools from hollowing out the inside of the crucible. The two pieces were welded together while maintaining a smooth outer surface of the crucible which could sit flush against the ceramics holding the heating wire (Sec. 3.3). This was achieved by a cutting a groove for the weld seam around the top of the crucible (see Fig. 3.2(b)).

3.3 Heating Circuits

The heating in our oven was designed to be radiative, since any heating via thermal contact would have to include an electrically insulating material between the heating circuits and the crucible, reducing the efficiency of our heaters. Our heating mechanism also had to be able to generate a higher temperature at the nozzle than at the oven to prevent clogging of the nozzle. This was achieved by overlapping two heating circuits, one of which ran the length of the crucible and the nozzle, while the other only covered the length of the nozzle (Fig. 3.3). Since the heating wires could not be in contact with any metal parts in the oven we constructed a retaining cage for the wire consisting of eight half-moon shaped Macor pieces, which together formed four uniform heating rings and centered the crucible and nozzle in the oven. Drilled into each half-disk were two rows of 0.6 mm holes for the heating wires.

Two important dimensional quantities of the heating wire needed to be determined. The first of these was the length of the wire. As the temperature in a wire increases, so does its resistance. For a given temperature, the resistance of a uniform wire of length l and cross-sectional area A is given by:

$$R = \rho \frac{l}{A}, \tag{3.1}$$

where ρ is the previously cited electrical resistivity of the wire. Our lab power supplies (EA Elektro-Automatik: EA-PS 3065-05 B) are limited to V_{max} =65 V and $I_{\text{max}} = 5$ A. Using these limiting values we can calculate the maximum length of wire to use in our oven. Assuming a wire diameter of 0.3 mm as a compromise between the number of windings in our heating circuit and the resistance of our wire, we calculate a maximum wire length of

$$l = \frac{V}{I}\frac{\pi d^2}{4\rho} = \frac{13\ \Omega \times \pi \times (0.15\ \text{mm})^2}{50 \times 10^{-8}\ \Omega\text{m}} \approx 1.8\ \text{m}. \tag{3.2}$$

Our second dimensional quantity was the bending radius of the tantalum wire. Since no specifications were made on the data sheet of our wire, this quantity was determined

experimentally. At room temperature, the wire allowed for multiple bending and unbending sequences with a minimum bending radius on the order of the wire diameter. After heating the wire in vacuum to temperatures in excess of 600 °C it was found that the wire had become very brittle and that very tight kinks in the wire would lead to snapping of the wire upon attempting any further bending or movement of the wire. In the end we settled for a conservative bending radius of 3.5 mm for our heating circuits.

To aid the threading of the wire through the Macor disks, we manufactured a mounting stage consisting of an aluminum cylinder with grooves at the position of the Macor rings, and a matching clamp. This mounting stage was placed on a 30 mm half-inch post and allowed for a uniform threading of the wire along the entire length of the crucible and nozzle. Particular care was taken to ensure that the wires did not deform in between the Macor rings, to avoid risking electrical contact with the crucible or with each other. The mounting stage is illustrated in Fig. 3.3(a) and the finished product in part (b) of the same figure.

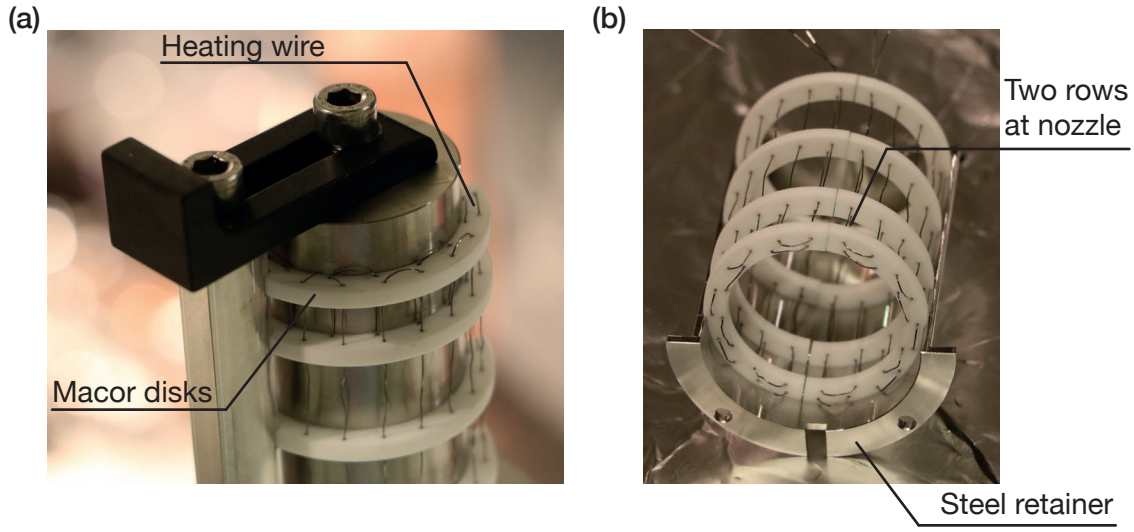

Figure 3.3 (a) The mounting stage used to thread the heating wire through the Macor half-disks. (b) The finished heating wire cage supported by one of the two steel retainers.

The Macor disks were held in place by two steel retainers in the form of half-cylinders with grooves matching the positions of the disks. From a manufacturing standpoint these retainers posed a considerable challenge. Simply cutting a full cylinder in half would have resulted in the loss of material and subsequently two halves that, when brought together, would not have formed a closed cylinder. Therefore, two full cylinders with the required dimensions and features were produced on the lathe and then cut such that there existed two identical halves. However, due to the grain structure introduced into the steel during the forging process [49] the retainers deformed upon cutting. This deformation had to be corrected using a machine press.

The current for the wires was supplied by two lab power supplies connected to four 8.2

A, ⌀=1.3 mm current feedthroughs (VACOM: W-HV3-4CE-NI13). On the vacuum side, the heating wire was connected to these feedthroughs using beryllium copper set-screw connectors (Kurt J. Lesker: FTASSC040). These were chosen for their high electrical and thermal conductivity. The temperature of our oven was measured at the nozzle, the crucible and the baseplate using double hole, oval insulated K-type thermocouples (Omega: OV-1-20-K-12). These were connected to thermocouple feedthroughs (VACOM: W-TC2-CE-K) using M3 $\times$ 8 screws and nuts. We used thermocouples rather than thermistors due to their applicability across a much broader temperature range (K-type thermocouples composed of chromel and alumel can measure temperatures between -200 °C and 1250 °C).

A major challenge associated with these feedthroughs was threading the heating wire and thermocouples through the baseplate and steel retainers to their desired locations. For the purpose of guiding the heating wires, hollow Macor spacers were placed into holes drilled into the baseplate of the oven. The position and size of these holes was matched on the base of the steel retainers and allowed the heating wire to traverse the baseplate and steel retainers without shorting. In addition to acting as a guide for our heating wire, the Macor spacers simultaneously separated the baseplate, steel retainers and crucible, thus thermally insulating these components from each other. However, due to their fragility (⌀= 3.5 mm, L = 15 mm), some of these spacers broke during the construction of the oven and had to be replaced. Even slight shear forces created by minimal sideways movement of the steel retainers were enough to shatter these components and we strongly recommend an alternate solution for the next iteration of this oven. One possibility would be to insulate the heating wire directly using fish-spine beads small enough to pass through the holes in the baseplate. The thermocouples came with their own ceramic insulation and were again guided through holes in the baseplate. All of our thermocouples had to be shortened to allow for exact positioning. Comparing the temperature measurement of our shortened thermocouples to that of an unshortened one showed no significant differences.

Figure 3.4 shows the result of heating our oven and demonstrates its ability to generate a temperature gradient of more than 90 °C. At the time, we had not yet implemented any water cooling on the outside of our vacuum chamber. Since we did not want our flange to exceed temperatures of 100 °C, the maximum temperature in the aforementioned figure is limited to $\approx$ 750 °C. The power consumption at this temperature totaled $\approx$ 80 W, giving us ample reason to believe that temperatures of up to 900 °C are indeed possible.

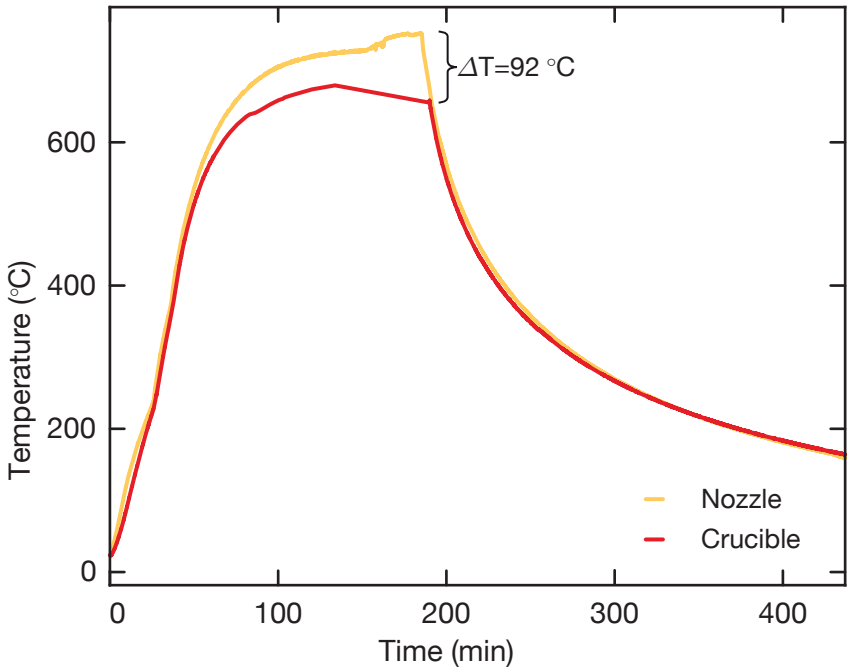

Figure 3.4 The recorded temperature at the crucible and the nozzle demonstrating the ability of our oven to generate temperature gradients between these two elements of more than 90 °C.

3.4 Nozzle

The nozzle represents the heart of our oven and contains the microcapillaries necessary for the collimation of the atomic beam. As mentioned in the introduction to this chapter, our nozzle should be detachable to allow for the testing of multiple capillary geometries. This requirement provides us with our first design challenge. Ideally we want to avoid the use of screws in our oven since these may loosen upon heating of the oven and are also difficult to handle in a glove bag. We therefore require a different way of holding the nozzle in place. This is the purpose of the Macor nozzle insulation and the fixing disk. These isolate the steel rods and by extension, the flange from the extreme heat at the nozzle. The fixing disk is designed to have only minimal thermal contact with the nozzle insulation via four prongs. In the event of the nozzle fusing to the crucible caused by atomic diffusion between the boundary of these two smooth surfaces, its conical shape allows us to detach the nozzle by applying sideways pressure.

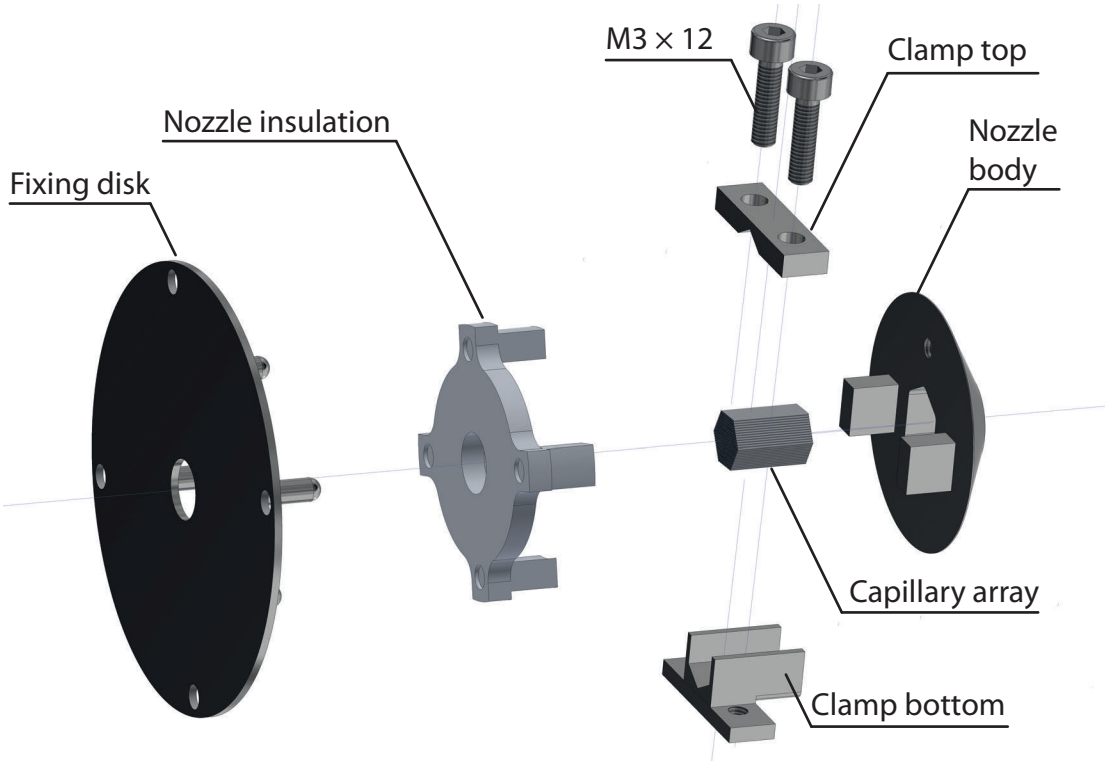

Figure 3.5 A render of the six main elements constituting our nozzle. The capillaries are held in place by two clamps which form a hexagon. This clamp is inserted into the conical body of the nozzle, which is in turn held in place on top of the crucible by the Macor insulation and the fixing disk.

It was decided early on that the capillaries should be clamped in place in a similar fashion to Ref. [22]. Ideally, the required clamping mechanism should consist of as few moving parts as possible to prevent differential movement of the clamping components upon heating and a subsequent distortion of the capillary array. We decided to stack the capillaries into a hexagon as this provides the highest capillary packing density. To achieve this packing density and prevent irregular stacking of the capillaries, the edges of the hexagon would have to be machined such that the radius of curvature of each edge was smaller than or equal to the outer radius of our capillaries (this is illustrated schematically in Fig. 3.6). Due to the limited penetration depth of the milling cutter, it was not possible to cut a hexagon into the conical body of our nozzle. The clamping insert illustrated in Fig. 3.5 was our preferred solution to this problem. Both the clamp top and bottom were fully accessible to the milling cutter, allowing for a sharper cut along the vertices of the hexagon. We assembled our capillaries within this clamping structure before inserting the clamp into the body of the nozzle and fixing it in place using two M3 $\times$ 12 screws. One downside presented by this solution is the increased tolerances between the capillaries due to the a hexagon consisting of two pieces. While the triangular stacking employed in Ref. [22] is better in this regard, it requires more capillaries to cover the same effective

area.

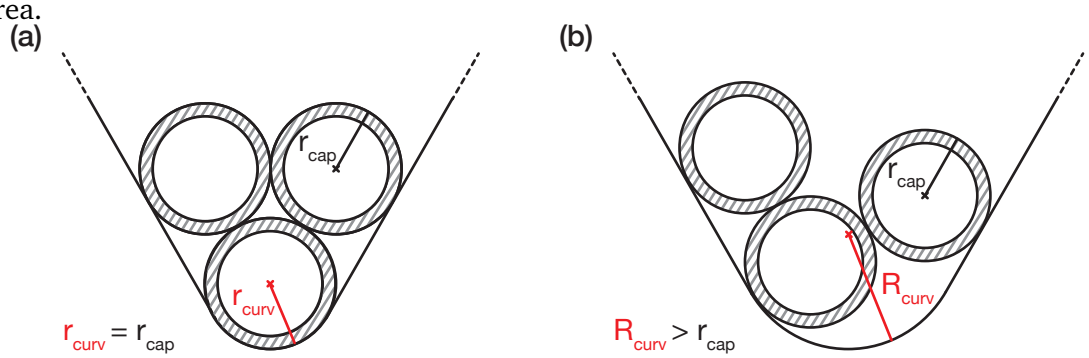

Figure 3.6 (a) A vertex of a hexagon with a radius of curvature, r_{curv} equal to that of the capillary, r_{cap}. This results in even stacking of the capillaries. (b) A vertex with a larger radius of curvature, R_{curv}, than the capillary radius, resulting in irregular stacking and a lower capillary packing density.

3.4.1 Microcapillaries

The microcapillaries were manufactured in four different aspect ratios (0.04, 0.027, 0.02, 0.01) by Robert-Helwig GmbH. We specified a burr-free cut at the ends of each capillary to ensure that the angular distribution of atoms exiting the capillaries was not artificially narrowed/broadened by atoms bouncing off the burrs at odd angles. The ends of the capillaries were observed under a microscope as shown in Fig. 3.7(b) and (c). The former clearly shows that the ends of the capillary have an uneven, pitted finish. This could be the result of using electrical discharge machining to cut the capillaries. It seems that the majority of the imperfections are height variations in the wall of the capillaries rather than burrs sticking into or out of the capillary. Based on Fig. 3.7(c) we approximate a surface roughness of Ra = 5 μm, which we deem to be within acceptable boundaries in terms of causing possible inhomogeneities in the absorption spectrum.

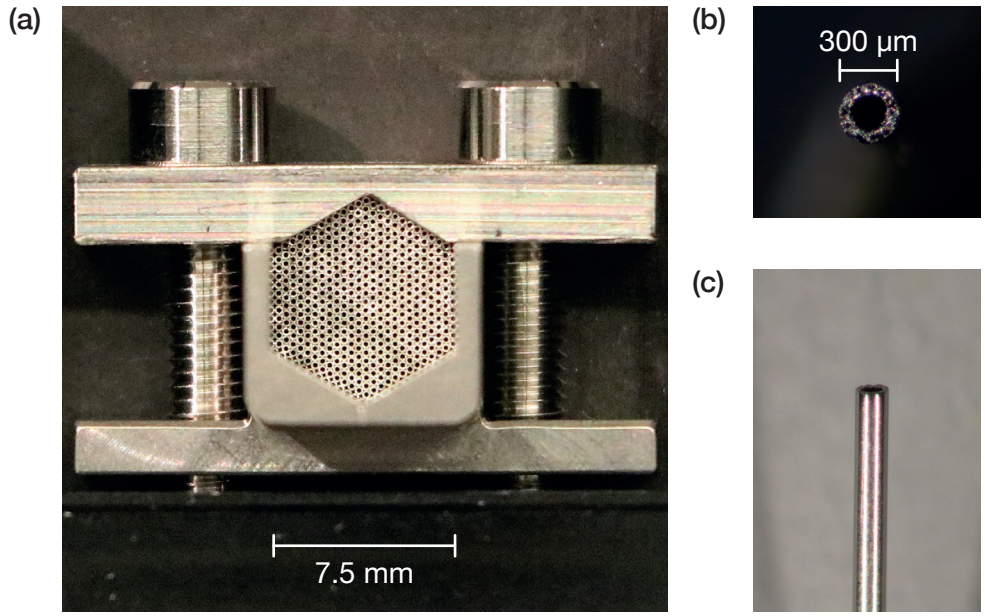

Figure 3.7 (a) The microcapillary array held by our hexagonal clamp. (b) One of our microcapillaries as viewed from the front. The roughness of the surface is visible as variations in the brightness of the capillary. (c) A side view of one of our capillaries, showing the vertical scale of the height imperfections observed in panel (b). Based on these two panels we estimate a surface roughness of Ra $\approx$ 5 μm.

The assembly process of the hexagonal capillary array, shown Fig. 3.7(a), proved to be a very tedious process. Each of the well over two thousand capillaries had to be individually placed into the clamping structure using a tweezer. For this procedure we constructed a custom mount with a lens to magnify the area of interest. This mount allowed for the tilting of the clamp into an almost vertical position to facilitate the dropping of the capillaries into the clamping structure once the clamp top had been screwed onto the clamp bottom and horizontal placement was no longer possible. Even so, it was difficult to distribute the pressure generated by the clamping mechanism equally across the entire capillary array, leading to individual capillaries sliding out of the nozzle when tilted or moved about vigorously. This problem was solved by carefully wet sanding the top clamp using P1000 grit sandpaper.

3.5 Insulation and Cooling

Without adequate insulation and cooling, the temperature generated by our oven is enough to heat the outside of our vacuum chamber to well above 100 °C. This is not only a health hazard, but also affects any optics or other temperature sensitive elements

of the experiment around the vacuum chamber. More importantly still, higher temperatures cause increased outgassing from our oven and consequently a higher pressure in the oven region. This is turn would limit the efficacy of our differential pumping and cause and increased pressure in our main chamber, causing a reduced vacuum lifetime of our atoms. As a result, we decided to surround our oven with two layers of heat shielding and to water cool the outside of our vacuum chamber. This cooling method is temporary and serves as a precursor to in-vacuum water cooling of our oven.

3.5.1 Heat Shields

The heat shields in our oven serve two interrelated purposes. On the one hand, they reduce the power consumption of our oven by reflecting part of the thermal radiation incident on their surface back to the oven. The amount of reflected heat depends on the emissivity of the heat shield. This quantity is defined as the ratio of the energy radiated from a materials surface to that radiated by a perfect blackbody at the same temperature and can be reduced by improving the reflectivity of the surface in question. On the other hand, a lower emissivity and higher reflectivity also ensure that less heat is transmitted through the heat shield therefore insulating the vacuum chamber walls from some of the heat of the oven. Stacking multiple heat shields concentrically further improves this behavior.

To improve the reflectivity of our heat shields we polished these to a mirror finish [see Fig. 3.8(a)]. This was achieved by successive sanding of the surface with ever finer sandpaper, beginning with dry sanding at P400 and moving to wet sanding for P800, P1000 and finally P2000 on a lathe. Afterwards, we polished the surface using polishing wool. Prior to this, a variety of other polishing methods had also been tested, including an acid bath and electropolishing. The latter method was attempted after having previously exposed out heat shields to temperatures of above 500 °C and yielded a matte finish. We assume that the exposure of the heat shield to these high temperatures in the oven led to a hardening of the surface and subsequently a failure of the metal to dissolve in the electrolyte.

The effect of our heat shields is visible in the power consumption of our oven, plotted in Fig. 3.8(b). The necessary power to generate an oven temperature of ≈ 750 °C is reduced by close to a factor of two with an additional outer heat shield. Additional heat shields manufactured from a material with a lower emissivity than steel would further reduce the power consumption of our oven.

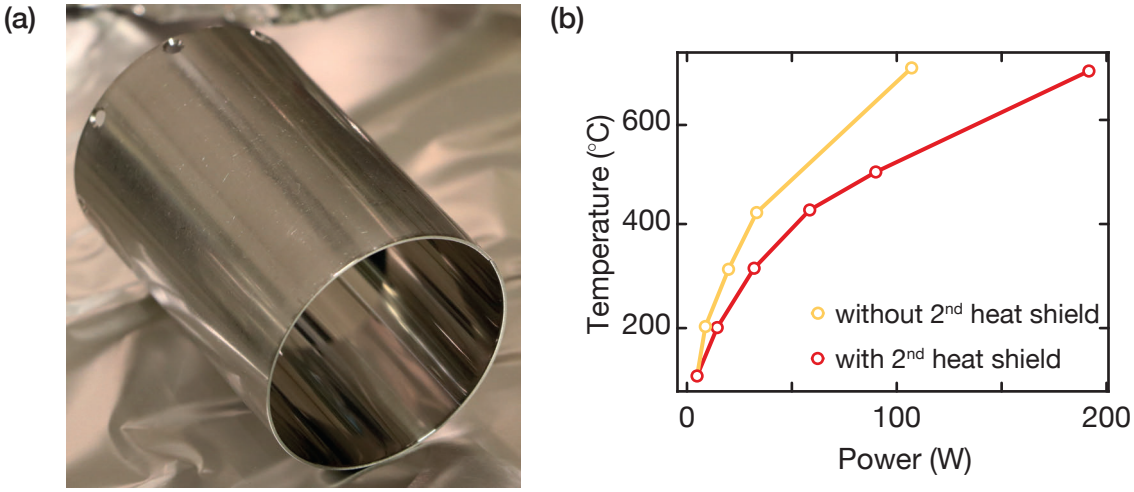

Figure 3.8 (a) The outer heat shield of our oven after successive sanding and polishing of its interior surface. Prior to the polishing process the interior and exterior surfaces had the same matte appearance. (b) A graph of the power necessary to achieve a given temperature with one and two heat shields. The addition of an extra heat shield reduces the power consumption by close to a factor of two.

3.5.2 Water Cooling

The water cooling of our vacuum chamber consists of 3 m of $\varnothing$=8 mm copper tubing which has been flattened by cold rolling the copper tubing to improve the thermal contact between the tube and the outside of the vacuum chamber. This maintains the chamber at a constant 23 °C at an oven temperature of $\approx$ 650 °C. Ideally, we want to do away with any cooling on the outside of the vacuum chamber and move to a purely in-vacuum water-cooled oven. This would lead to an increased vacuum lifetime of our atoms, as explained in the previous subsection.

A possible in-vacuum water cooling solution is illustrated in Fig. 3.9 and involves feeding water through one of the four steel supporting rods to the base plate and back through a second of the steel rods. This method would maintain the CF63 flange size for our oven while heating the base plate and by extension the outer heat shields of our oven.

Figure 3.9 A render of our baseplate for a possible in-vacuum water cooling solution.

With the conclusion of this chapter we have arrived at a working oven which can generate temperatures of more than 700 °C and temperature gradients of $\approx$ 90 °C between the crucible and the nozzle. The detachable nozzle design allows us test various capillary geometries and the associated theoretical predictions made for each of these in Chapter 2. Additionally, our crucible is able to hold 25 g of dendritic strontium in comparison to the 5 g capacity available in our current oven. Finally, a double layer of heat shields ensures a relatively low power consumption of 100 W at 700 °C. While certain challenges, such as in-vacuum water cooling, remain, we are now ready to test our oven by measuring the properties of the atomic beam emerging from its nozzle. To this end we require a laser, which will be the subject of the following two chapters.

Chapter 4

Laser Theory

In the preceding chapter we explained the construction of our oven. We now have an oven that is ready to be filled with strontium and tested, but no means to measure any of the characteristic features predicted in Chapter 2 For this we require a laser with which we can address our atoms. Before building such a laser, it is helpful to understand its basic properties and their origin. This chapter will therefore begin with a general quantum statistical model for a laser from which we can derive some of the main features common to all lasers, such as the lasing threshold and the linewidth. We will then move on to discuss the physics of semiconductor lasers, with a particular emphasis on blue laser diodes. These are of special interest to us, since we will be addressing the 461 nm $^1S_0 \rightarrow ^1P_1$ transition in strontium for both absorption spectroscopy and our 2D MOT. Once we have understood these theoretical aspects, we will move onto the construction of our laser in Chapter 5.

Before delving into our quantum statistical laser model, it is useful to develop some basic intuition for a laser. In Fig. 4.1 we show a typical laser diode which represents one possible realization of a laser. While other types of lasers exist, the three fundamental elements described in the following are shared by all lasers, irrespective of their construction. A laser diode is essentially a semiconductor with certain specific properties, the details of which will be discussed in Section 4.2. This semiconductor forms what is known as the gain medium of the diode. By applying a current to our gain medium we can, under specific conditions to be discussed in the following, cause the semiconductor to lase i.e. to emit coherent and monochromatic light. The process of applying a current to our semiconductor gain medium is called pumping. However, in order for the diode to lase, merely pumping the diode is not enough. We also require that both ends of the laser diode act as partially transmitting mirrors. These mirrors continually feed light of a particular frequency, emitted in the gain medium, back into the gain medium for amplification [50]. Such a partially reflecting set of mirrors is called an optical resonator and will be explored towards the end of this chapter (Section 4.3). Having developed our intuition for the three main features common to all lasers, we will now concentrate on building a mathematical model for our laser, which incorporates these three essential features.

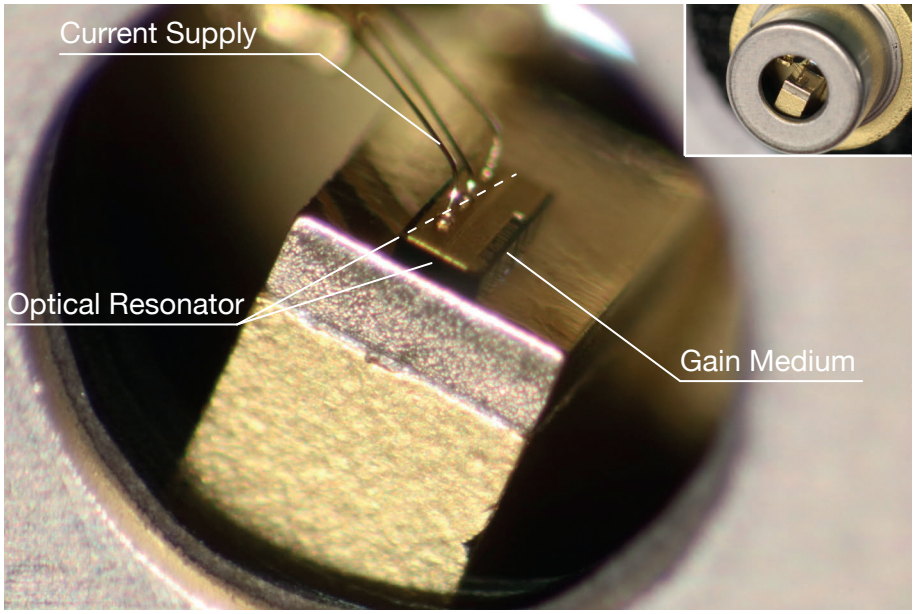

Figure 4.1 An image of a laser diode (Eagleyard: RWE-0690-00703-1000-SOT02-0000) taken with a microscope. The semiconductor gain medium is pumped by a current supply and bounded by two cleaved edges which act as partially transmitting mirrors and form an optical resonator. The inset shows the zoomed out version of this laser diode.

4.1 Lasers: An Open Quantum Systems Approach

A laser as described above is not an isolated system. Energy is fed into the gain medium by an external pump and some fraction of the laser's light has to be coupled out of the laser to be at all useful to experimentalists. A rigorous model of a laser must therefore take these external influences into account. As such, the laser is a good example of what is known as an open quantum system. Fundamentally, we expect such an open system to exhibit both well-controlled, deterministic processes as well as random, stochastic processes due to its coupling to the environment. How should we model such a system? Two alternatives present themselves.
The first exploits the probabilistic nature of the system to generate a rate equation for the probability density functions of the variables of our system. This type of equation is known as the Fokker-Planck equation [51] and can be generalized in a quantum mechanical sense by observing the evolution of the density matrix of our open quantum system. This generalized density matrix approach bears the name Lindblad master equation [52].
In the second alternative we are aided by the combination of deterministic and stochastic processes. This combination allows for a separation of the physical degrees of freedom (DOF) of the system into those evolving slowly and deterministically on the one hand and those evolving fast and stochastically on the other. The essence of this separation can be

captured in an equation of motion of the form:

$$\frac{dv(t)}{dt} = -\gamma v(t) + \eta(t) \tag{4.1}$$

where $v(t)$ is our variable of interest, $-\gamma v(t)$ regulates the deterministic evolution of the system, and $\eta(t)$ is called the noise term and describes any stochastic processes present. An equation of this kind is known as a Langevin equation and was first established in the context of Brownian motion of a particle with velocity $v(t)$, immersed in a fluid of microscopic particles [53]. In such a scenario, collisions with the microscopic particles occur in an uncorrelated manner. This is reflected in the moments of $\eta(t)$:

$$\langle \eta(t) \rangle = 0, \tag{4.2a}$$

$$\langle \eta(t)\eta(t') \rangle = 2D\delta(t - t'), \tag{4.2b}$$

where *D* is called the diffusion constant and gives the strength of the fluctuating force. A noise term obeying Eqs. (4.2) is called white noise.

In the following we will use this Langevin approach. However, since our laser system is expected to exhibit certain purely quantum mechanical behaviors, such as spontaneous emission, we will work with the quantum analog of the Langevin equation. This means our DOFs are given by a set of mutually non-commutative operators. Since we will treat our system quantum mechanically, it is sensible to first construct a suitable Hamiltonian for our laser. Our discussion will closely follow that of Ref. [52] and by extension that of Ref. [54].

The Hamiltonian of our laser consists of three parts (illustrated schematically in Fig. 4.2):

1. A harmonic oscillator describing a single mode of the light field

$$H_F = \hbar\omega_c a^\dagger a \tag{4.3}$$

confined in our optical resonator with a resonance frequency ω_c and some losses through the partially transmitting mirror is coupled to a heat bath consisting of the available modes of the electromagnetic field via a coupling:

$$H_{FB} = a^\dagger \Gamma_F + a\Gamma_F^\dagger, \tag{4.4}$$

where $\Gamma_F^\dagger$ (Γ_F) describes the creation (annihilation) of a bath particle, $a^\dagger(a)$ is the bosonic creation (annihilation) operator.

2. The atoms in our gain medium are modeled as a simple collection of two level systems (indexed by μ), held in an inverted state by some pumping mechanism.

$$H_A = \frac{1}{2}\sum_{\mu=1}^{N} \hbar\omega\sigma_z^\mu, \tag{4.5}$$

each coupled to an individual mode of the pumping bath via

$$H_{AB} = \sum_{\mu=1}^{N} \left(\Gamma_{A,\mu} \sigma_{\mu}^{+} + \Gamma_{A,\mu}^{\dagger} \sigma_{\mu}^{-} \right) \tag{4.6}$$

where $\Gamma_{A,\mu}^{\dagger}$ ($\Gamma_{A,\mu}$) again corresponds to the creation (annihilation) of a bath particle, $\sigma_z = |2\rangle\langle 2| - |1\rangle\langle 1|$ is the atomic inversion operator, and $\sigma^{+} = |2\rangle\langle 1|$ and $\sigma^{-} = |1\rangle\langle 2|$ are the atomic raising and lowering operators, respectively.

3. The atom-light coupling in the rotating-wave approximation approximation is described by:

$$H_{AF} = ig\hbar \sum_{\mu} \left(a^{\dagger} \sigma_{\mu}^{-} - a \sigma_{\mu}^{+} \right) \tag{4.7}$$

where g is the coupling constant between the cavity mode and a two-level system.

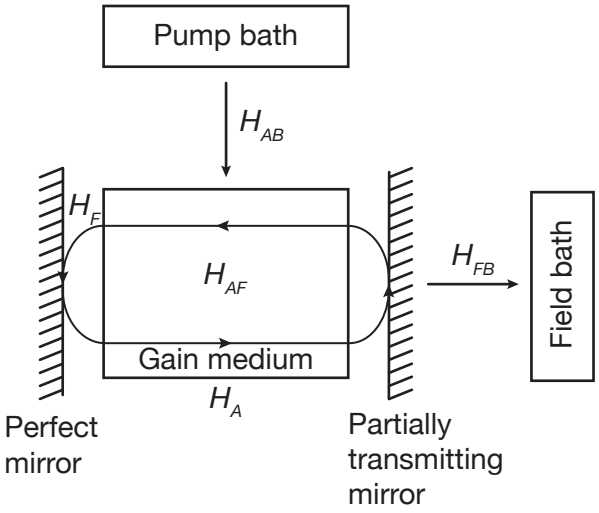

Figure 4.2 A schematic illustration of a laser as an open quantum system indicating the relevant constituents of our system Hamiltonian.

From this Hamiltonian it is possible to derive a quantum Langevin equation (the derivation can be found in Chapter 9.3.1 of Ref. [52]) which we can expand in orders of $\frac{1}{\sqrt{N}}$, where N is the atom number. In zeroth order we obtain:

$$\dot{\tilde{a}} = \kappa \tilde{a} + \tilde{g} \tilde{S}^{-}, \tag{4.8a}$$

$$\dot{\tilde{S}}^{-} = \tilde{g} \tilde{a} \tilde{S}_z - \gamma \tilde{S}^{-}, \tag{4.8b}$$

$$\dot{\tilde{S}}_z = -2\tilde{g} \left(\tilde{a}^{*} \tilde{S}^{-} + \tilde{a} \tilde{S}^{-*} \right) - 2\gamma \left(\tilde{S}_z - \overline{d} \right), \tag{4.8c}$$

where $\tilde{a} = \frac{a}{\sqrt{N}}$, $\tilde{g} = g\sqrt{N}$, $\tilde{S}^{-} = \frac{1}{N} \sum_{\mu} \sigma_{\mu}^{-}$, $\tilde{S}_z = \frac{1}{N} \sum_{\mu} \sigma_z^{\mu}$ and $\overline{d} = \frac{W_{12} - W_{21}}{W_{12} + W_{21}}$. The

coefficients W_{12} and W_{21} describe the rate of stimulated absorption and emission respectively. The parameter γ is the excited state population decay rate, κ is the cavity loss rate through the partially transmitting mirror, and g is the coupling constant defined in Eq. (4.7).
Together, Eqs. (4.8)form a set of coupled ordinary linear differential equations which are purely deterministic. Any stochastic contribution arising from noise is contained in higher orders of $\frac{1}{\sqrt{N}}$ which we omit for the moment.

4.1.1 The Lasing Threshold

First, let us analyze the stationary solutions to Eqs. (4.8), i.e. when $\dot{\tilde{a}} = \dot{\tilde{S}}^{-} = \dot{\tilde{S}}_z = 0$. In this case we obtain the following equation for our field operator, $\tilde{a}$:

$$\tilde{a}\left(1 - \frac{C}{1 + \frac{|\tilde{a}|^2}{n_0}}\right) = 0, \tag{4.9}$$

where $C := \frac{\overline{d}\tilde{g}^2}{\gamma\kappa}$ is known as the pump parameter and $n_0 := \frac{\gamma^2}{2g^2}$ is the saturation photon number. Equation (4.9) has two possible solutions, namely

$$\tilde{a} = 0, \tag{4.10a}$$

and

$$|\tilde{a}|^2 = n_0 \frac{C-1}{N}. \tag{4.10b}$$

Clearly the second solution in Eq. (4.10) is physical only if $C > 1$. We therefore have a transition between the two solutions, which we call the lasing threshold. The behavior of C above the lasing threshold is determined by the pumping in the form of $\overline{d}$.

4.1.2 The Laser Linewidth

We will now look at the time-dependent solutions of Eqs. (4.8) and expand to first order in $\frac{1}{\sqrt{N}}$. Before doing so, it is worth thinking about the various timescales of the system as defined by the constants γ, κ and $\tilde{g}$. In any useful laser we want the atomic decay rate γ to be dominant over all other timescales. If, for example, κ were the dominant decay rate, any light in the cavity would leak out before it had time to interact with the atoms and generate enough feedback to cause lasing. Therefore, assuming that $\gamma \gg \kappa, \tilde{g}$, any dynamics of the system involving γ cannot be resolved when measuring a quantity reliant only on κ and $\tilde{g}$. Applying this assumption to Eqs. (4.8), we can set the fast evolving DOFs

$\dot{\tilde{S}}^- = \dot{\tilde{S}}_z = 0$. Substituting the resulting equations into Eq. (4.8a) we are left with:

$$\dot{\tilde{a}} = -\kappa\tilde{a}\left(1 - \frac{C}{1+\frac{|\tilde{a}|^2}{n_0}}\right). \tag{4.11}$$

This process is an application of the principle of adiabatic elimination of variables [55].

Taking into account terms on the order of $\frac{1}{\sqrt{N}}$, Eq. (4.11) becomes

$$\dot{\tilde{a}} = -\kappa\tilde{a}\left(1 - \frac{C}{1+\frac{|\tilde{a}|^2}{n_0}}\right) + \frac{1}{\sqrt{N}}\eta(t). \tag{4.12}$$

This has the form of Eq. (4.1) with a Gaussian white noise term, $\eta(t)$, describing the stochastic processes in the system. We will now explore the effect of this noise term on our laser. For this purpose we can write our field operator as $\tilde{a} = \tilde{a}_0 + \epsilon$, where $\tilde{a}_0$ is the stationary solution described by Eqs. (4.10), and ϵ is the fluctuating part of the field due to the addition of the noise term in Eq. (4.12).

Below Threshold

Below threshold, $\tilde{a}_0 = 0$ and Eq. (4.12) is given by

$$\dot{\epsilon} = \kappa\epsilon + \frac{1}{\sqrt{N}}\eta(t) \tag{4.13}$$

in lowest order of ϵ. This is an inhomogeneous first-order differential equation and as such has the solution

$$\epsilon(t) = \epsilon_0 e^{-\kappa t} + \frac{1}{\sqrt{N}}\int_0^t dt' e^{-\kappa(t-t')}\eta(t'). \tag{4.14}$$

In the limit of $t \to \infty$ and using Eq. (4.2b), its autocorrelation is then given by

$$\langle \epsilon^\dagger(t)\epsilon(t+\tau)\rangle = \frac{D}{\kappa N}e^{-\kappa|\tau|}. \tag{4.15}$$

Such an exponentially decaying autocorrelation function is characteristic of a thermal light source. We can therefore say that below the lasing threshold our laser behaves as a thermal lamp.

Above Threshold

Above threshold, it is useful to separate the stochastic processes represented by $\eta(t)$ into those affecting the amplitude of our field, η_A, and those affecting its phase, η_ϕ.

The physical origin of the phase fluctuations of our field lies in the process of spontaneous emission. This process is described by the Wigner-Weisskopf theory and results from the atom-field coupling quantified by our coupling constant, g. Since each photon emitted via spontaneous emission carries with it a random phase, the phase of our field will perform a random walk in time. The central limit theorem tells us that over many such spontaneous emission events the phase will become normally distributed and may be modelled by a Wiener process [56], $W(t)$, obeying

$$W(t) = \int_0^\tau d\eta_\phi(\tau). \tag{4.16}$$

To reflect the fact that we are considering the effect of phase modulation on our field, we write our field operator as $\tilde{a}(t) = \tilde{a}_0 e^{i\phi(t)}$, where $\tilde{a}_0$ is the stationary solution above threshold, i.e. Eq. (4.10b), and $\phi(t)$ is the fluctuating phase of our field. This leads to an autocorrelation function of the form

$$\langle(\tilde{a}^\dagger(t)\tilde{a}(t')\rangle) = |\tilde{a}_0|^2\langle e^{i(\phi(t')-\phi(t))}\rangle. \tag{4.17}$$

Since we know that $\phi(t)$ obeys a Wiener process, we can write

$$\phi(t) - \phi(t') = W(t), \tag{4.18}$$

and therefore

$$\langle(\phi(t) - \phi(t'))^2\rangle = 2\tilde{D}\,|t - t'|\,, \tag{4.19}$$

with a diffusion constant, $\tilde{D}$. Furthermore, since $\phi(t) - \phi(t')$ is Gaussian we can make use of the following property [56],

$$\langle e^{\phi(t)-\phi(t')}\rangle = e^{\frac{1}{2}\langle(\phi(t)-\phi(t'))^2\rangle}, \tag{4.20}$$

and thus

$$\langle\tilde{a}^\dagger(t)\tilde{a}(t')\rangle = n_0\,(C-1)\,e^{-\widetilde{D}|t-t'|}. \tag{4.21}$$

By the Wiener-Khinchin theorem [57], the Fourier transform of our autocorrelation function yields the power spectral density, $S_\omega(\omega)$, of the frequency fluctuations of our field

$$S_\omega(\omega) = \frac{2}{\tilde{D}}\frac{1}{1+\left(\frac{\omega}{\tilde{D}}\right)^2}, \tag{4.22}$$

which is a Lorentzian with a full-width at half maximum (FWHM) proportional to the diffusion constant, D. Note that in the case of a constant field without phase fluctuations, we would observe a constant autocorrelation, indicative of a perfectly coherent light source. We can therefore conclude that a phase diffusion process due to spontaneous emission leads to an exponential decay of the coherence time of our laser, as given by the autocorrelation function Eq. (4.21). This is equivalent to a broadening of the laser linewidth into a Lorentzian with a FWHM $\propto \tilde{D}$.

4.2 Laser Diodes

Our open quantum systems approach has allowed us to derive features that are shared by all lasers, irrespective of their particular construction and material properties. We will now move on to look at the specifics of diode lasers and derive properties unique to this class of lasers.

4.2.1 p-n Junctions

Of critical importance to the topic of semiconductor lasers is the concept of material doping. Doping is the deliberate introduction of impurities into a material of high purity. An impurity in this case may be defined as any particle differing from those present in the pure material. For our purposes it is useful to distinguish between two different types of impurities. A material containing an excess of electrons (or donors) is said to be n-doped. In contrast, a material lacking electrons is said to be p-doped. This lack of electrons can also be seen as an excess of holes (or acceptors), which are identical to electrons, but possess the opposite charge. At its most basic, the laser diode is a junction between an n-doped substrate and a p-doped layer which has been grown onto this substrate. When a forward bias current is applied to the p-n junction via two electrodes at either end of the diode, an active region is created in the intrinsic material. Electron-hole recombination in this region leads to stimulated emission and lasing from the diode [58].

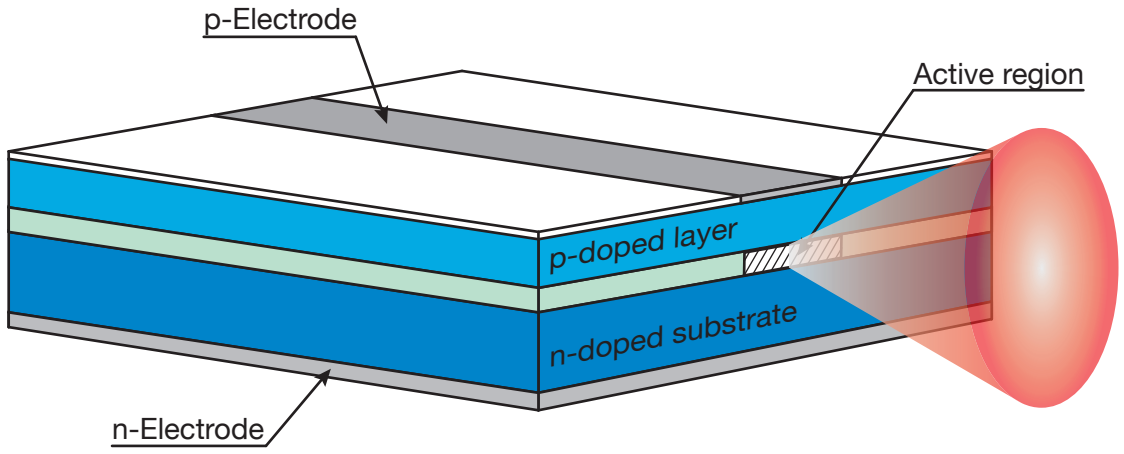

Figure 4.3 A simplified illustration of a laser diode showing the main features contributin to lasing. Adapted from Ref. [59].

Band Structure

The overlap of atomic orbitals in a solid results in a splitting of individual atomic orbitals into a large number of molecular orbitals each with a different energy. The large number of atoms guarantees an effective continuum of allowed electron energies known as a band. Depending on the separation between atoms, certain energy ranges between bands are not occupied by any electrons. We call these unoccupied regions bandgaps. The highest energy band where all energy levels are still occupied is called the valence band and the next highest, the conduction band.
According to this band structure we my classify solids into insulators and conductors. In an insulator electrons occupy the valence band, but the bandgap is large enough to prevent any excitation to the conduction band under the application of conventional voltages. The electrons are therefore immobile and no current can flow in the insulator. By contrast, electrons in a conductor are free to move across the bandgap since this is usually very small or even nonexistent.

A semiconductor is a material which displays insulating behavior at $T = 0$K, but whose bandgap is small enough for thermal excitations to cause conductivity in the material at non-zero temperatures [60]. In a semiconductor we can distinguish between two types of bandgap. A direct bandgap occurs if the position of the conduction band edge is at the same point in $\mathbf{k}$-space as the valence band edge. For an indirect bandgap this is not the case and conservation of momentum requires the participation of a phonon in the transition process between valence band and conduction band.

With these definitions in mind, let us now turn to the process of lasing in a p-n junction. For lasing we need to achieve a population inversion (see subs. 4.1.1). This means that we require a region in our junction where there exists a higher density of electrons in the conduction band than in the valence band. If we bring our p and n-doped semiconductors together, the difference in Fermi levels between the two semiconductors leads to diffusion of charge carriers across the junction until the Fermi levels equilibrate. This steady-state is illustrated in Fig. 4.4(a). Applying a forward-bias voltage to our junction results in a corresponding shift in the Fermi levels of electrons and holes. When this voltage is equal to the bandgap potential, an active region is formed in our junction where we have both electrons in the conduction band and holes in the valence band (Fig. 4.4(b)). This is the required population inversion for lasing. Light incident on the electrons in the conduction band can cause these to recombine with the holes in the valence band. This process results in the release of an identical photon to the one that caused the recombination. This process is known as stimulated emission. The optical resonator mentioned in the introduction to this chapter causes some of this stimulated emission to be fed back into the active region, resulting in further stimulated emission processes and amplification of the light.

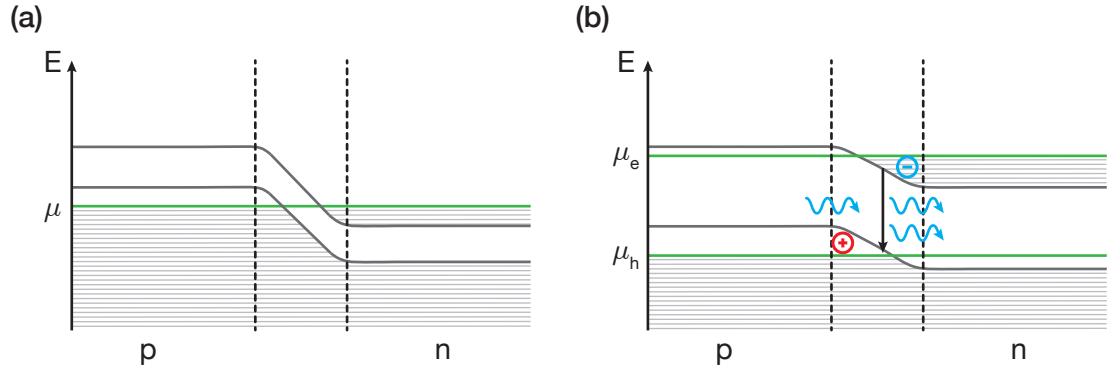

Figure 4.4 (a) The band structure of a p-n junction without the application of a forward-bias voltage, showing a constant Fermi level. (b) The application of a forward-bias voltage leads to a population inversion, enabeling electron-hole recombination via stimulated emission. Adapted from Ref. [61].

From the above description of the lasing threshold it is clear that an electron-hole recombination involving an indirect bandgap in the active region is less efficient than a recombination process at a direct bandgap, since the former involves the emission of a phonon. To increase their efficiency, laser diodes should therefore be manufactured with a direct bandgap in the active region.

Heterojunctions

Continuing along the line of laser diode efficiency, we come to the topic of heterojunctions. These types of junctions are generated when two dissimilar semiconductors are brought together as a p-n junction. The difference in conduction and valence band potential energies between the semiconductors leads to discontinuities in the bands at the junction. These discontinuities can be exploited to increase the efficiency of the laser diode in the following fashion:
If we create two such discontinuous junctions in succession, we will be left with an active region bounded on both sides by discontinuities, as illustrated in Fig. 4.5(a). This is what is known as a double heterostructure. Applying a forward bias current to such a structure leads to the confinement of charge carriers in the bounded region, an effect called charge confinement (Fig. 4.5(b)). The great advantage of the double heterostructure is the ability to engineer the width of the active region. This leads to a higher carrier density in the active region for the same current when compared to a homojunction of the type illustrated in 4.4. As we know from our discussion of the lasing threshold, the gain, C, depends on the pumping $\overline{d}$ and by extension the population-scaled rates of stimulated emission and absorption (4.10b). These rates, in turn, depend on the carrier density. A higher carrier density in the active region therefore results in a higher gain. Finally, this means that a double heterostructure reduces the lasing threshold of our laser, thereby increasing its efficiency [58].

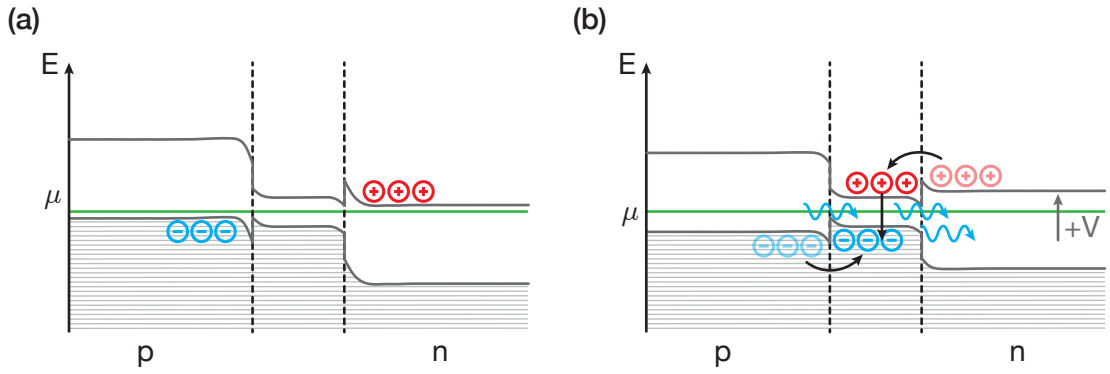

Figure 4.5 (a) A double heterostructure is created by joining two heterostrucutres created at the interface of dissimilar semiconductors. The junction is marked by an active region bounded on both sides by discontinuities. (b) An applied forward-bias voltage leads to charge confinement in the active region. For very narrow active regions this leads to a high charge-carrier density and consequently a higher gain.

Quantum Wells

Reducing the width of the active region of a double heterostructure junction to values on the order of the de Brogile wavelength of the electrons leads to a discretization of the energy levels in the active region. In such a scenario the active region is said to form a quantum well. As before, the reduced width of the active region improves the efficiency of our laser diode by reducing the lasing threshold. In addition, however, the quantum well structure is also less sensitive to temperature fluctuations. In a bulk double heterostructure, the continuum of available states in the active region means that any change in temperature leads to changes in energy of the electrons/holes via intraband phonon transitions. Consequently, even small changes in temperature affect the carrier distribution in the active region and hence the maximum gain of our diode. In a quantum well, this behavior is suppressed since phonons transitions now require a certain fixed energy [59].

4.2.2 Blue Laser Diodes

We are now in possession of all the necessary ingredients to understand the distinctive nature of blue laser diodes. Our first requirement in the manufacture of a blue diode is a direct bandgap semiconductor with a bandgap energy corresponding to wavelengths in the blue and ultraviolet. A prime candidate fulfilling these criteria is gallium-nitride (GaN) with a direct bandgap energy of ≈ 3.4 eV [62]. Almost immediately, however, we encounter our first problem.

Growing GaN

Finding a suitable substrate on which to grow GaN is difficult. GaN grows in a wurzite crystal structure (a type of hexagonal crystal system) and has a large lattice mismatch with a range of substrates. A mismatch between the lattice constants of GaN and its substrate introduces stresses into the former resulting in a cracked surface. Nevertheless, smooth GaN growth was first demonstrated on a substrate of sapphire despite a mismatch of ≈ 16 % and ≈ 25 % between their lattice constants and thermal expansion coefficients respectively [63]. This was achieved with the help of a AlN buffer layer and the use of metal organic chemical vapor deposition (MOCVD). The AlN layer acts as an adapter between the two crystal structures. and the MOCVD method allows for a steady growth speed and deposition of high purity GaN on the substrate.

Doping GaN

A second problem is posed by the need to p-dope GaN such that it can form a p-n junction with the n-doped sapphire substrate. It was found that the irradiation of Mg-doped GaN by a low energy electron beam resulted in better p-doping properties of GaN [64]. This effect can be explained in the following manner: Hydrogen, decomposed from ammonia during the MOCVD process, passivates Mg acceptors by forming Mg-H complexes (a complex is simply an atom or ion that is covalently bonded to a number of surrounding molecules or ions). The subsequent irradiation of this complex by an electron beam results in the dissociation of hydrogen. An equivalent effect can also be achieved via heat treatment of the Mg-doped GaN [65]. This method of p-doping can be extended to the doping of heterostructures and quantum wells, ensuring an efficiency great enough for a functioning laser diode [66].

Effects on Characteristic Laser Quantities

The above methods for growing and doping blue laser diodes also have implications for the light emitted by these diodes. For example, a large lattice mismatch between the layers in a quantum well diode can lead to a distortion of the active region and a skew in the electron-hole distributions. This in turn reduces the optical gain as well as the spontaneous electron-hole recombination rate [67]. Another difficulty is the manufacture of low-restistance Ohmic contacts to the p-doped layer of the laser diode. Such contacts are necessary to prevent excessive heating of the diode which would lead to a reduced lifetime and reliability. This problem arises due to the lack of metals with a high enough work function to overcome the potential barrier preventing hole injection [68] and is an ongoing area of research [69].

4.3 Optical Resonators

So far we have been focused on the material properties of the laser diode and only touched upon feedback in very general terms when deriving the lasing threshold and emission spectrum of a laser using our open quantum systems approach. As was mentioned in that section, a laser diode has cleaved facets which form what is known as an optical resonator (or optical cavity). Such an optical resonator is necessary to provide the optical feedback that allows for stimulated emission and amplification in the gain medium of a laser. An optical resonator is defined by a set of mirror surfaces which allow light to circulate in a closed path and supports two types of modes for the light circulating between its mirrors [70].

4.3.1 Longitudinal modes

For simplicity, let us assume that our optical resonator consists of two perfectly flat, partially transmitting mirrors with reflectivity, R_1, R_2, and transmissivity T_1, T_2 respectively. These are separated by a distance, L with the space between the mirrors having uniform refractive index, n (this type of resonator configuration is known as a Fabry-Pérot interferometer and is illustrated in Fig. 4.6(a)). Only light which, after a round-trip between the mirrors, is in-phase with new light entering the resonator will build up in said resonator. This condition is known as the round-trip phase matching condition and is expressed mathematically as

$$2Lkn = q2\pi,\ q \in \mathbb{N}, \tag{4.23}$$

where $k = \frac{2\pi}{\lambda}$ is the wavenumber. Solving Eq. (4.23) for the frequency of the light, ν, gives rise to a set of resonant frequencies

$$\nu_q = q\frac{c}{2nL}, \tag{4.24}$$

separated by a distance

$$\nu_{\text{FSR}} = \frac{c}{2nL} \tag{4.25}$$

called the free spectral range (FSR) of the cavity. Owing to resonator losses through the partially transmitting mirrors, T_1 and T_2, as well as scattering losses due inhomogeneities in gain medium [70], the field amplitude of the light circulating in the resonator is reduced upon every roundtrip by an attenuation factor, $|r|$. Summing the intensities of the light over every roundtrip results in a geometric series, which can be written as

$$\frac{I_{\text{max}}}{1 + \left(\frac{2\mathcal{F}}{\pi}\right)^2 \sin^2\left(\frac{\phi}{2}\right)},\ I_{\text{max}} = \frac{I_0}{\left(1 - |r|\right)^2}, \tag{4.26}$$

where $\phi = 2knL$ is the phase difference acquired by the light in every roundtrip and I_0 is the initial intensity. The quantity

$$\mathcal{F} = \frac{\pi\sqrt{|r|}}{1-|r|}, \tag{4.27}$$

is called the finesse and together with the FSR determines the spectral width, $\delta\nu$, of the cavity resonances via

$$\delta\nu \approx \frac{\nu_{\text{FSR}}}{\mathcal{F}}. \tag{4.28}$$

As was demonstrated in Subs. 4.1.1, the intensity of the light increases as a function of the pumping, characterized by the pumping parameter, C. Thus, the light experiences some gain in the medium which can be described by defining a gain coefficient, $g(\nu)$, in the following manner [71]:

$$g(\nu) := \frac{C\,|T_1 T_2|}{L}. \tag{4.29}$$

In addition to the gain, we can describe the above mentioned resonator losses by a loss coefficient, $\alpha_r = \alpha_s + \alpha_m$, where α_s represents scattering losses and α_m losses through the mirrors. Using these gain and loss coefficients we can formulate an alternate definition of the lasing threshold to that of Subs. 4.1.1, namely that the lasing threshold is reached when $g(\nu) = \alpha_r$, i.e. when the gain in the medium is equal to the losses of the resonator. Consequently, only those resonator modes contained within the lasing frequencies allowed by the gain curve $g(\nu)$ will be amplified. This is shown in Fig. 4.6(b).

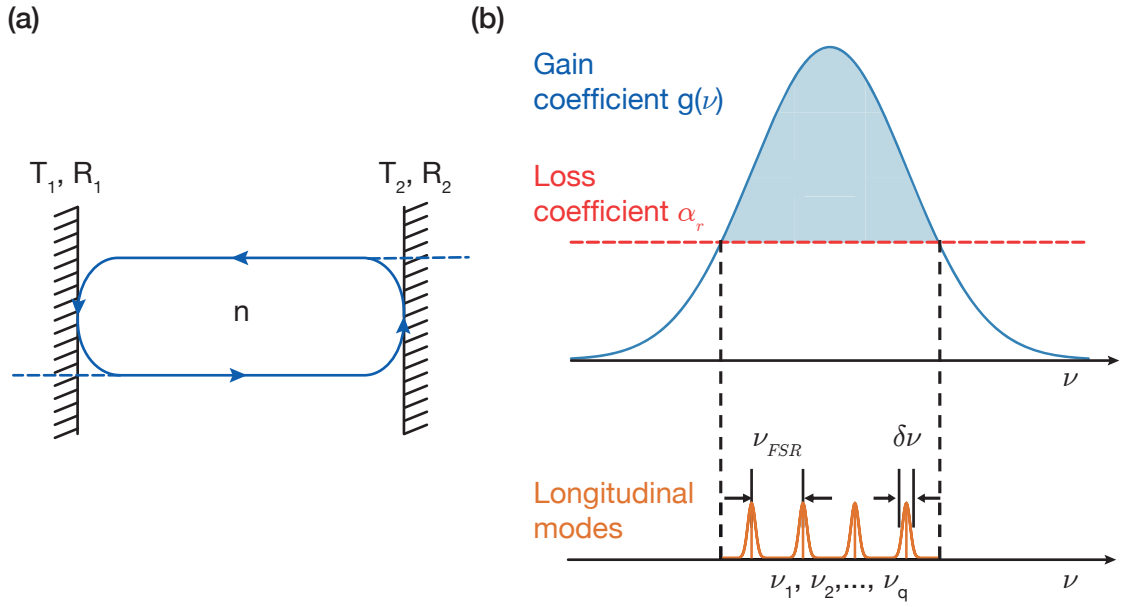

Figure 4.6 (a) Light circulating in a medium of refractive index n, bounded by pair of flat mirrors with transmittivity $T_{1/2}$ and reflectivity $R_{1/2}$ forms an optical resonator known as a Fabry-Pérot interferometer. (b) The light circulating in this resonator obeys the round-trip phase matching condition, which gives rise to a set of resonance frequencies of the resonator, ν_q which are seprated by the free spectral range ν_{FSR}. For a laser gain medium with a gain coefficent $g(\nu)$ and loss coefficient α_r, only those resonator modes lying above the threshold $g(\nu) = \alpha_r$ are amplified. Adapted from Ref. [72].

4.3.2 Transverse modes

In addition to the frequency of our light, we can also explore the behavior of the field distributions in our cavity. In this case, geometric properties such as the shape of the mirrors have a large effect on the shape of the resonant field distributions. Looking to the laser diode, it can be shown that the difference in refractive indices between the cladding layers and the active region leads to a cosine distribution in the latter with exponentially decaying wings in the former [59]. We can further distinguish the distribution of the $E_{\parallel}$ component of field, known as the TE mode and the $E_{\perp}$ component known as the TM mode.

Usually, the TM mode has less overlap with the gain medium than the TE mode, due to the narrowness of the active region. This means that the TE mode experiences a higher gain and begins to lase first. As a result, most laser diodes preferentially amplify $\parallel$-polarized light. This effect is enhanced in blue diodes, since the quantum well structure of their active region makes it easier for $E_{\parallel}$ light to stimulate electron-hole recombination [73]. Additionally, the narrowness of the active region in the vertical plane also leads to

diffraction of the light at the facet and hence an elliptical beam that is longer in the vertical direction than in the horizontal direction. This illustrated in Fig. 4.3.

Chapter 5

Linear External Cavity Diode Laser

Having previously discussed the theoretical aspects of diode lasers, we will now describe how to realize such a laser in the lab and how to characterize its properties. As explained in previous chapters, we will interrogate our atomic beam using absorption spectroscopy, which calls for a source of 461 nm light that can be scanned over a large range of detunings. Additionally, we want to combine our new atomic oven with a 2D MOT to increase its efficiency beyond the factor already provided by varying the capillary geometry (see Chapter 2 for details). To this end we require laser light with sufficient intensity to compress the atomic beam to the required size (for a quantitative analysis see Chapter 1). The laser presented in this chapter is intended to provide light for both of these applications.

Our design is that of an diode laser with a linear external cavity (ECDL) and a wide bandwidth interference filter as a wavelength-selective element. A general benefit of a such a linear ECDL is its effective decoupling of the wavelength selection from the optical feedback degree of freedom. This results in a greater tunability of the laser compared to e.g. a Littrow laser. In addition, the output coupler can be coated for a broad range of wavelengths, whereas the grating in a Littrow configuration is optimized for one specific wavelength. Finally, the linear design of the external cavity reduces the effect of cavity length variations on the frequency of the laser, since any horizontal compression or expansion of the cavity has no effect on the optical path length. The latter point was of particular interest to us, since the direct coupling of the external cavity of our current generation of home-built Littrow lasers to the environment led to substantial frequency jitter (for more information see Appendix. C).

The essential features of our ECDL design are captured in Fig. 5.1. Light emitted by the laser diode is collimated by a lens within the collimator before it passes through the interference filter and is focused onto the output coupler by an aspheric lens ($f = 18.4$ mm). Together, these optical elements define the external cavity of our laser. The light is out-coupled by the output coupler and re-collimated by a final lens of identical focal length to the first. All these optics are contained in a monolithic aluminum mount resting on two Peltier elements, which, together with a thermistor, temperature stabilize the laser diode. This assembly is itself contained withtin a large outer housing designed to be evacuable via a KF gasket in the lid. We will touch upon each of these essential features

in more detail in the description of the construction process to follow. A full parts list is provided in Appendix. C.

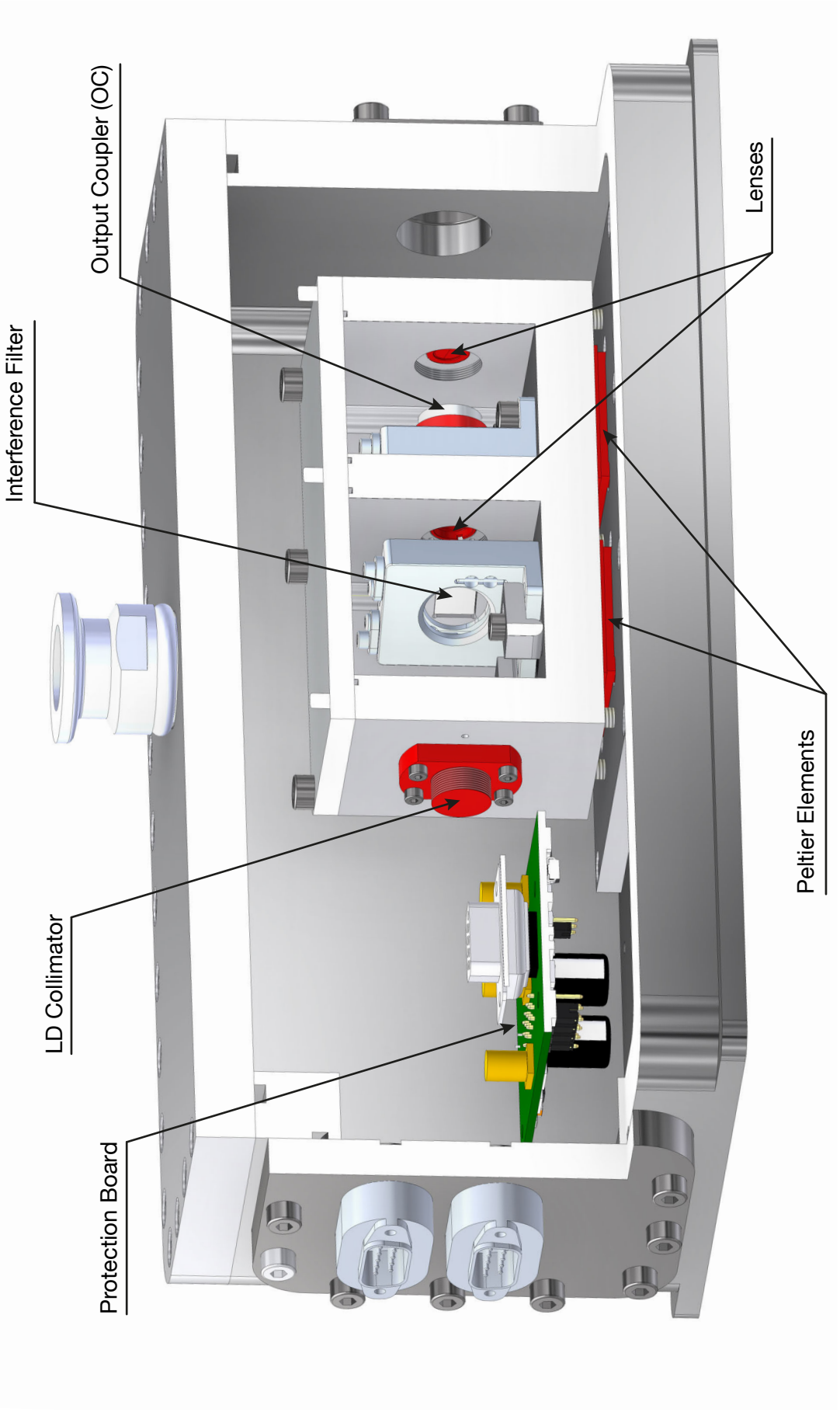

Figure 5.1 Render of our linear ECDL. The external cavity is defined by the back facet of the LD in the collimator and the front of the OC. The wavelength of the laser can be tuned via the IF and the diode is temperature stabilized with a thermistor and two Peltier elements. The large, hermetically sealed outer housing ensures frequency stability.

5.1 Construction Process

The construction of the ECDL was divided into three main areas:

- Gluing and assembly of the housing
- The protection board and associated electronics
- Assembly and alignment of the optics

Prior to construction almost all constituent mechanical parts of the laser were thoroughly cleaned to vacuum standard with the exception of the Newport mounts (HVM-05r). Together with the electronics (including the piezo [Piezomechanik GmbH, HPCh 150/15-8/3], the Peltier elements [RS, 490-1480, 32.8] and the thermistor [EPCOS NTC Thermistor, 10 kΩ]), these were separately cleaned with isopropanol and a wipe due to the possibility of incurring damage during the sonication process and, with regards to the Newport mounts, the likelihood of residual pockets of water in the grub screws and springs failing to dry within a reasonable time frame. For a detailed account of the cleaning procedure see Ref. [74].

Additionally, we decided to test whether we could use a simple beam-splitter plate from Thorlabs as an output coupler, instead of an anti-reflection coated mirror. This would be both significantly cheaper and faster (the coating itself would have taken several weeks). Consequently, we ordered beam splitter plates with three separate reflection to transmission ratios and measured the reflected power. The results are recorded in Tab. 5.1 for both 633 nm and 461 nm.

Table 5.1 The reflected output power as a percentage of input power for three different beam splitters with varying reflection/transmission (R:T) ratios.

461 nm		633 nm	
R:T	P_{ref}/P_{in} (%)	R:T	P_{ref}/P_{in} (%)
50:50	43.88	50:50	48.81
30:70	29.18	30:70	27.50
10:90	7.82	10:90	7.77

We also tested the anti-reflection coating of the beam splitter plates by measuring the reflected power from the back surface of the plate. In both cases the secondary reflection amounted to $< 0.1\%$ of the input power. Based on an experimentally determined optimal feedback of 30% [75] and the above results we initially decided to use the 30:70 beam splitter plate (BSS04) as the output coupler in our lasers. However, it was later found that a feedback of only 10% gave a larger range of currents at which a stable single-mode operation could be achieved and we subsequently switched to this output coupler.

5.1.1 Gluing and Assembly of the Housing

Since certain components required the application of epoxy glues with a specific curing time, we addressed these first. The output coupler had to be glued to the piezo, which in turn had to be glued to the piezo adapter. The glue required for this is TorrSeal, which is a two-component glue with a mixing ratio of 100:40 by weight and an effective (90%) curing time of 24 hrs at 25 °C (this can be sped up by exposure to higher temperatures - see [76] for details). TorrSeal can be used at pressures up to 10^{-8} mbar, which would allow us to evacuate the laser, increasing its stability by reducing air pressure fluctuations as well as preventing impurities in the air form burning into the output coupler. The glue was applied at three equidistant spots around the circumference of the output coupler and covered the piezo and coupler in equal amounts [see Fig. 5.2(a)]. Similarly, the glue between the piezo and its adapter was also applied at three equidistant spots on the piezo surface. To prevent a possible reduction in the optical feedback caused by an expansion of the glue onto the surface of the output coupler, care was taken not to apply too much glue in one spot.

A good strategy for this procedure is described in Ref. [77] and involved placing the output coupler onto several layers of optical paper, followed by the piezo and then the piezo adapter. The three components were then weighed down by an optics post to prevent differential expansion of the glue and a subsequent tilting of the output coupler. The glue was applied with a thin piece of wire, though a needle works equally as well. When placing the output coupler, care was taken to ensure its correct orientation. The direction of light transmittance (as indicated by an arrow on the side of the coupler) should face downward onto the optical paper so that when all components had been glued together and mounted in the Newport mounts, the output coupler would face the right way.

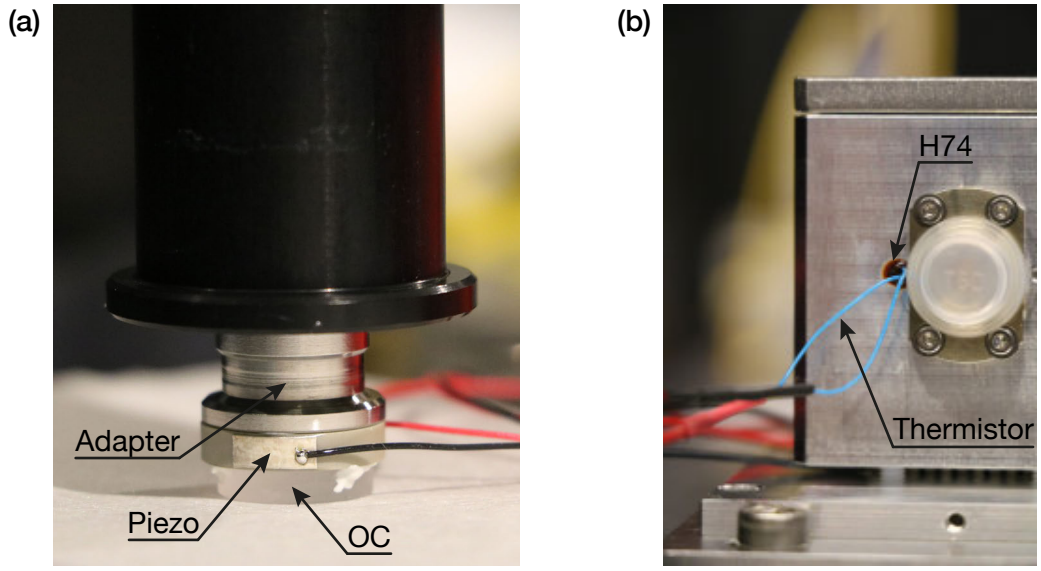

Figure 5.2 (a) The gluing method for the OC described in [77]. (b) The mounting and gluing of the thermistor to the inner housing of our laser. The EPO-TEK H74 has turned dark red after baking at 150 °C for 1 h.

A second component requiring the application of glue was the thermistor. The thermistor had to be glued to the housing of the laser using EPO-TEK H74 thermally conductive epoxy to ensure a fast temperature response which would enable a more sensitive and accurate temperature control of our diode. Again, this is a two component glue with a mixing ratio of 100:3 by weight. The hole for the thermistor should be 3 mm in diameter. In our case additional drilling was required to bring this hole up to the correct size. After curing in the oven for 1 h at 150 °C the glue should turn a dark red [see Fig. 5.2(b)].

5.1.2 The Protection Board and Associated Electronics

The protection board for our ECDL is designed to minimize possible noise sources on the laser light and to protect the LD from incorrect driving currents or voltage spikes. It also acts as an intermediary between the Toptica/Thorlabs control units and their dependents (the laser diode, thermistor and peltier elements). The laser diode is isolated from high frequency noise via a series of a bypass capacitors (C1-C4) and from incorrect driving currents by a Schottky diode (MBRO540) in parallel with the laser diode. Additionally, a relay circuit protects the laser diode from static electricity [Fig. 5.3(c)]. For further details see Ref. [36].

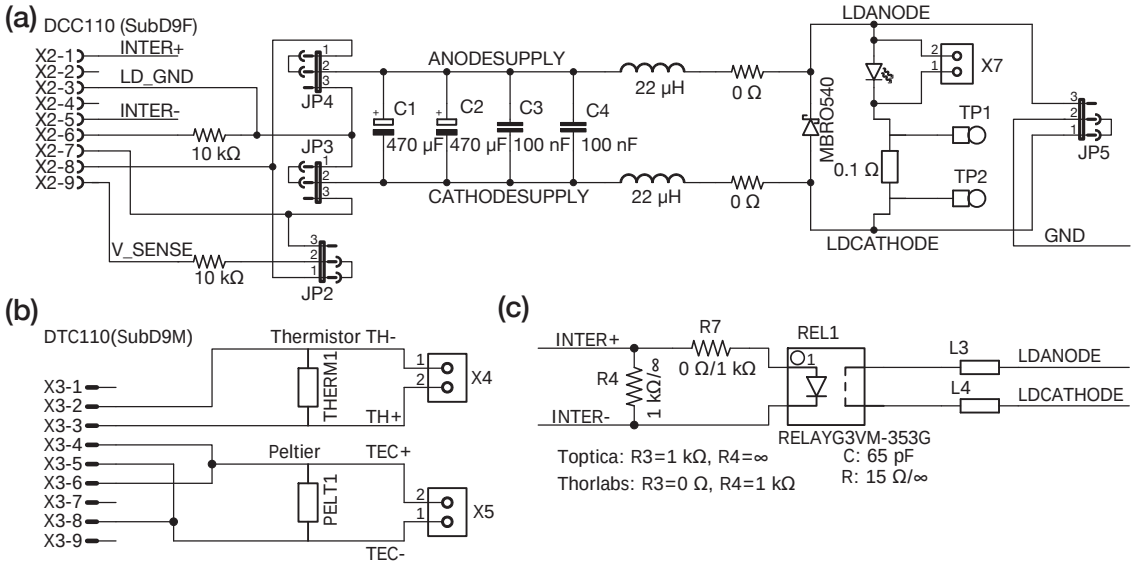

Figure 5.3 (a) A schematic of the current supply part of our protection board. The LD is protected from noise and incorrect driving currents by a series of bypass capacitors (C1-C4) and a Schottky diode (MBRO540) respectively. (b) The temperature control unit of the protection board. (c) A schematic of the relay designed to protect the LD from static electricity. Note the Toptica/Thorlabs controller dependent resistances R3 and R4.

Care was taken to check the polarity of the laser diode and the corresponding jumper settings (JP2 - JP4, shown in Fig. 5.3(a) for a cathode grounded LD). Additionally, we checked that the polarity setting on the actual current controller corresponded to the setting on the board. An incorrect polarity could lead to a reverse breakdown of the diode where mobile charge carriers in the diode can knock bound charge carriers free, causing an avalanche effect and permanent damage to the diode.

As a final step, we soldered the thermistor and the Peltier elements to the PCB and tested the polarity by placing the Peltier elements in place without fixing them, switching on the temperature controller and observing the actual temperature. If the temperature begins to drift away from the setpoint, the polarity needs to be inverted. Having ensured the correct polarity, we placed a small amount of heat paste on each Peltier indentation in the base plate and fixed the inner housing to this plate using the nylon screws. These screws ensure that the only efficient heat exchange occurs at the contact between the inner housing and the Peltier elements.

Some compatibility issues between the housing and the electronics became apparent during this stage of the construction process. Firstly, the backplate of the outer housing was lacking feedthroughs for the scan control and DC modulation. For the scan control we drilled a hole into the backplate, placed two electrical contacts through this hole and sealed it with TorrSeal. The DC modulation feedthrough is still outstanding. Additionally,

the housing cannot be evacuated due to the vacuum incompatibility of the electrolytic capacitors on our protection board. A future iteration of this laser should therefore aim to place the PCB on the outside of the housing.

5.1.3 Assembly and Alignment of Optics

Since the outer laser housing limits access to the collimator alignment screws, the entire assembly and alignment of the optics took place outside the housing. For the purpose of achieving the standard 50 mm beam height in our lab (determined by the height of the laser output from our Toptica DL Pro lasers), we cleaned a 20 mm aluminum plate to vacuum standard and fixed the inner housing on top of this plate.
The assembly process itself began with the delicate task of placing the laser diode (Nichia NDB4216) into the collimator (Schäfter-Kirchhoff 20C-A4.5-01). Since detailed instructions can be found at [78] we will only highlight two problems which we encountered during this process. One was the inability of the fixing ring to hold the laser diode tightly enough to compensate for any pulling force from the wire, yet loose enough to allow for the rotation of the diode. For a next iteration of this laser, we recommend implementing a simple strain relief solution for the wires leading to the diode, such that that it may be rotated without any back-action. The second was the lack of space for the grub screws that fix the retaining ring, once the plug for the laser diode pins had been placed on the end of the collimator. Here, a simple fix was to trim the plug down to the required circumference using a razor blade.

For the purposes of alignment, the current to the laser diode was increased to a few mA beyond the lasing threshold of the bare diode (without optical feedback), such that the elliptical emission from the diode was clearly visible. After we fixed the collimator in place, we rotated the laser diode to match the polarization axis to the one favored by the interference filter and collimated the beam in the far field ($\approx$ 5 m). We then aligned the cavity by centering the beam on the holes for the first and second lenses using the collimator adjustment screws and a half-inch alignment target (ThorLabs SM05A7). A well-centered beam should, in principle, minimize any aberrations that may arise as a consequence of the lenses through which the beam is focused. We would particularly like to avoid this phenomenon after the first lens, since a smearing of the focus at the position of the output coupler will reduce the optical feedback into the laser diode.

The next step was to insert the first lens and the output coupler. The mounting of the lens consisted of placing the lens into the circular lens retainer with the curved side of the lens facing the diode. The lens retainer, in turn, was surrounded by a viton fixing ring. This ring was lightly covered in vacuum grease for ease of adjustment of the lens. The output coupler was placed in the Newport mount and screwed into the inner housing. To ensure optimal feedback, the surface of the coupler should coincide exactly with the

focus of the lens. To this end, we placed a 1" beam splitter plate (R:T = 90:10) into the cavity at a 45° angle, thereby reflecting part of the light out of the cavity. This beam was then collimated in the far field by rotating the lens.

For the next step, the current was reduced to just below the natural lasing threshold of the diode. We then proceeded to tune the output coupler's pitch and yaw using the fine adjustment screws on the Newport mount, such that the reflected beam was incident on the center of the diode. To determine whether the reflected light was indeed centered, we used a punctured piece of paper which was held into the external cavity at a position close to the end of the collimator. After a couple of minutes of adjusting the back-reflection to align with the center of the puncture, this procedure resulted in lasing of the diode. At this point we optimized the lasing threshold of our laser for the first time using the procedure described in Subsection. 5.2.2.

We then inserted the second collimating lens into the laser and placed the wedged window (WW11050-A) into the tilted insert on the outer housing. The tilt of the window is intended to prevent back-reflection into the cavity, whilst the wedge form of the window reduces etaloning effects in both the transmitted and reflected components of the laser light. The window was fixed by clamping the rectangular retaining frame onto the outer housing using four M4×10 screws. The window was made airtight by inserting a silicon band into the provided inset in the retaining frame.

As a final step, we placed the interference filter (473 nm bandpass filter from Iridian) into the remaining Newport mount and fixed this mount with a dowel pin to the floor of the laser cavity between the laser diode and the first lens. The dowel pin provides the rotational degree of freedom required for wavelength adjustment with the filter. To restore lasing, some crude initial adjustment of the IF angle is usually required at this point. We then proceeded to re-optimize our lasing threshold as before.

5.2 Characterizing the Laser

5.2.1 Beam Shaping

To maximize the usable output power and reduce aberrations as the laser light passes through any optical elements, the highly elliptical mode emitted by the laser diode needs to be shaped into a zeroth order Hermite-Gaussian mode. For this purpose we decided to use a cylindrical telescope, rather than an anamorphic prism pair or spatial filtering, since the cylindrical lenses can be aligned to correct for any astigmatism present in the beam. Furthermore, the cylindrical telescope transmits a larger share of the beam power than the previously mentioned beam shaping methods [79]. For our telescope we chose cylindrical lenses with a focal length of $f_1 = 50$ mm and $f_2 = 20$ mm matching the initial

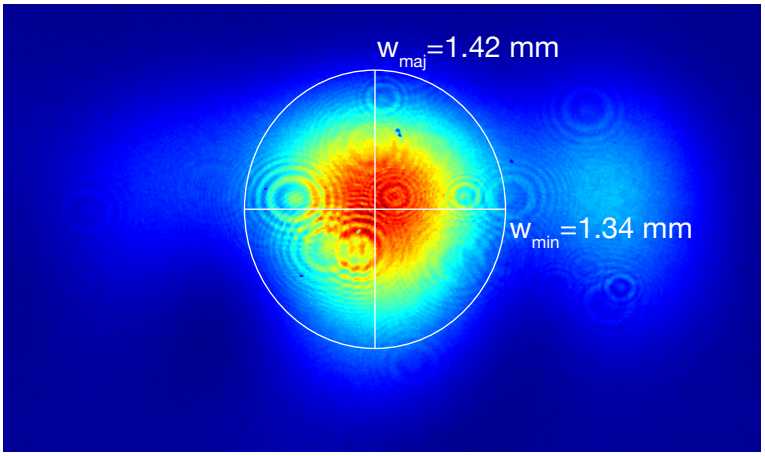

Figure 5.4 The shape of our laser beam as measured by a CINOGY CinCam CMOS 1201 Nano beam profiler ≈ 3 m from the front face of the laser housing. The 2nd moments fit shows a 1:0.94 ratio of major to minor axis.

aspect ratio of our elliptical laser beam. These were then mounted to each other with cage rods at a distance corresponding to $f = f_1 + f_2$ and with their flat sides facing each other. The beam was observed on a beam profiler (CINOGY - CinCam CMOS 1201 Nano) at a distance of approximately 3 m from the front face of the laser housing. The relative position of the lenses was carefully adjusted to obtain an optimal aspect ratio of 1:0.94 as measured by the 2nd moments fit provided by the beam profiler software (see Fig. 5.4).

5.2.2 Threshold Current

As explained in the previous chapter, the threshold current describes the current at which the gain of our laser diode is equal to the losses of the resonator. According to ([70])

$$P = \eta(I - I_{th})\frac{1.24}{\lambda} \tag{5.1}$$

a lower threshold current I_{th} guarantees a higher output power at a given operating current I, thereby increasing the efficiency of the laser. Furthermore, the higher circulating intracavity power ensures a greater mode stability for a given current. We therefore want to lower I_{th} as far as possible.

For our optimization procedure, we fed a 100 Hz sawtooth wave with an amplitude of 1 V (corresponding to 10 mA on the laser diode) into the modulation input of the current controller using a Stanford Research Systems function generator (SRS DS345). This signal was also observed on an oscilloscope (Keysight - InfiniiVision MSOX2004A) and

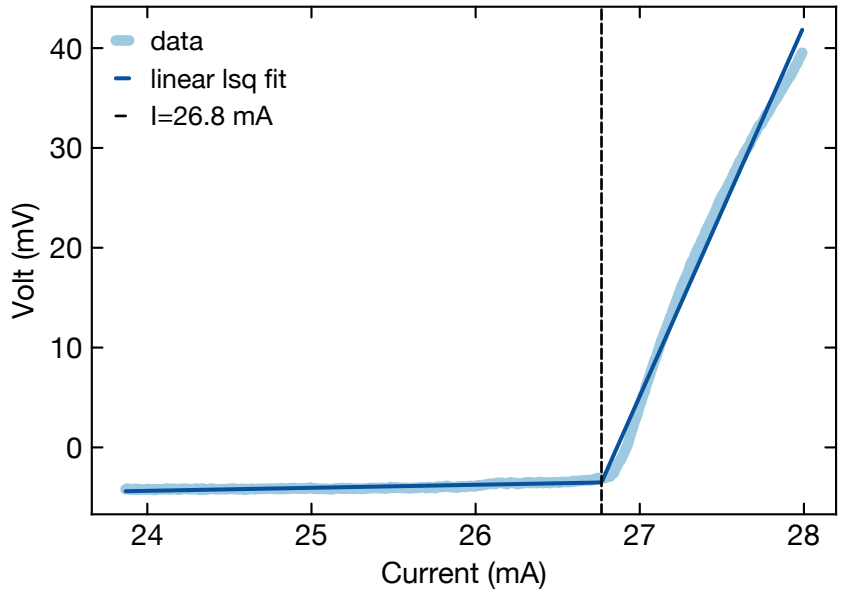

Figure 5.5 Oscilloscope data (light-blue) for the optimal lasing threshold of our linear ECDL. A two-line fit (dark-blue) leads to a value for the lasing threshold of 26.8 mA at the intersection point (indicated by the dashes black line).

provided the trigger signal for our optimization procedure. We then connected the DC output of the photodetector to the oscilloscope. The observed signal is defined by a 'kink' at the position of the lasing threshold, as illustrated in Fig. 5.5.

To optimize the threshold current, we sequentially tuned the pitch/yaw of the output coupler and the position of the first lens while observing the location of the 'kink'. The aim was to push this feature to the lowest possible current. We found it necessary to decrease the laser diode current after each incremental adjustment of the output coupler or lens to keep the 'kink' roughly in the center of the oscilloscope display. The optimum was reached when a turning point occured, that is to say, when any adjustment of the output coupler or lens resulted in higher lasing thresholds. Using this procedure, we achieved a threshold current of 26.8 mA. Since our protection board draws a current of 9 mA, the actual lasing threshold lies at 17.8 mA.

5.2.3 Interference Filter

Our interference filter was provided by Iridian (473 nm bandpass filter) and consists of a multiple layers of dielectric coatings. Depending on the thickness, refractive indices and the order in which these dielectric coatings are layered, it is possible to produce a filter with very specific transmission properties. As the angle of the incident light is changed,

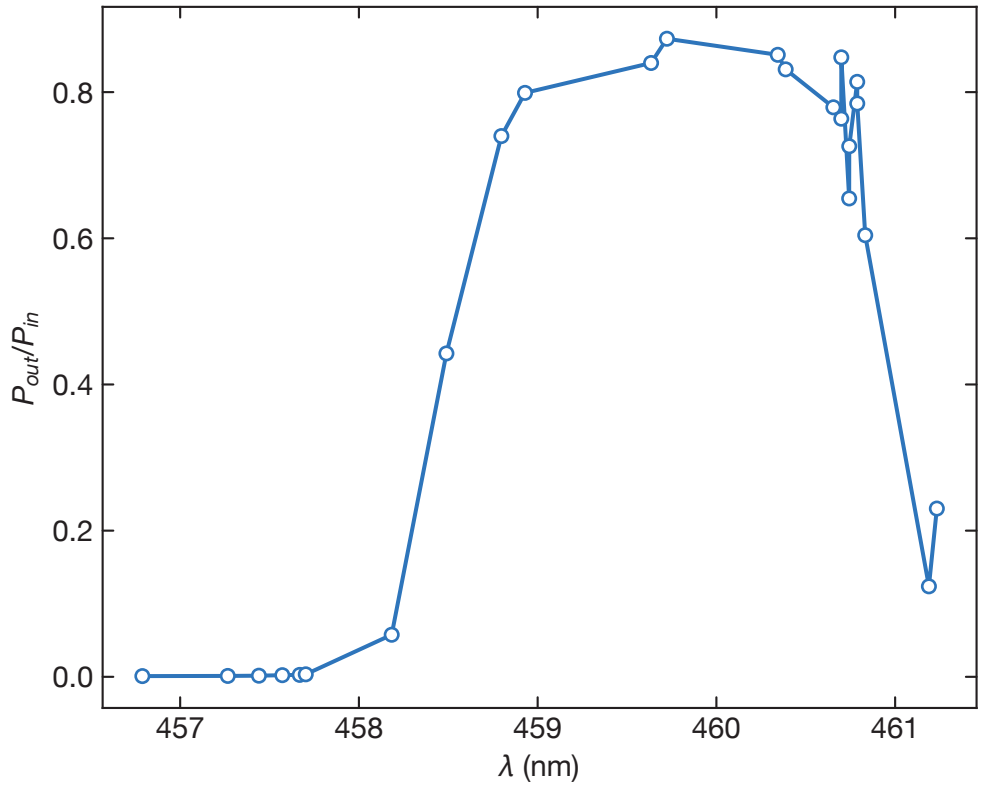

Figure 5.6 The transmission spectrum of our IF with a FWHM of ≈ 3 nm

the wavelength of the transmitted light through the filter changes according to [75]

$$\lambda = \lambda_0 \sqrt{1 - \frac{\sin^2\theta}{n_{eff}^2}}, \tag{5.2}$$

where λ_0 is the transmitted wavelength at normal incidence and n_{eff} the refractive index of the filter. In contrast to a grating-based laser, where the Bragg condition $\lambda = 2d\sin\theta$ determines the wavelength, Eq. (5.2) leads to a much smaller wavelength change as a function of the angle. In principle, therefore, the filter design is more robust with respect to angular misalignment. The width of the filter transmission spectrum was determined by measuring the transmission through our filter with a powermeter while scanning the wavelength using the piezo and observing the wavelength on our wavemeter. The resulting spectrum (Fig. 5.6) has a FWHM of ≈ 3 nm.

5.2.4 Linewidth

For the purposes of absorption spectroscopy and the 2D MOT, the linewidth of our laser needs to lie below the $^1S_0 \rightarrow ^1P_1$ transition linewidth of 30.5 MHz. We measured the linewidth of our laser in two separate ways. The first was a heterodyne beat measurement with our 461 nm Toptica DL Pro. The second measurement was performed with the use of an EagleEye OSA. The linewidth obtained from both of these measurements is narrow enough to allow for our planned absorption spectroscopy. However, a large discrepancy between the beat and the EagleEye was observed. The details of these measurements is discussed in the following.

Heterodyne Beat

Broadly speaking, a heterodyne beat measurement consists in interfering the light of two lasers with similar frequency on a photodetector. The interference of the two lasers gives rise to a beat signal, from which it is possible to infer an upper bound on the linewidth of either one of the lasers.

More concretely, we can consider a simplified model where the two interfering laser beams are assumed to be plane waves

$$\begin{aligned} \mathbf{E}_1(\mathbf{r},t) &= E_0 e^{\mathrm{i}(\mathbf{k}\cdot\mathbf{r}-\omega_1 t+\phi_1)}\mathbf{e}_1 \\ \mathbf{E}_2(\mathbf{r},t) &= E_0 e^{\mathrm{i}(\mathbf{k}\cdot\mathbf{r}-\omega_2 t+\phi_2)}\mathbf{e}_2 \end{aligned} \tag{5.3}$$

with angular frequencies $\omega_{1/2}$, polarization vectors $\mathbf{e}_{1/2}$, phases $\phi_{1/2}$ and a constant amplitude E_0. The intensity profile resulting from the interference of two such waves takes the form:

$$I(\mathbf{r},t) \propto |\mathbf{E}_1(\mathbf{r},t)+\mathbf{E}_2(\mathbf{r},t)|^2 = 2\left(E_0^2 + E_0^2 \mathrm{cos}[(\omega_1-\omega_2)t-\phi_1-\phi_2]\right). \tag{5.4}$$

Let us recall from Chapter 4 that, in an ideal case, each individual laser beam exhibits a Lorentzian lineshape. Furthermore, the convolution theorem tells us that a multiplication in the time domain corresponds to a convolution in the frequency domain. Consequently, we expect our intensity, which is nothing more than the multiplication of individual **E**-fields, to correspond to a convolution of Lorentzians in frequency space, i.e. another Lorentzian. However, since our laser is not an ideal system, some acoustic noise on our beat signal is unavoidable. This introduces a Gaussian contribution to our lineshape and therefore alters our signal to that of a Voigt profile.

Our measurement was carried out using the setup sketched in Fig. 5.7. Light from our linear ECDL was superimposed with light from a Toptica DL pro, locked to the $^1S_0 \rightarrow ^1P_1$ transition via modulation transfer spectroscopy, using an NPBS and sent onto a home-built photodetector with a bandwidth of 250 MHz and a gain of 1 kΩ. The DC port

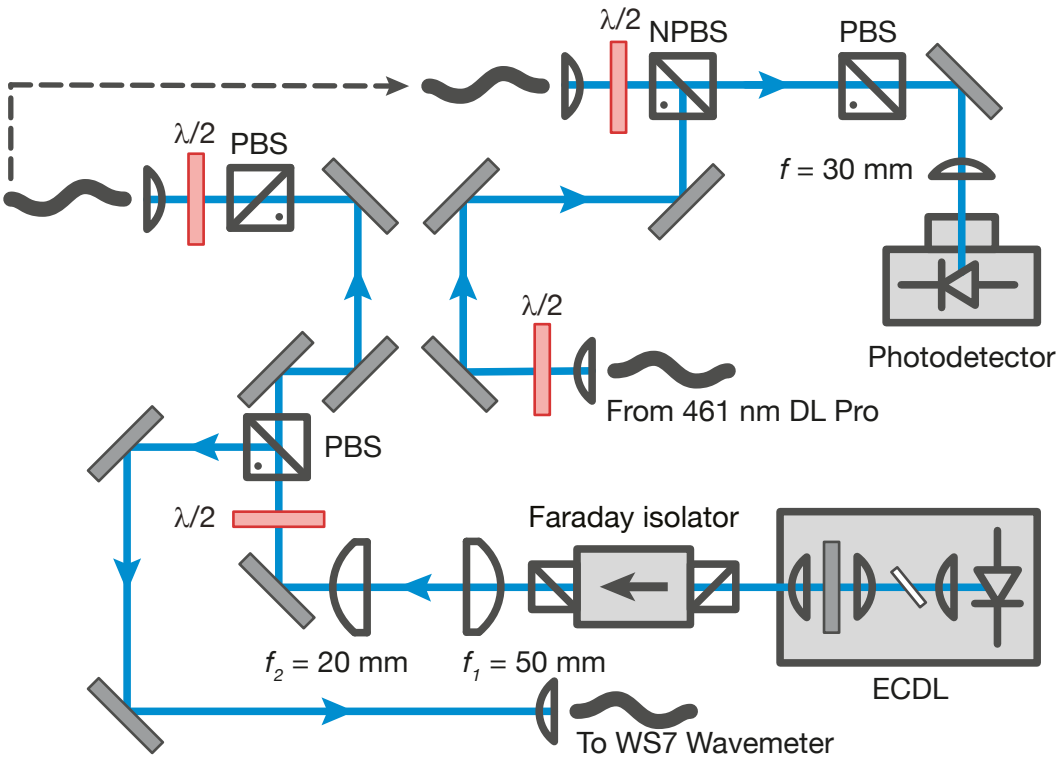

Figure 5.7 A schematic of the setup used to measure the beat signal between our linear ECDL and our locked 461 nm Toptica DL Pro.

of the photodetector was connected to an oscilloscope and the AC port to a spectrum analyzer (Anritsu MS2721B). Care was taken to match the intensity and polarization of both beams and to ensure mode overlap along the entirety of the optical path. This was done to increase the signal contrast and create uniform interference conditions across the entire photodiode. To further increase the signal strength, the superimposed beam was focused onto the facet of the photodiode using a f=35 mm plano-convex lens (Thorlabs LA1027-A) and the alignment of the beam varied until the DC signal on the oscilloscope was at its maximum.

Having thus optimized our alignment, we observed the signal plotted in Fig. 5.8. As expected, we observe a Voigt profile with an associated FWHM of $\approx$ 3.6 MHz for a RBW of 300 kHz. Using the our 689 nm Toptica laser's free-running linewidth as a ballpark figure for an order-of-magnitude estimate of our own linewidth, we would expect a beat on the order of several hundred kHz rather than 3.6 MHz. Two possible factors that could contribute to a broadening of the linewidth are the low-bandwidth lock of the blue Toptica to a spectroscopy cell as well as the particular material properties of blue laser diodes as discussed in the previous chapter. However, even this relatively broad upper bound on our linewidth is roughly a factor of ten less than than the atomic transition we will address with our absorption spectroscopy.

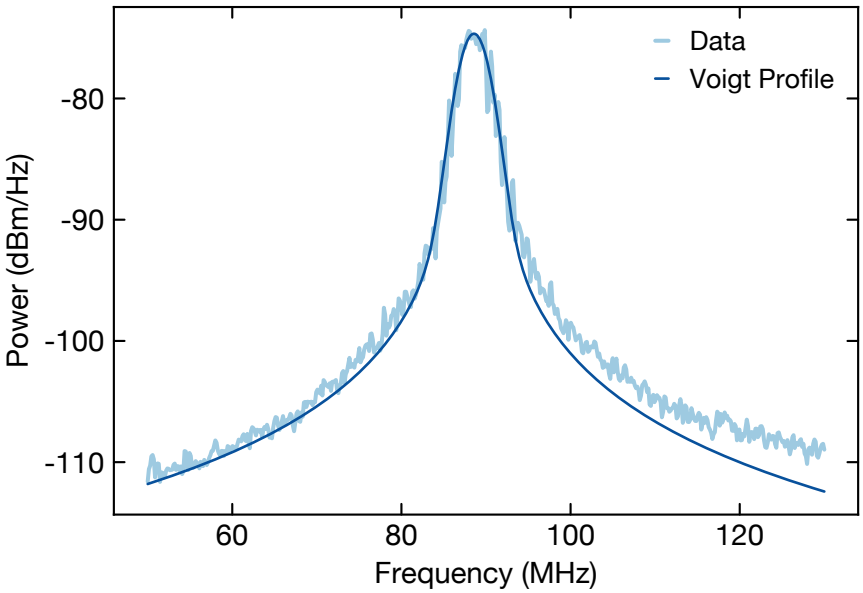

Figure 5.8 The recorded beat signal between our linear ECDL and our locked 461 nm Toptica DL Pro. The fitted Voigt profile gives a 3 dB FWHM of $\approx$ 3.6 MHz with an RBW of 300 kHz

EagleEye OSA

Our second linewidth measurement was performed with the use of a Fabry-Pérot interferometer (FPI) in the form of an EagleEye OSA from Sirah. An FPI is type of optical resonator formed by two partially reflective mirrors. As such, it supports a discrete spectrum of cavity resonances (see Chapter 4 for details). In the EagleEye OSA, the laser of unknown linewidth is coupled into the cavity and the aforementioned cavity resonances are scanned in frequency space by a piezo actuator until a transmission maximum is found. The EagleEye then uses a PID loop to lock the laser transmission to the rising/-falling edge of the corresponding cavity resonance. The lock is turned off after some hold time and the resulting intensity fluctuations due to the laser jitter are observed. From these fluctuations it is possible to infer the linewidth of the laser [80]. In this manner, the EagleEye achieves a linewidth resolution of 20 kHz, despite its comparatively broad cavity resonances of $\approx$ 5 MHz [81].

The results of the EagleEye measurement are recorded in a histogram (Fig. 5.9). A Gaussian fit of our data yields a mean linewidth of 0.42(6)MHz with an error given by the standard deviation. However, it is evident from Fig. 5.9 that the Gaussian fit does not seem to approximate the shape of the underlying distribution very well. This may simply be due to the limited sample size (298 data points were recorded by the EagleEye). Nonetheless, we have included a kernel density approximation [82] for completeness, which seems to hint at the mode of our data as a more accurate value for the linewidth of our laser. The modal linewidth is 0.39(6)MHz.

In either case, we note a large discrepancy between the linewidth as recorded by the EagleEye and that of our beat measurement. One possible explanation for this discrepancy is that the frequency jitter of our linear ECDL was faster than the bandwidth of the EagleEye.

5.2.5 Mode-Hop-Free Tuning Range

As we outlined in the introduction to this chapter, we need to be able to scan our laser continuously over a large range of detunings ($>$ 5 MHz) to measure the entire absorption spectrum of our atomic beam. This is achieved by varying the external cavity length with our piezo. In practice, however, the laser will experience mode-hops as the shift in cavity resonance causes another nearby mode to become dominant. To circumvent this problem, a current is fed forward to the laser diode which causes the its gain spectrum to shift in a common mode fashion with the cavity resonance spectrum. The maximal mode-hop free tuning range is achieved when the ratio of current feedforward to piezo scan range is at an optimum.

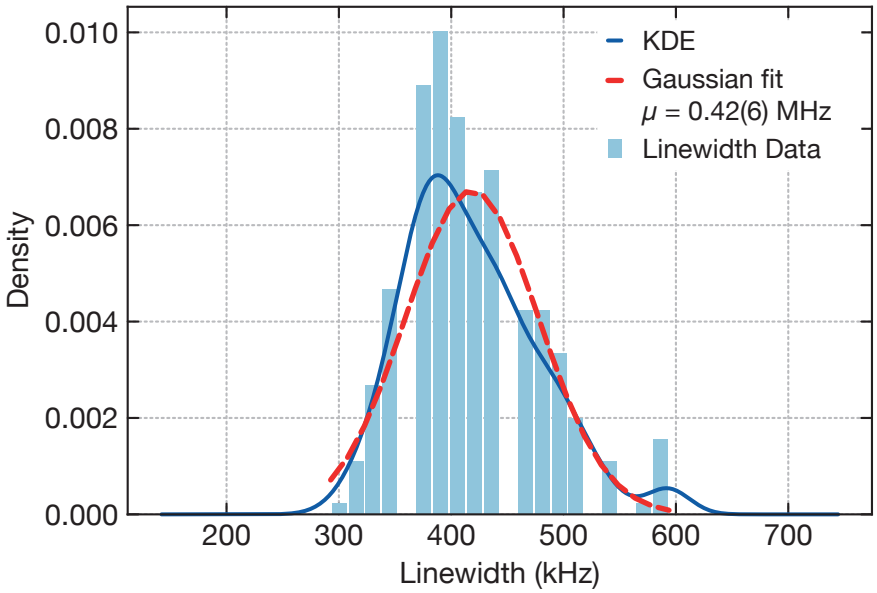

Figure 5.9 A histogram of the linewidth data recorded by the EagleEye OSA. A Gaussian fit of our data produces a mean linewidth of 0.42(6) MHz with an error of 60 kHz given by the standard deviation. A kernel density estimation (KDE) suggests a modal linewidth of 0.38(6) MHz.

To find this optimum ratio, we used the same setup as for our beat measurement (Fig. 5.7) and followed the relevant instructions in the Sys DC 110 manual [83]. We initially encountered some difficulties during the tuning procedure which limited our mode-hop free range to $\approx$ 1.2 GHz. This problem was resolved by inverting the feedforward signal before sending it to the laser diode (for further details see Appendix. B). With this modification, we measured a mean MHF tuning range of 6.8(1) GHz (Fig. 5.10). The wiggles in the the scan apparent in panel (b) of Fig. 5.10 are likely caused by contributions from other modes, but do not cause a mode-hop when observed on an oscilloscope. After the optimization of our mode-hop free range we measured the usable output power of our laser (after the cylindrical telescope and an the isolator) at the desired wavelength of 461.86198 nm. This gave a value of 42(1) mW measured using a PM100D powermeter.

5.2.6 Stability

The large, hermetically sealed outer housing of our ECDL is intended to increase its frequency stability by reducing the effect of both mechanical vibrations and fluctuations in ambient air pressure. Furthermore, our laser diode and external cavity are actively temperature stabilized to minimize the effects of temperature drifts on our laser frequency. To test the stability of our laser, we recorded its frequency over a period of five hours

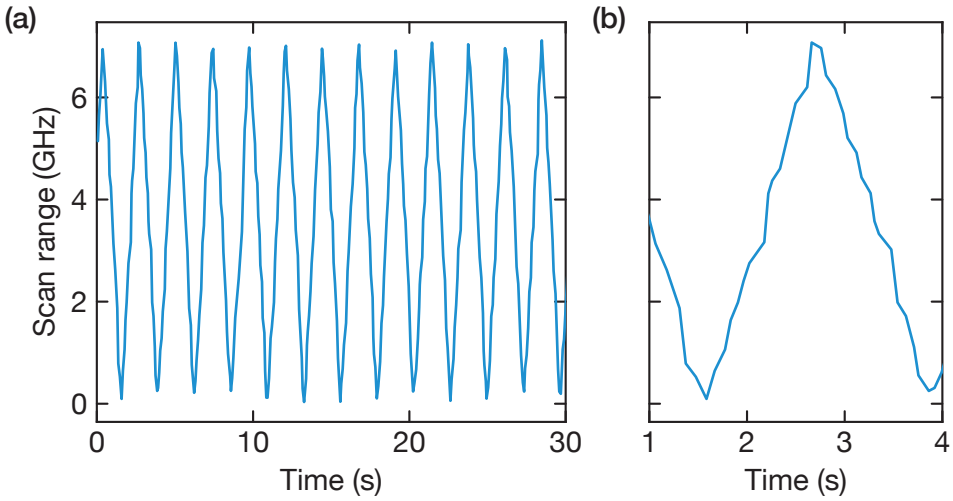

Figure 5.10 A plot of the frequency scan of our linear ECDL over a mean MHF tuning range of 6.8(1) GHz, as recorded by the wavemeter.

using a WS7 high-finesse wavemeter. For comparison, we performed the same measurement with our 461 nm Toptica DL Pro. The results are recorded in Fig. 5.11.

The total drift range for our linear ECDL over five hours is 330(4) MHz compared to 179(4) MHz from the Toptica with an error provided by limited resolution of our wavemeter. Additionally, we observe greater amplitude fluctuations on short timescales for our linear ECDL. It is worth noting that the Toptica laser was very well isolated from its environment, whereas our laser was positioned next to an active turbo pump and had no separate enclosure for its breadboard. To quantify the laser instability and gain some precise insight into the possible noise sources on our laser we calculated both the overlapping and modified Allan deviations for Fig. 5.11. The results are recorded in Fig. 5.12 for a sampling rate of 5 Hz.

The Allan deviation, $\sigma_y(\tau)$, is a measure for the instability of an oscillator. For an absolutely stable oscillator, the frequency, ν, is fixed at some nominal value, ν_n. Instabilities in the oscillator lead to variations of the frequency from its nominal value and different noise sources invariably introduce variations from the nominal value on different timescales. To quantify these deviations we introduce the fractional frequency, defined as:

$$\overline{y_n} = \frac{\nu - \nu_n}{\nu_n} \tag{5.5}$$

The Allan deviation allows us to distinguish the frequency instability due to different noise sources by calculating the deviation in the variance of this fractional frequency for

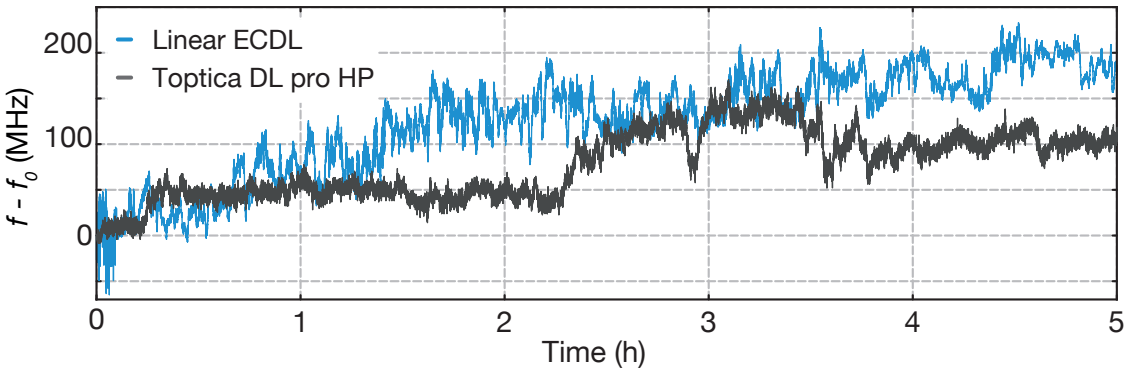

Figure 5.11 Stability measurement of our linear ECDL and our 461 nm Toptica DL Pro over a period of 5 h. The linear ECDL exhibits a larger drift range (330.39 MHz vs 179.26 MHz) and greater amplitude fluctuations at short timescales.

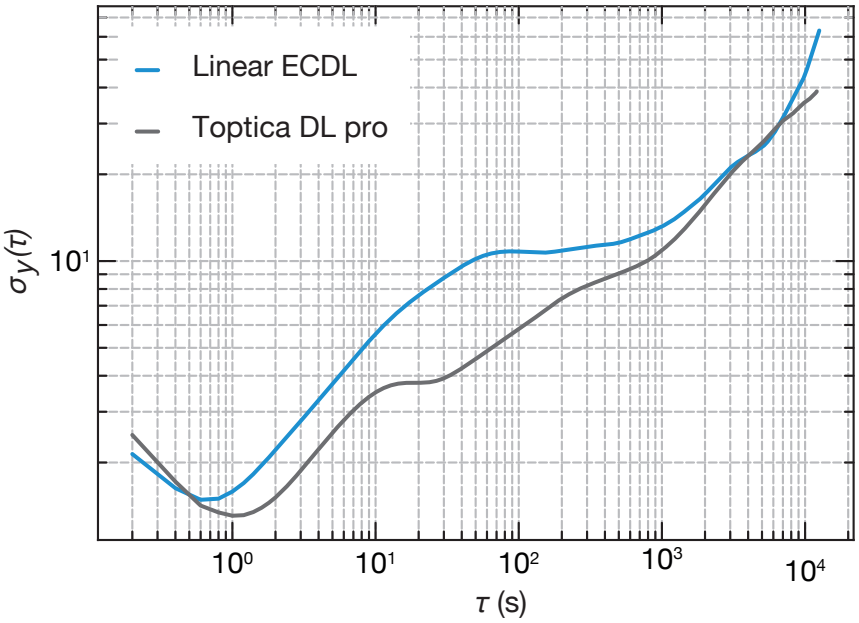

Figure 5.12 A plot of the overlapping Allan deviation for the stability data of Fig. 5.11. Our linear ECDL exhibits a comparable stability to the Toptica DL Pro over a 1 s sampling time.

different sampling times, τ [84]

$$\sigma_y(\tau) = \sqrt{\frac{1}{2}\langle(\overline{y}_{n+1} - \overline{y}_n)^2\rangle} \tag{5.6}$$

The overlapping Allan deviation plotted for our laser in Fig. 5.12 represents an improvement over the standard Allan deviation in terms of its confidence interval. It is calculated by forming all possible overlapping samples at each time τ [85]. Fig. 5.12 reveals a comparable stability between our linear ECDL and the Toptica DL Pro over a 1 s sampling time with a slightly lower noise floor for the Toptica laser. On longer timescales we observe a positive slope for both lasers, indicative of low-frequency noise associated with longer term drifts such as variations in temperature.

In this chapter we have reported on the construction of a linear ECDL operating at 461 nm. Our laser is characterized by a maximal free-running linewidth of 3.6 MHz (RBW = 300 kHz) and a mod-hop free tuning range of 6.8(1) GHz. It features a usable output power of 41.7 mW with a stability comparable to that of a 461 nm Toptica DL Pro over a sampling time of 1 s. These parameters are sufficient to conduct absorption spectroscopy on our atomic beam. To improve these parameters, several issues should be addressed. The placement of the protection board to the outside of the housing would enable the evacuation of the laser, improving its stability by reducing possible air-pressure fluctuations. Furthermore, the backplate of the outer housing needs to be updated to include current modulation feedthroughs and one of the female sub-D pins should be exchanged for its male counterpart. On the topic of optics, we could try to improve the feedback into the diode by using properly coated mirrors instead of Thorlabs beam splitter plates as output couplers. However, given the difficulties associated with blue diodes (as explained in Chapter 4), the aforementioned laser parameters represent a promising starting point for the next iteration of home-built blue lasers for our lab.

Chapter 6

Complete Setup and Results

With our home-built ECDL from the previous chapter and the oven from Ch. 3 we are now in possession of the two main ingredients necessary to test our oven design and the associated theoretical predictions from Ch. 2. Naturally, we require a vacuum chamber within which to perform our measurements. The design of this vacuum chamber is explained in Section 6.1 of this chapter. Following this section, we describe several problems that we faced during our measurements with the oven. In particular, we encountered clogging of our nozzles due to necessary modifications on our heat shields (see Subsections 6.3.2 and 6.3.3 for details). This prevented us from performing our planned efficiency measurements. However, we were able to develop our understanding of the clogging process, which has proven to be a widespread problem for such microcapillary array ovens.

6.1 Test Setup

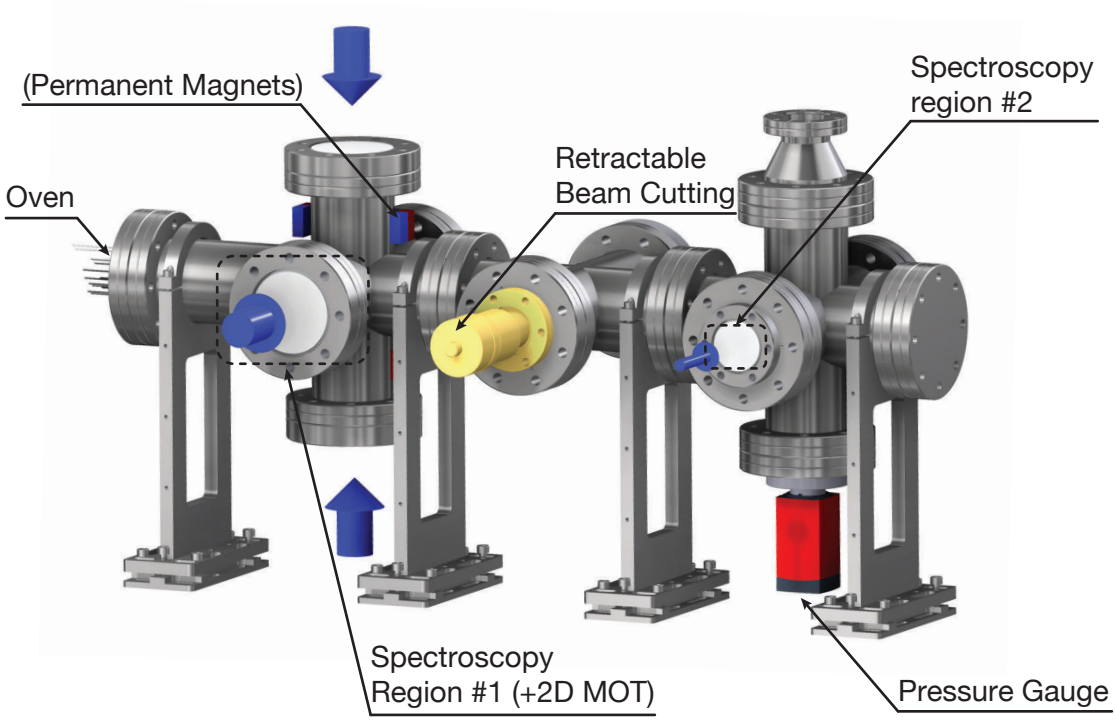

Figure 6.1 A render of the vacuum chamber used to test the atomic beam parameters. Spectroscopy is performed regione #1 and #2, which are separated by a razor blade. This allows us to measure the efficiency of our oven.

In Ch. 2 we had discussed the flow-rate and usable fraction of atoms as quantities that would allow us to determine the efficacy of our oven. Our vacuum test chamber was designed to allow for the measurement of both of these quantities. In spectroscopy region #1 we have the ability to measure the absorption profile, and by extension the total flow-rate, directly after the oven. After this region, a retractable razor blade cuts the atomic beam at various points in its profile, effectively simulating an aperture akin to the differential pumping tubes used in our current vacuum system. After this razor blade, the atoms are again probed with our laser in spectroscopy region #2. By comparing the total flow-rate before and after the razor blade, we can obtain a measure of the efficiency of our oven.

6.1.1 Construction Specifics

In addition to allowing for our spectroscopy measurements, the four CF63 viewports in spectroscopy region #1 provide enough optical access and a large enough viewport size

(interaction area) for a 2D MOT (see Ch. 1). All our viewports were manufactured by Novotek using Corning HPFS 7980 fused silica with a flatness of $\frac{\lambda}{4}$ at 632 nm and polished to a scratch-dig of 20/10. We additionally specified a .5° tilt to prevent reflection. The viewports were then anti-reflection coated for 461 nm and 689 nm by LaserOptik using electron beam evaporation (EBE) to minimize the loss of laser power and reflections at the viewports. Due to the shadow effect from the edge of the viewports, the effective coated area of the CF40 and CF63 viewports was $\varnothing = 29$ mm and $\varnothing = 57$ mm respectively. The six-way cross piece was manufactured from EN 1.4301 steel. To prevent any modification of the magnetic field by the magnets of a 2D MOT, a less magnetically permeable steel, such as EN 1.4401 (AISI 316), would have been preferable. However, the permeability of our cross-piece was measured using a magnetometer (Dr. Foerster GmbH & Co. KG: Magnetoscop 1.070) and found to vary between 1.001 and 1.007. Additionally, the cross-piece has been specially modified to place the oven far enough away from the viewports such that no line-of-sight existed between the capillaries and the viewports. This was intended to prevent coating of the viewports with strontium. In fact, just such a coating of the viewports was observed during our measurements. An explanation for this effect will be discussed in Subsection 6.3.2.

The retractable razor consisted of a bellows-sealed precision linear feedthrough (Pfeiffer: PF 631 012-T) and a razor blade mounted to the front of this feedthrough using a custom mount. This feedthrough was chosen due to its ability to provide strictly linear translation i.e. no feedthrough was rigid in the lateral dimension.
The pressure in our chamber was monitored using a Pfeiffer cold-cathode pressure gauge (Pfeiffer: PTT02350011) mounted at the rear end of the chamber. The entire test chamber was mounted on four pedestals ensuring a beam height of 250 mm, corresponding to beam height used in our main vacuum system. We decided to place the entire construction on a breadboard, such that we could move the whole chamber if necessary.

To be able to measure the absorption directly after the oven as well as after the razor blade at the back of the chamber, we used a flip mount to alternately send our laser light to either spectroscopy region. The power of the light incident on the atoms was measured to be ≈ 11 μW giving an intensity of ≈ 0.4 mW/cm^2 for a $\frac{1}{e^2}$ beam waist of 1 mm at the focus of the beam. After passing through the chamber, the laser light from either spectroscopy region was sent onto a home-made photodetector (bandwidth = 17 MHz, DC gain = 10V/mW) using another flip mount (to maximize the signal-to-noise ratio we refrained from using an NPBS at this point) and the signal observed on an oscilloscope (Keysight InfiniiVision MSOX2004A).

6.2 Measurement Procedure

According to the rationale set out at the beginning of the last section, we decided to measure the absorption spectrum before and after the razor blade for a range of temperatures. At each temperature we also measured the absorption spectrum behind the razor

blade for progressively increasing razor blade protrusions into our atomic beam. At the beginning of each measurement sequence, our linear ECDL was tuned to the $^1S_0 \rightarrow ^1P_1$ transition frequency of 650.503835 THz by varying its current and temperature using our wavemeter. Having established stable single-mode operation at the required frequency, the scan range of the laser was maximized by alternately increasing the scan amplitude and varying the current and temperature. For this procedure, we simultaneously observed the laser light on the oscilloscope and on the wavemeter. We also monitored the scan voltage of our ECDL on the oscilloscope and triggered on the trigger signal provided by the scan control. The scan frequency was set low enough to observe a clear mode-hop free scan signal on both the oscilloscope and the long-term graph of our wavemeter. We saved this scan graph at the beginning of every measurement sequence to use later as the frequency range of our absorption spectrum. We then proceeded to increase the power on the heating circuits and observed the temperature of the crucible and nozzle using two hand-held digital thermometers (Omega: HH801A). In an attempt to prevent clogging, we heated the nozzle circuit first and tried to establish the maximum possible temperature gradient between the nozzle and the crucible. Only then did we begin to heat up the crucible and nozzle simultaneously. Since we did not have a PID loop for the power provided to our heating circuits, the necessary power to reach any given temperature was controlled manually. This increased the duration of the measurement process, since we had to wait for the temperature to equilibrate before judging whether or not to increase or decrease the power to reach a desired setpoint.

6.3 Problems Encountered

During the measurement process described above, we encountered numerous difficulties and problems which we will describe in the following. We will also provide potential solutions to each of these issues.

6.3.1 Reloading Process

The reloading process involved preparing a glovebag with all the necessary equipment used in the nozzle exchange and strontium relaoding process. The glove bag and the chamber were then simultaneously flooded with argon. This involved attaching the argon bottle to an appropriate Timmer t-piece with one end running to our pumping station and the other directly to our glove bag. Prior to opening the argon bottle, we valved off our chamber and turned off the turbo pump. Then we let the membrane roughing pump evacuate the bellows attaching our pumping station to the chamber as well as the tubing running from the argon bottle to said pumping chamber and to the glove bag. We then valved off the membrane pump, opened the valve to the vacuum chamber and opened the regulator on the argon bottle to let the argon flow into the chamber and the glove bag. Once the glove bag had been filled with argon we opened it and pushed out the

argon along with any remaining air in the bag. We then temporarily sealed this bag and waited for it to refill with argon. Once a sufficient amount of argon had entered the bag (indicated by the swelling of the bag) we detached our oven from the vacuum chamber, opened the glove bag, quickly placed the oven inside and resealed the bag.

Although our oven was already designed to minimize the necessary reloading effort (see Chapter 3 for details), we nevertheless encountered difficulties when exchanging our nozzles and/or loading our oven with strontium in a glove bag. The first and most prominent problem was posed by the screws fixing our heat shields to the baseplate and the nuts on the steel rods holding the fixing disk in place. These proved to be very difficult to handle in the glove bag and made the reloading process very slow. A second problem was posed by the fusing of the inner heat shield to the baseplate. To take off this heat shield we had to twist and pull the shield with one hand while holding the steel rods with the other.
A possible solution to both problems would be to develop a "clip-on" mechanism for both heat shields. This could be achieved by having four screws sticking out of the baseplate with a four matching, L-shaped openings at the base of both heat shields which would allow us to lock them in place by simply turning the heat shields slightly. The same mechanism could also be employed on the fixing disk and is illustrated schematically in Fig. 6.2(a). Finally, the positioning of the nozzle thermocouple meant that every time we wanted to exchange the nozzle we had to move the thermocouple out of the way and then move it back after having inserted the new nozzle. This meant that the thermocouple did not measure the temperature at exactly the same temperature every time. A solution to this problem is made difficult by the lack of space around the nozzle. However, we could exploit the space between the heating wires and drill a hole in the steel retainer and crucible walls through which the thermocouple could contact the side of the nozzle. This is illustrated in Fig. 6.2(b), where the position of the holes to be drilled are marked with red crosses.

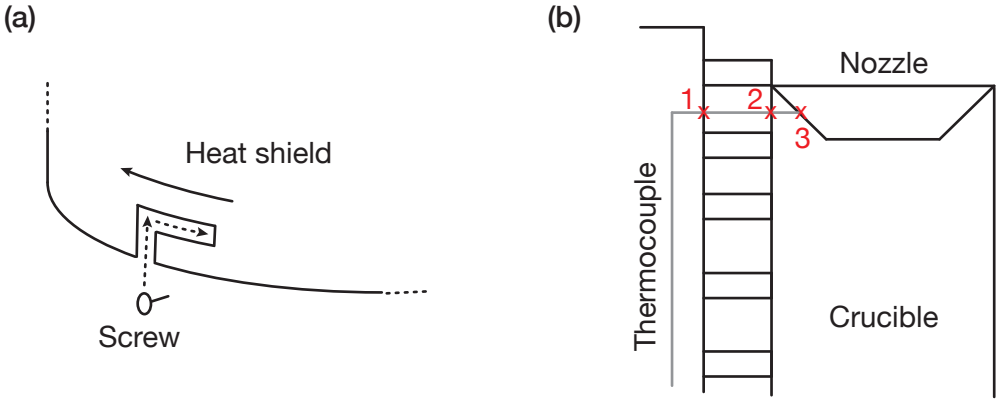

Figure 6.2 Two possible solutions for the an easier reloading process. Panel (a) illustrates a simple "clip-on" mechanism for the heat shields while panel (b) shows an alternative thermocouple placement to avoid having to move the thermocouple during the reloading process.

6.3.2 Viewport Coating

Our first measurement was conducted with a capillary aspect ratio of β=0.027 (corresponding to a length of 7.5 mm and a diameter of 200 μm). We observed a much narrower spectrum in both absorption regions than expected from our theoretical model (see Fig. 6.3). The data was, however, consistent with an atomic beam being cut off by our fixing disk. However, while the absorption profile was very narrow, we had no way to determine the area of the atomic beam that was cut off by the heat shield and consequently no way of measuring the efficiency of our oven. In addition, we noticed coating of the viewports beginning at a crucible temperature of $\approx$ 700 °C. This coating was characterized by a gradual increase in the reflectiveness of our viewports until a mirror-like surface was visible [Fig. 6.4(a)] on the surface of the viewport. Since there was no line-of-sight between the capillaries and the viewports we speculated that one or both of he heat shields became hot enough to cause scattering of the atoms from the edge of its aperture at steep enough angles to cause a coating of the viewports. This theory was lent extra credence by the large amount of strontium oxide observed around the aperture of the second heat shield once the heat shields had been removed from the vacuum Fig. 6.4(b) and (c).

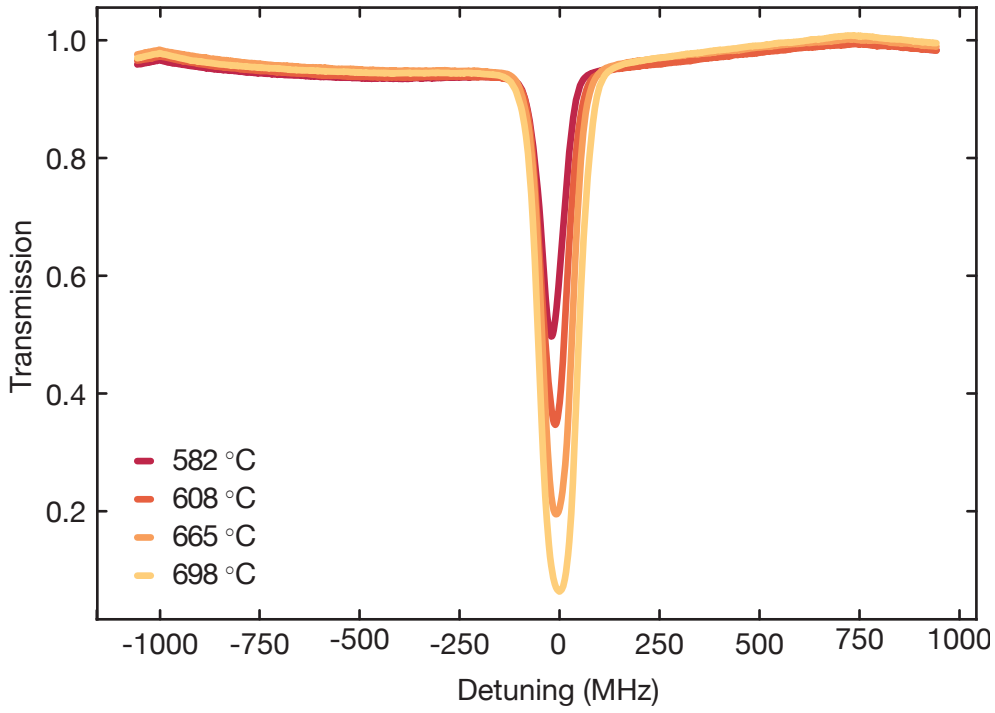

Figure 6.3 The first transmission spectrum observed during our measurements in spectroscopy region #2. The spectrum is much narrower than what we would expect from the collisional model of Chapter 2. This is due to the heat shield apertures cutting the beam and artificially narrowing it. Coating of the viewports began at $\approx$ 700 °C.

As a result of the beam clipping and the coating of the viewports we decided to replace the heat shields, fixing disk and ceramic nozzle insulation by the same parts with their respective aperture sizes maximized. In the case of the heat shields this meant the complete removal of the front of the heat shields, resulting in two cylindrical heat shields. In addition, we moved the entire oven back from the viewports by 65 mm with the aid of a piece of CF63 vacuum tubing that had been cut to size. The distance was chosen to eliminate any line-of-sight between the edge of the heat shields and our viewports. With respect to the coating, we heated the viewports to 160 °C for two weeks using heating tapes and specially made steel disks that covered the viewports to ensure a uniform heat distribution over the surface of the viewport. This heating worked well and removed the majority of strontium from the viewports to the extent that any residual coating was no longer visible on the surfaces.

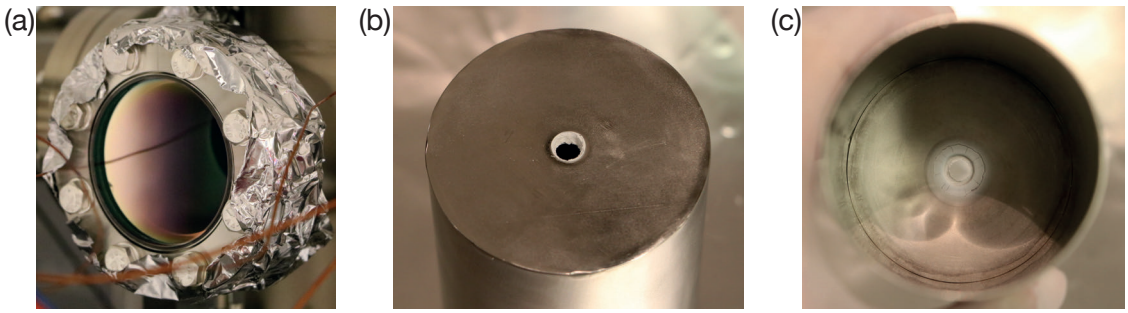

Figure 6.4 (a) The appearance of one of our CF63 viewports when partially coated by strontium. The coating is visible on the left-hand side of the viewport as a silvery reflective surface. (b) and (c) show the outermost heat shield after having been removed from the oven. The heat shields cut the atomic beam as indicated by the visible strontium on the inside of the heat shield. Moreover, the coating of the viewports was likely caused by atoms scattering off the inside of the hot heat shields at steep enough angles to reach the viewports.

6.3.3 Clogging

Upon exchanging our nozzles, we observed a large amount of clogging on the capillaries, as shown in Fig 6.5. The shape of the clogged strontium on the back of the capillary array seems to suggest condensation as the most likely mechanism for the clogging of our capillaries. This requires that at any given time, the capillaries be the coldest part of the entire oven. One possible explanation for this is the following: at the capillaries we encounter two competing heat exchange mechanisms. On the one hand the large surface area of our capillary array compared to the body of the nozzle ensures that the capillaries radiate heat at a faster rate than the rest of the nozzle. This cooling is exacerbated by our open heat shields, since heat is no longer radiated back to the nozzle from the front. On the other hand, the capillaries are heated by the thermal contact to the walls of the clamps as well as radiatively from the crucible and the rest of the nozzle. However, the

poor thermal contact between individual capillaries as well as between the capillaries and the walls, ensures that radiative heat transfer is the dominant mode of heat exchange for our array. If the heat radiated away by the capillaries is larger than the heat radiating towards them from the crucible and the nozzle, then the steady-state temperature of the capillaries would be colder than its surroundings. Clearly, the clogging of our nozzle will have an effect on the lineshape of our atomic beam and consequently on the measured absorption profile. This is discussed in detail in the following section.

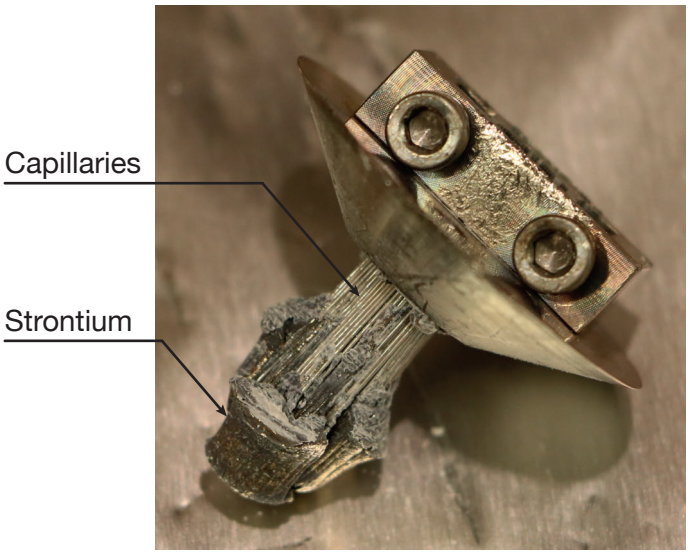

Figure 6.5 A photo of the clogged $\beta = 0.01$ nozzle. The shape of the clogging as a randomly distributed blob around the capillaries suggest condensation as the most likely mechanism of capillary clogging.

6.4 Results and Discussion

Our first measurements were taken with the β=0.027 and β=0.01 capillaries while the razor blade was fully retracted. The measured data from spectroscopy regions #1 and #2 is shown in the left and right panels of Fig. 6.6, respectively.

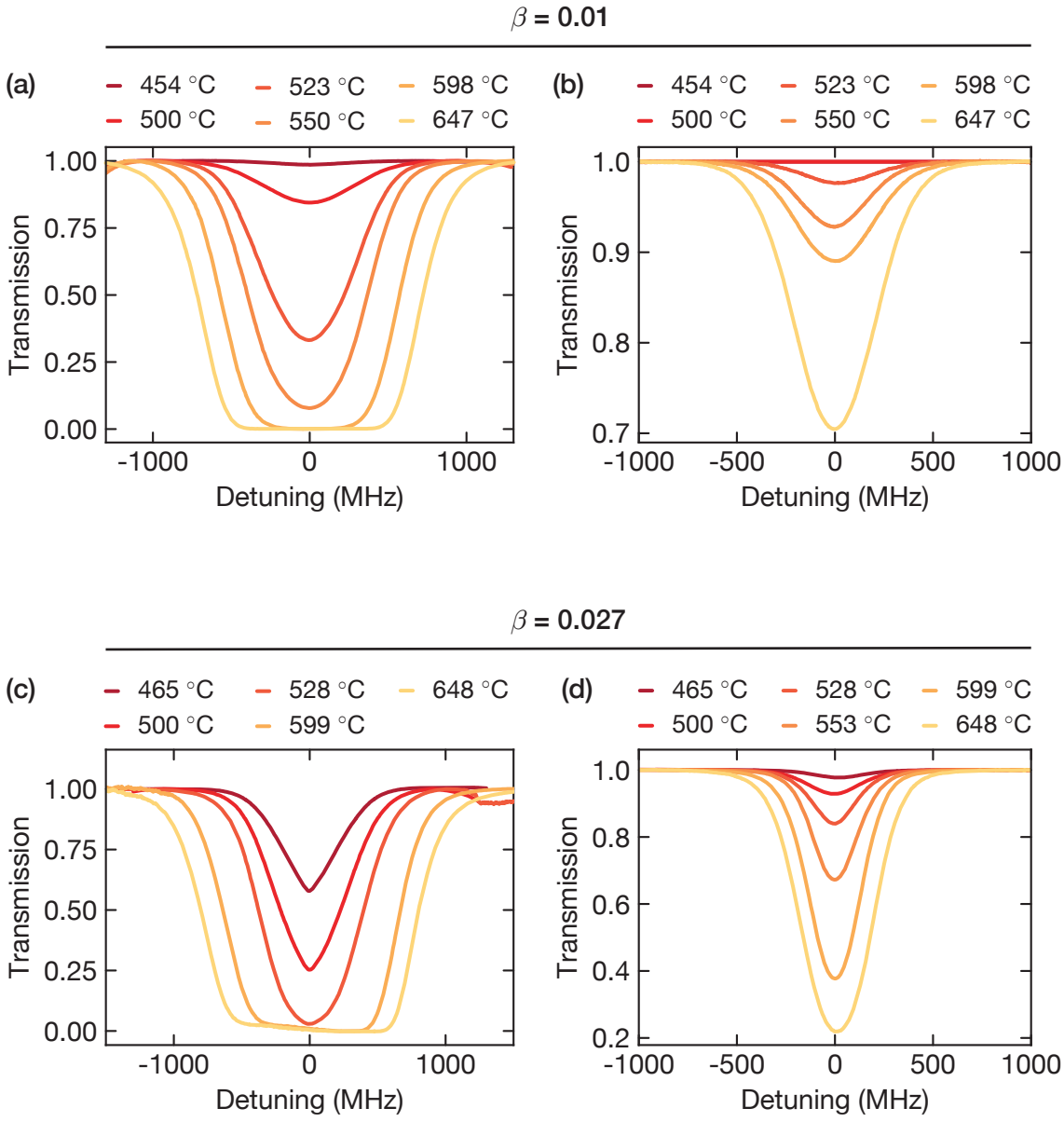

Figure 6.6 (a) and (b) show the measured transmission spectra for the $\beta = 0.01$ capillaries in spectroscopy regions #1 and #2, respectively. (c) and (d) show the same spectra for the $\beta = 0.027$ capillaries. In both regions the spectra are broader than expected from our model (see Fig. 6.7 for details), but clogging begins at an earlier stage in the $\beta = 0.01$ nozzle than in the $\beta = 0.027$ nozzle. This is clearly visible from the peaked shape at low temperatures in panel (c), a feature that is absent in panel (a).

Both datasets exhibit broader spectra than expected from our model, as demonstrated in Fig. 6.7. Our initial assumption was that the nozzles had clogged at some point during

the measurement due to the reduced temperature gradient between nozzle and crucible of ≈ 40 °C. In such a case it is reasonable to assume essentially thermal behavior of the gas along the spectroscopy direction and hence, a normal distribution of the atomic velocities in our beam. As such, we fitted a Gaussian distribution to our data which yielded much more accurate results (see Fig. 6.7). We can quantify this broadening by comparing the FWHM of our model with that of our Gaussian fit for $\beta = 0.027$ and T = 500 °C. Here we observe a discrepancy of $\approx 1 - \frac{370\text{MHz}}{530\text{MHz}}$=30 %. Particularly in the case of the β=0.027 capillaries, the Gaussian contribution to the spectra is less pronounced at low temperatures and increases gradually with increasing temperature until we are left with a purely Gaussian spectrum at circa 500 °C. This further supports our assumption that a clogging of the nozzle due to large exposed surface area available for radiative cooling is the reason for the broadening of our absorption spectra, since we would expect capillaries with a smaller aspect ratio to clog before those with a larger aspect ratio.
Broadening effects due to the lasers must also be taken into account. However, transit-time broadening contributes $\frac{4\bar{v}}{d}\sqrt{2\ln 2} \approx \frac{4\times 600\ \text{ms}^{-1}}{1\ \text{mm}}\sqrt{2\ln 2} \approx 3$ MHz, while any power broadening contribution was negligible due to the low intensities of ≈ 0.4 mW/cm^2. We also considered the possibility that some of the strontium from our nozzle was scattered at the edge of our heat shields in a Lambertian fashion, thereby artificially broadening our beam. However, only atoms emerging from our nozzle at an angle greater than ≈ 77° would see the outer heat shield. Of these atoms, around 13 % are scattered at an angle sufficient to arrive at spectroscopy region #1 and 1% at spectroscopy region #2. This would account for less than half of the broadening observed in region #1 and does not explain the temperature dependent nature of the broadening, nor the even larger deviation of our measured absorption spectra from our model in region #2.

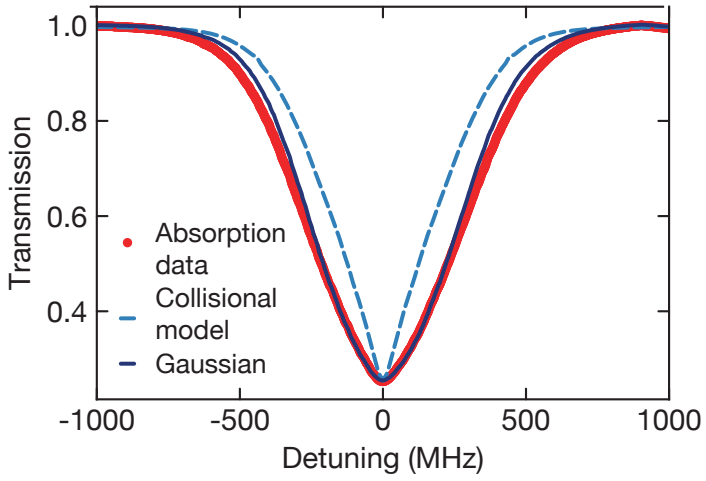

Figure 6.7 A comparison of the measured transmission spectrum for the $\beta = 0.027$ capillaries with the expected result from our collisional model of Chapter 2 (FWHM = 370 MHz) as well as a Gaussian (FWHM = 530 MHz) at T = 500 °C. The Gaussian fit is much more accurate than our model, indicating a clogged nozzle.

We also took data for varying razor blade positions for both the β=0.01 and β=0.027 capillaries, the results of which are shown in Fig. 6.8. As the razor blade cuts our beam, we expect a reduction in the peak height and a shift in the position of the peak. The latter is a consequence of the transverse velocity distribution of our atoms. As the razor blade cuts ever more atoms from our beam, those atoms with the highest transverse velocity i.e those at the tail end our velocity distribution, are discarded from the beam first. Since our spectroscopy beam no longer sees these atoms, the absorption peak will shift toward lower detunings. Surprisingly, we do not observe this behavior, rather, our absorption spectra are symmetric irrespective of the protrusion of our razor blade into the chamber as shown in Fig. 6.8 (a) and (b) for β = 0.01 and β = 0.027 respectively. One possible explanation for this behavior is the fact that the walls of the vacuum chamber eliminate the majority of atoms from our beam and especially those with a high transverse velocity component. Consequently, the effect of the Doppler shift on our transmission spectrum could be reduced to an almost negligible degree. A measurement of our transmission spectra at the highest possible oscilloscope resolution was made, but yielded inconclusive results. No major shift in the peaks position was visible and any shift that was present could also have been the result of laser drift over the measurement period.

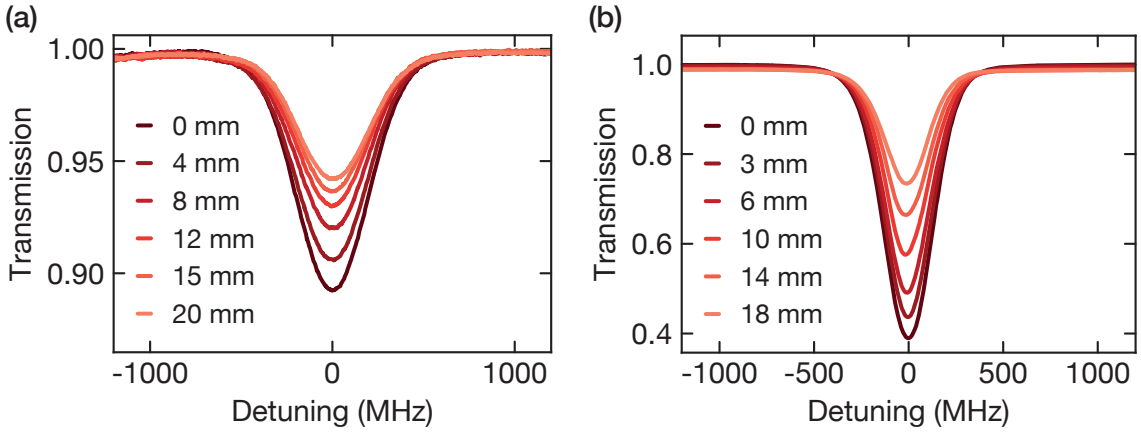

Figure 6.8 (a) The transmission spectrum recorded in spectroscopy region #2 for various razor blade protrusions and an aspect ratio of β=0.01. Interestingly, the expected shift in the peak position of the spectrum is not visible. (b) The same plot but for a capillary aspect ratio of β=0.027.

6.4.1 Clogging Transition

Given these results and the time constraints on this thesis, we decided to abandon our measurement of the oven efficiency and focus instead on understanding the precise mechanism for the clogging in our oven. For this purpose, we switched to the β=0.02 capillaries, where we had established an empirical basis for our numerical model by fitting it

to data from our current oven (see Chapter 2). Measuring with this capillary geometry would also allow us to draw direct comparisons between the new oven and our current oven. For ease of measurement we switched to our blue Toptica laser, which had a larger mode-hop free tuning range than our home-built ECDL. We began our measurement at a relatively low crucible temperature of 389 °C to ensure that no clogging was present. Subsequent measurements were taken at more frequent intervals than those of Fig. 6.6 so that the transition to a clogged regime would be clearly visible. The results of these measurements are shown in Fig. 6.9.

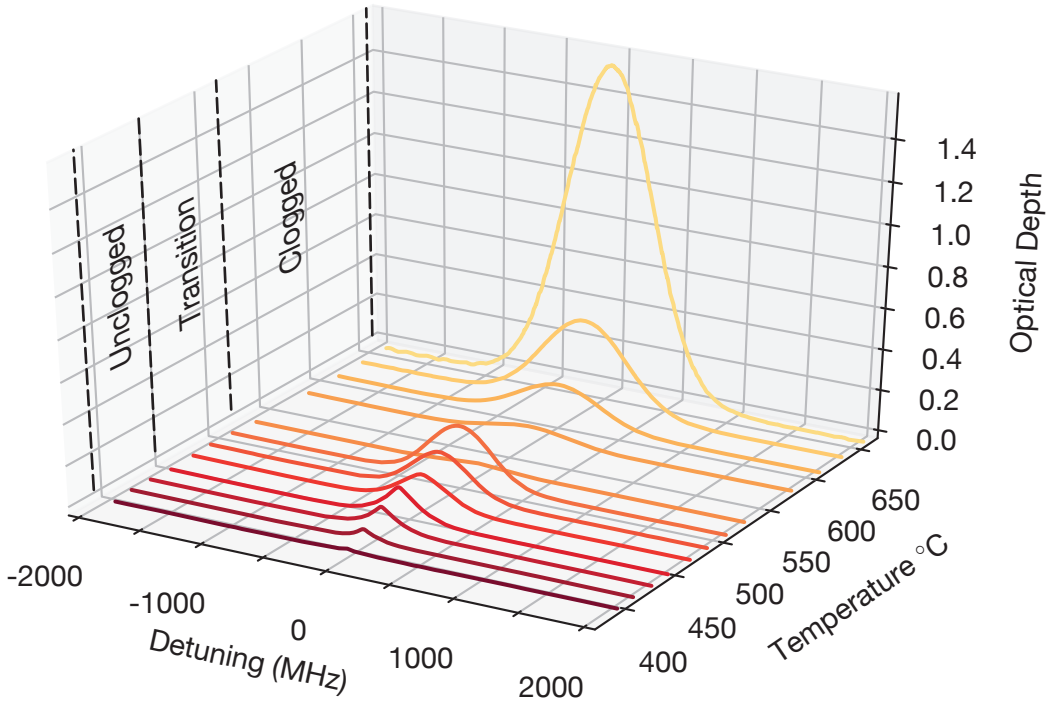

Figure 6.9 A plot of the optical depth for the $\beta = 0.02$ capillaries in spectroscopy region #1, showing the transition from an unclogged regime below 440 °C to a clogged regime above 520 °C. The unclogged regime is marked by a good agreement with the intermediate flow regime model developed in Chapter 2, while the clogged regime exhibits a Gaussian spectrum. The transition region is marked by an initial broadening and decrease in the peak height at a constant temperature of 520 °C.

As predicted, the low-temperature behavior of our atomic beam correlates well with our model up to 440 °C. We therefore know the nozzle to be unclogged below this temperature. Above this point we observe an initial broadening, marking the beginning of the clogging process (Fig. 6.10). The peak height begins to reduce at 500 °C settling to its minimial steady-state value at 520 °C. At this temperature the peak height was observed to remain constant for more than an hour. We therefore believe this value to represent a saturation of the nozzle and the endpoint of the clogging process. That this clogging

process is not observed in an identical fashion in the other capillary aspect ratios (e.g. there seems to be no reduction in the peak heights in the β=0.027 and β=0.01 data) could be attributed to the unpredictable fashion in which the capillaries clog.

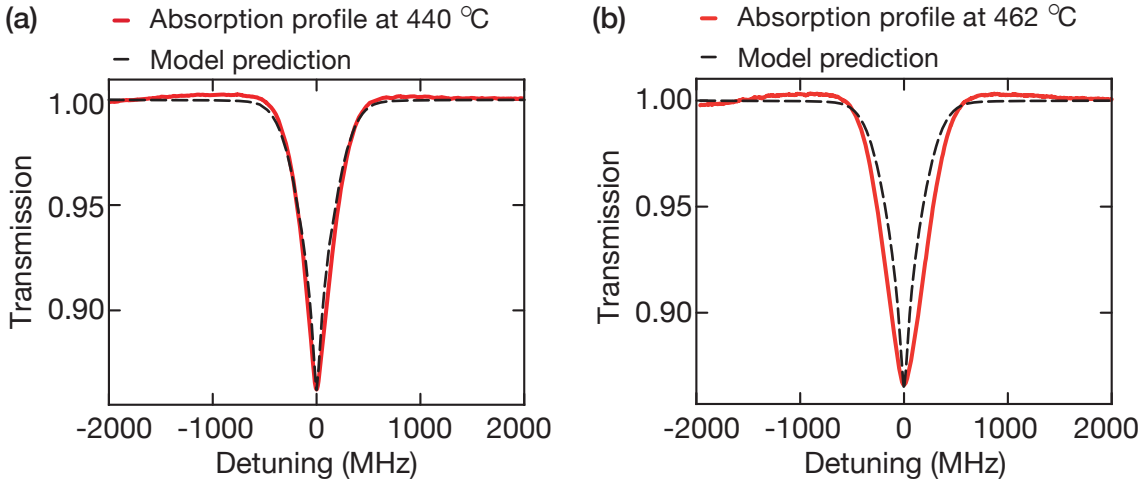

Figure 6.10 (a) The transmission spectrum of the $\beta = 0.02$ nozzle at 440 °C, just prior to the onset of clogging. (b) The transmission data for the same nozzle at 462 ° showing some broadening, which marks the beginning of the clogging process.

6.4.2 Verifying our Clogging Theory

Based on the above observations, we think it important to avoid any clogging of the nozzle. To test whether the reduced temperature gradient was indeed responsible for the clogging of the nozzle, as theorized in Subsection 6.3.3, we placed the old heat shields back onto the oven with the clogged $\beta = 0.02$ nozzle from before. Although this would again cut our beam, we were only interested in the central peak of the transmission spectrum, as in both the clogged and unclogged case these central atoms would make it into both spectroscopy regions. With the old heat shields back in place, we were again able to generate a temperature gradient of $\approx$ 75 °C between the nozzle and the crucible. Having established this gradient we began to uniformly heat both the crucible and the nozzle and observed the transmission spectra. The results are plotted in Fig. 6.11(b), next those of the clogged nozzle in Fig. 6.11(a).

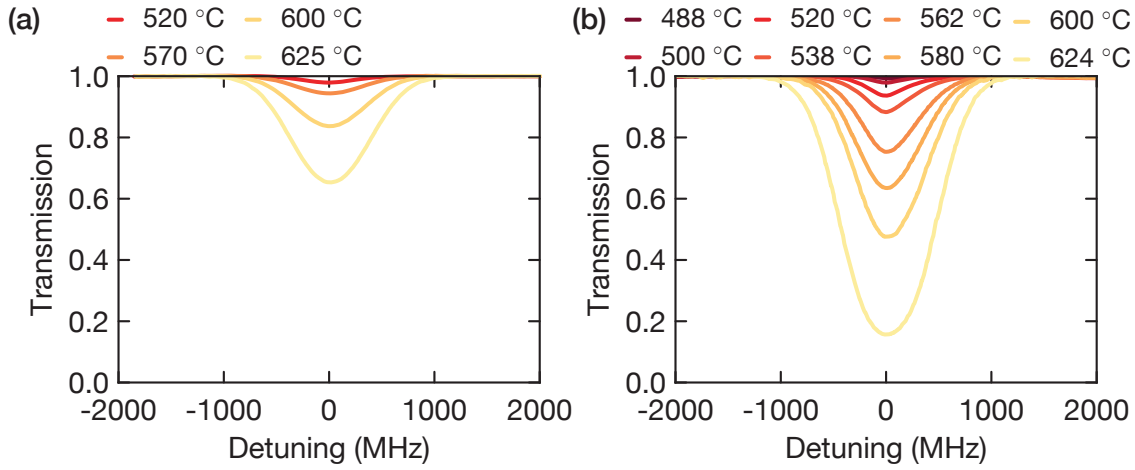

Figure 6.11 A comparison of the transmission data for our clogged nozzle shown in (a) and the same nozzle with our old heat shields and larger temperature gradient in (b). The increased transmission recorded with our old heat shields indicates that our previously clogged nozzle has become unclogged.

A much greater transmission signal for the same temperature is observed in the data recorded with our old heat shields and larger temperature gradient. This is a strong indicator that the nozzle has indeed unclogged.

From the measurements in this chapter we can conclude that the clogging of our oven leads to a significant broadening of our atomic beam and hence a much reduced efficiency and is an issue to be avoided. Although the clogging of our nozzles prevented us from measuring the usable flow of atoms from our oven and testing the predictions of Chapter 2, we were able to significantly improve our understanding of the clogging mechanism. It now seems clear, that clogging is caused by the condensation of strontium on the capillaries, perhaps due to the efficient cooling of the capillary array caused by its large surface area. This problem can be resolved by the a sufficiently large thermal gradient (in our case 75 °C). Our modification of the heat shields also revealed the practical difficulty associated with the measurement of absorption data directly after the nozzle and is something to be improved upon in the next iteration of this oven. While it is difficult to obtain an exact numerical value due to the breakdown of our model, the data taken in Figs. 6.3 and 6.11 provides a promising indicator for an increase of the total atomic flux in the forward direction when compared to our current oven.

Chapter 7

Conclusion and Outlook

The main aim of this thesis was to design, build and test a new oven for our experiment, that could deliver a high flux of usable atoms while maintaining a long lifetime. In Chapter 3, we reported on the design and construction of a new oven able to generate temperatures in excess of 750 °C and temperature gradients between the nozzle and the crucible of ≈ 90 °C. This was achieved by the use of two separate heating circuits and a double layer of heat shields. Furthermore, our oven has the capacity to hold up to 25 g of dendritic strontium, potentially increasing its lifetime far beyond that of our current oven. The interchangeable nozzle design allows us to adapt the collimation properties of our atomic beam as needed.
The clipping of the beam by our heat shield apertures initially prevented us from measuring the efficiency of our oven. We subsequently modified our heat shields to circumvent this problem only to encounter clogging at the nozzle due to a reduced thermal gradient between the nozzle and the crucible. This demonstrates the difficulty of measuring the beam directly after the nozzle and poses a problem that is common to the majority of cold atom experiments which want to measure the efficiency of their atomic beams. However, our oven can easily be modified in the next iteration to counteract this issue.

Though the clogging of our nozzle prevented any further measurements regarding the predictions of Chapter 2, we used this opportunity to come to a better understanding of the clogging mechanism. We first observed a transition from an unclogged regime to a clogged one for capillaries with an aspect ratio of $\beta = 0.02$. The transition occurred between 440 °C and 520 °C and was characterized by an initial broadening followed by a reduced transmission at the saturation point of 520 °C. We further observed a homogeneously distributed clump of strontium on the ends of our capillaries upon opening the oven. Together with the clogging transition, this led us to hypothesize that the clogging was caused by condensation on the capillary array due to efficient radiative cooling caused by its large surface area. We tested this hypothesis by placing our old heat shield back on the oven and observing the peak transmission. With a temperature gradient of 75 °C between the nozzle and the crucible, a much higher peak transmission was observed, strongly suggesting an unclogged nozzle. Given these observations, we feel confident in stating that the clogging of microcapillary arrays in effusive ovens is caused by condensation due to an insufficient thermal gradient between the array and its surroundings.

In the course of this thesis we also built and tested a 461 nm linear external cavity diode laser for use during the absorption measurements on our oven. For these measurements our laser had to achieve a free-running linewidth of less than 30.24(2) MHz and a mode-hop free tuning range of several GHz. A heterodyne beat with a 461 nm DL Pro locked to a spectroscopy cell set an upper limit of 3.6 MHz (with an RBW = 300 kHz) on the former. After initial difficulties due to competition between the feed-forward and the piezo offset, the latter was optimized to 6.8(1) MHz. The usable output power of our laser at the working point was measured to be 41.7 mW. For the purposes of this thesis these paramters are more than sufficient and given the difficulties associated with blue laser diodes (as discussed in Chapter 4), represent an encouraging step towards a home-built blue diode laser for our lab.

Numerous future improvements to both the oven and the laser are necessary. First and foremost, we suggest moving the heat shields closer to the nozzle and increasing the aperture size by a factor of two. This way, enough heat is radiated back by the heat shields to ensure a sufficient thermal gradient and prevent clogging, but clipping of the beam is reduced. More heat shield layers with a smaller wall thickness would increase the temperature gradient still further, while also reducing the necessary power required to heat our oven to high temperatures.
The implementation of in-vacuum water cooling of our oven should be another priority. This would reduce outgassing from our oven at high temperatures, preventing an increase in pressure and the associated reduction of the in-trap lifetime of our atoms. A potential cooling scheme was presented at the end of Chapter 3.
Lastly, the reloading process of our oven needs to be simplified. Two suggestions to this point were presented in Subsection 6.3.1 and involve the replacement of screws with a simple “clip-on” mechanism and the drilling of additional holes for better thermocouple placement.

Regarding our laser, modifications to the housing need to be made. Specifically, proper feedthroughs for DC current modulation need to be installed in the back-plate of the housing and one of the male 9 pin sub-D feedthoughs replaced with its female counterpart. In addition, the PCB should be placed outside the housing to allow for the evacuation of the laser without having to worry about the vacuum compatibility of electronic components. We should also find an ’on-board’ solution for the analog inverter necessary to optimize the mode-hop free tuning range of our laser, so as to minimize any potential noise sources on our laser. Generally, the propensity of our laser to mode-hop warrants further investigation into its stability. We could, for example, look at using a properly coated mirror instead of a beam splitter plate as our output coupler and/or at replacing our broad bandpass interference filter with a narrow-band one. Finally, a three-way beat between our linear laser, the blue DL Pro and another 461 nm laser could be performed to determine the individual linewidth of each. In combination with the oven improvements mentioned above, these changes would enable us to implement our planned 2D MOT and measure its effect on the efficiency of our oven. On the whole, we are confident that the suggested improvements are relatively straightforward to implement and will allow us to

use our new atom source in the experiment soon.

References

[1] Greiner, M., O. Mandel, T. Esslinger, T. W. Hänsch, and I. Bloch. *Quantum phase transition from a superfluid to a Mott insulator in a gas of ultracold atoms*, Nature **415**, 39–44 (2002). DOI: 10.1038/415039a.

[2] Köhl, M., H. Moritz, T. Stöferle, K. Günter, and T. Esslinger. *Fermionic Atoms in a Three Dimensional Optical Lattice: Observing Fermi Surfaces, Dynamics, and Interactions*, Physical Review Letters **94**, 080403 (2005). DOI: 10.1103/PhysRevLett.94.080403.

[3] Schauß, P., M. Cheneau, M. Endres, T. Fukuhara, S. Hild, A. Omran, T. Pohl, C. Gross, S. Kuhr, and I. Bloch. *Observation of spatially ordered structures in a two-dimensional Rydberg gas*, Nature **491**, 87–91 (2012). DOI: 10.1038/nature11596.

[4] Jotzu, G., M. Messer, R. Desbuquois, M. Lebrat, T. Uehlinger, D. Greif, and T. Esslinger. *Experimental realization of the topological Haldane model with ultracold fermions*, Nature **515**, 237–240 (2014). DOI: 10.1038/nature13915.

[5] Lahaye, T., C. Menotti, L. Santos, M. Lewenstein, and T. Pfau. *The physics of dipolar bosonic quantum gases*, Reports on Progress in Physics **72**., 126401 (2009). DOI: 10.1088/0034-4885/72/12/126401.

[6] Ludlow, A. D., M. M. Boyd, T. Zelevinsky, S. M. Foreman, S. Blatt, M. Notcutt, T. Ido, and J. Ye. *Systematic Study of the ^{87}Sr Clock Transition in an Optical Lattice*, Physical Review Letters **96**, 033003 (2006). DOI: 10.1103/PhysRevLett.96.033003.

[7] Bakr, W. S., J. I. Gillen, A. Peng, S. Fölling, and M. Greiner. *A quantum gas microscope for detecting single atoms in a Hubbard-regime optical lattice*, Nature **462**, 74–77 (2009). DOI: 10.1038/nature08482.

[8] Cheuk, L. W., M. A. Nichols, M. Okan, T. Gersdorf, V. V. Ramasesh, W. S. Bakr, T. Lompe, and M. W. Zwierlein. *Quantum-Gas Microscope for Fermionic Atoms*, Physical Review Letters **114**, 193001 (2015). DOI: 10.1103/PhysRevLett.114.193001.

[9] Parsons, M. F., F. Huber, A. Mazurenko, C. S. Chiu, W. Setiawan, K. Wooley-Brown, S. Blatt, and M. Greiner. *Site-Resolved Imaging of Fermionic ^{6}Li in an Optical Lattice*, Physcial Review Letters **114**, 213002 (2015). DOI: 10.1103/PhysRevLett.114.213002.

[10] Gross, C. and I. Bloch. *Quantum simulations with ultracold atoms in optical lattices*, Science **357**., 995–1001 (2017). DOI: 10.1126/science.aal3837.

[11] Campbell, S. L. *et al. A Fermi-degenerate three-dimensional optical lattice clock*, Science **358**., 90–94 (2017). DOI: 10.1126/science.aam5538.

[12] González-Tudela, A., C. S. Muñoz, and J. I. Cirac. *Engineering and Harnessing Giant Atoms in High-Dimensional Baths: A Proposal for Implementation with Cold Atoms*, Physical Review Letters **122**, 203603 (2019). DOI: 10.1103/PhysRevLett.122.203603.

[13] Krinner, L., M. Stewart, A. Pazmiño, J. Kwon, and D. Schneble. *Spontaneous emission of matter waves from a tunable open quantum system*, Nature **559**, 589–592 (2018). DOI: 10.1038/s41586-018-0348-z.

[14] Cazalilla, M. A. and A. M. Rey. *Ultracold Fermi gases with emergent SU (N) symmetry*, Reports on Progress in Physics **77**, 124401 (2014). DOI: 10.1088/0034-4885/77/12/124401.

[15] Dick, G. J. *Local oscillator induced instabilities in trapped ion frequency standards*, (1987).

[16] Ludlow, A. D., M. M. Boyd, and J. Ye. *Optical Atomic Clocks*, Reviews of Modern Physics **87**, 637–701 (2015). DOI: 10.1103/RevModPhys.87.637.

[17] Kaubruegger, R., P. Silvi, C. Kokail, R. van Bijnen, A. M. Rey, J. Ye, A. M. Kaufman, and P. Zoller. *Variational spin-squeezing algorithms on programmable quantum sensors*, arXiv: 1908.08343 (2019).

[18] Cho, A. Y. and J. R. Arthur. *Molecular Beam Epitaxy*, Progress in Solid State Chemistry **10**, 157–191 (1975). DOI: 10.1016/0079-6786(75)90005-9.

[19] G.King, J. and J. R.Zacharias. *Some New Applications and Techniques of Molecular Beams*, Advances in Electronics and Electron Physics **8**, 1–88 (1956). DOI: 10.1016/S0065-2539(08)61225-1.

[20] Ramsey, N. *Molecular Beams*. Oxford: Oxford University Press, 1956. ISBN: 0-19-852021-2.

[21] Vanier, J. and C. Audoin. *The Quantum Physics of Atomic Frequency Standards*. Vol. 2. Bristol and Philadelphia: IOP Publishing Ltd, 1989. ISBN: 0-85274-433-1.

[22] Senaratne, R., S. V. Rajagopal, Z. A. Geiger, K. M. Fujiwara, V. Lebedev, and D. M. Weld. *Effusive atomic oven nozzle design using an aligned microcapillary array*, Review of Scientific Instruments **86**, 023105 (2015). DOI: 10.1063/1.4907401.

[23] Schioppo, M., N. Poli, M.prevedelli, S. Falker, C. Lisdat, U. Sterr, and G. M. Tino. *A compact and efficient strontium oven for laser-cooling experiments*, Review of Scientific Instruments **83**, 103101 (2012). DOI: 10.1063/1.4756936.

[24] Demtröder, W. *Laserspektroskopie*. 4th ed. Berlin-Heidelberg: Springer, 2000. ISBN: 3-540-64219-6.

[25] Metcalf, H. J. *Laser Cooling and Trapping*. New York: Springer, 1999. ISBN: 978-0-387-98728-6.

[26] Inguscio, M. and L. Fallani. *Atomic Physics*. Oxford: Oxford University Press, 2015. ISBN: 978-0-19-852584-4.

[27] Ashkin, A. and J. P. Gordon. *Stability of radiation-pressure particle traps: an optical Earnshaw theorem*, Optics Letters **8**., 511–513 (1983). DOI: 10.1364/OL.8.000511.

[28] Snigirev, S., A. J. Park, A. Heinz, I. Bloch, and S. Blatt. *Fast and dense magneto-optical traps for strontium*, Physical Review A **99**, 063421 (2019). DOI: 10.1103/PhysRevA.99.063421.

[29] Yasuda, M., T. Kishimoto, M. Takamoto, and H. Katori. *Photoassociation spectroscopy of ^{88}Sr: Reconstruction of the wave function near the last node*, Physical Review A **73**, 011403 (2006). DOI: 10.1103/PhysRevA.73.011403.

[30] Cooper, A., J. P. Covey, I. S. Madjarov, S. G. Porsev, M. S. Safronova, and M. Endres. *Alkaline-Earth Atoms in Optical Tweezers*, Physical Review X **8**, 041055 (2018). DOI: 10.1103/PhysRevX.8.041055.

[31] Xu, X., T. H. Loftus, J. L. Hall, A. Gallagher, and J. Ye. *Cooling and trapping of atomic strontium*, Journal of the Optical Society of America B **20**., 291 (2003). DOI: 10.1364/JOSAB.20.000968.

[32] Heinz, A., A. J. Park, J. Trautmann, N. Šantić, S. Porsev, M. Safronova, I. Bloch, and S. Blatt. "State-dependent optical lattices for strontium". In preparation. 2019.

[33] Taichenachev, A. and V. I. Yudin. *Magnetic Field-Induced Spectroscopy of Forbidden Optical Transitions with Application to Lattice-Based Optical Atomic Clocks*, Physical Review Letters **96**, 083001 (2006). DOI: 10.1103/PhysRevLett.96.083001.

[34] Nosske, I., L. Couturier, F. Hu, C. Tan, C. Qiao, J. Blume, Y. H. Jiang, P. Chen, and M. Weidemüller. *Two-dimensional magneto-optical trap as a source for cold strontium atoms*, Physical Review A **96**, 053415 (2017). DOI: 10.1103/PhysRevA.96.053415.

[35] Vanier, J. and C. Audoin. *The Quantum Physics of Atomic Frequency Standards*. Vol. 1. Bristol and Philadelphia: IOP Publishing Ltd, 1989. ISBN: 0-85274-432-3.

[36] Janša, N. "A frequency-stable diode laser system for spectroscopy and trapping of Sr atoms". MA thesis. Ludwig-Maximilians-Universität, 2016. URL: http://www.ultracold.sr/publications/.

[37] Olander, D. R. and V. Kruger. *Molecular Beam Sources Fabricated from Multichannel Arrays. III. The Exit Density Problem*, Journal of Applied Physics **41**, 2769 (1970). DOI: 10.1063/1.1659313.

[38] Clausing, P. *Over den verblijftijd van moleculen en de strooming van zeer verdunde gassen*. Amsterdam: Paris, 1928.

[39] Cheuk, L. W., M. A. Nichols, M. Okan, T. Gersdorf, V. V. Ramasesh, W. S. Bakr, T. Lompe, and M. W. Zwierlein. *Über die Strahlformung bei der Molekularströmung*, Zeitschrift für Physik **66**, 471–476 (1930). DOI: 10.1007/BF01402029.

[40] Clausing, P. *Über die Strömung sehr verdünnter Gase durch Röhren von beliebiger Länge*, Annalen der Physik **12**, 961 (1932). DOI: 10.1002/andp.19324040804.

[41] Pauly, H. *Other Low-Energy Beam Sources*, *Atomic and Molecular Beam Methods*. Ed. by Scoles, G. Vol. 1. Oxford: Oxford University Press, 1988. Chap. 4, pp. 83–123. ISBN: 0-19-504280-8.

[42] Giordmaine, J. A. and T. C. Wang. *Molecular Beam Formation by Long Parallel Tubes*, Journal of Applied Physics **31**, 463 (1960). DOI: 10.1063/1.1735609.

[43] *Permodur 4841*. 1.4841. DEW. Feb. 2016. URL: https://www.dew-stahl.com/produkte/rsh-stahl/ (visited on 09/12/2019).

[44] *Inconel alloy 600*. SMC-027. Special Metals. Sept. 2002. URL: http://www.specialmetals.com/tech-center/alloys.html (visited on 09/12/2019).

[45] *Monel alloy 400*. SMC-053. Special Metals. Feb. 2005. URL: http://www.specialmetals.com/tech-center/alloys.html (visited on 09/12/2019).

[46] Baillard, X. “Horloge à réseau optique à atomes de Strontium”. PhD thesis. l’Université de Paris VI, 2008. URL: https://tel.archives-ouvertes.fr/tel-00267252/.

[47] *Macor*. Corning Inc. 2012. URL: https://www.corning.com/emea/de/products/advanced-optics/product-materials/specialty-glass-and-glass-ceramics/glass-ceramics/macor.html (visited on 09/12/2019).

[48] Desai, P. D., T. K. Chu, H. M. James, and C. Y. Ho. *Electrical Resistivity of Selected Elements*, J. Phys. Chem. Ref. Data **13**., 1074–1078 (1984). DOI: 10.1063/1.555723.

[49] Forge, C. *How does Forging Affect Grain Structure?* URL: http://www.dropforging.net/how-does-forging-affect-grain-structure.html (visited on 09/29/2019).

[50] Siegman, A. E. *Lasers*. Sausalito, California: University Science Books, 1986. ISBN: 0-935702-11-3.

[51] Risken, H. and T. Frank. *The Fokker-Planck Equation*. 2nd ed. Berlin-Heidelberg: Springer, 1996. ISBN: 978-3-540-61530-9.

[52] Gardiner, C. W. and P. Zoller. *Quantum Noise*. 3rd ed. Berlin-Heidelberg: Springer, 2004. ISBN: 3-540-22301-0.

[53] Langevin, P. *Sur la théorie du mouvement brownien*, Comptes rendus de l'Académie des sciences **146**, 530–533 (1908). URL: https://gallica.bnf.fr/ark:/12148/bpt6k3100t/f530.image.r=Sur%20la%20th%C3%A9orie%20du%20mouvement%20brownien?rk=42918;4 (visited on 09/02/2019).

[54] Louisell, W. H. *Quantum Statistical Properties of Radiation*. Hoboken, New Jersey: John Wiley & Sons, Inc., 1990. ISBN: 0-471-52365-8.

[55] Haken, H. *Synergetics, an Introduction*. Berlin-Heidelberg: Springer, 1983. ISBN: 978-3-642-88338-5.

[56] Papoulis, A. *Probability, Random Variables ans Stochastic Processes*. 3rd ed. New York: McGraw-Hill Inc., 1991. ISBN: 0-07-048477-5.

[57] Wiener, N. *Generalized harmonic analysis*, Acta Mathematica **55**, 117–258 (1930). DOI: 10.1007/BF02546511.

[58] Chow, W. W. and S. W. Koch. *Semiconductor-Laser Fundamentals*. Berlin-Heildeberg: Springer, 1999. ISBN: 3-540-64166-1.

[59] Yamada, M. *Theory of Semiconductor Lasers*. Tokyo: Springer, 2014. ISBN: 978-4-431-54889-8.

[60] Ashcroft, N. W. and N. D. Mermin. *Solid State Physics*. Philadelphia: Saunders College, 1976. ISBN: 0-03-049346-3.

[61] Homeier, L. "Setup and characterization of a Littrow laser for 689 nm". BSc Thesis. Ludwig-Maximilians-Universität München, 2017.

[62] Nakamura, S. and G. Fasol. *The Blue Laser Diode*. Berlin-Heidelberg: Springer, 1997. ISBN: 3-540-61590-3.

[63] Amano, H., N. Sawaki, and I. Akasaki. *Metalorganic vapor phase epitaxial growth of a high quality GaN film using an AlN buffer layer*, Applied Physics Letters **48**, 353 (1986). DOI: 10.1063/1.96549.

[64] Amano, H., M. Kito, K. Hiramatsu, and I. Akasaki. *P-Type Conduction in Mg-Doped GaN Treated with Low-Energy Electron Beam Irradiation (LEEBI)*, Japanese Journal of Applied Physics **28**., L2112–L2114 (Dec. 1989). DOI: 10.1143/jjap.28.l2112.

[65] Nakamura, S., T. Mukai, M. Senoh, and N. Iwasa. *Thermal Annealing Effects on P-Type Mg-Doped GaN Films*, Japanese Journal of Applied Physics **31**, L139–L142 (1992). DOI: 10.1143/jjap.31.l139.

[66] Nakamura, S., T. Mukai, M. Senoh, S.-i. Nagahama, and N. Iwasa. *$In_xGa_{(1-x)}N/In_yGa_{(1-y)}N$ superlattices grown on GaN films*, Journal of Applied Physics **74**., 3911–3915 (1993). DOI: 10.1063/1.354486.

[67] Brown, I. H., P. Blood, P. M. Smowton, J. D. Thomson, S. M. Olaizola, A. M. Fox, P. J. Parbrook, and W. W. Chow. *Time Evolution of the Screening of Piezoelectric Fields in InGaN Quantum Wells*, IEEE Journal of Quantum Electronics **42**., 1202–1208 (2006). DOI: 10.1109/ISLC.2006.1708096.

[68] Risk, W. P., T. R. Gosnell, and A. V. Nurmikko. *Compact Blue-Green Lasers*. Cambridge: Cambdrige University Press, 2003. ISBN: 0 521 62318 9.

[69] Wang, W., W. Xie, Z. Deng, H. Yang, M. Liao, J. Li, X. Luo, S. Sun, and D. Zhao. *Performance Improvement of GaN Based Laser Diode Using Pd/Ni/Au Metallization Ohmic Contact*, Coatings **9**., 291 (2019). DOI: 10.3390/coatings9050291.

[70] Saleh, B. E. A. and M. C. Teich. *Fundamentals of Photonics*. 2nd ed. Hoboken, New Jersey: John Wiley & Sons, Inc., 2007. ISBN: 978-0-471-35832-9.

[71] Loudon, R. *The Quantum Theory of Light*. Oxford: Oxford University Press, 2010. ISBN: 978-0-19-850176-3.

[72] Finger, F. "A Transport Laser with Shape and Amplitude Control for Ultracold Strontium Atoms". MA thesis. Technische Universität München, 2018. URL: http://www.ultracold.sr/publications/.

[73] Mansuripur, M. and E. Wright. *The optics of semiconductor diode lasers*, Optics and Photonics News **13**, 57–61 (July 2002).

[74] Kokhanovskyi, I. "Construction of an interference-filter-stabilized diode laser for experiments with ultracold strontium atoms". BSc Thesis. Ludwig-Maximilians-Universität München, 2019.

[75] Baillard, X., A. Gauguet, S. Biz, P. Lemondem, P. Laurent, A. Clairon, and P. Rosenbusch. *Interference-filter-stabilized external-cavity diode lasers*, Optics Communications **266**, 609–613 (2006). DOI: 10.1016/j.optcom.2006.05.011.

[76] Lesker, K. J. *Torr Seal Low Vapor Pressure Epoxy*. URL: http://www.lesker.com/newweb/fluids/sealants-epoxy/torrseal/ (visited on 08/21/2019).

[77] Scholl, M., W. Cairncross, and I. Kivlichan. *Interference Filter Stabilized External-Cavity Diode Lasers*. Tech. rep. Univeristy of Toronto, 2012.

[78] Schäfter-Kirchhoff. *Laser Diode Collimators 20C and 20P*. URL: https://www.sukhamburg.com/products/Laser_Diode_Collimators_20C_and_20P.html (visited on 10/01/2019).

[79] Thorlabs. *Comparison of Circularization Techniques for Elliptical Beams*. URL: https://www.thorlabs.com/newgrouppage9.cfm?objectgroup_id=11426 (visited on 08/26/2019).

[80] Hoyer, C. "Aufbau eines Resonators hoher Finesse zur Linienbreitenmessung". BSc Thesis. Technische Universität Darmstadt, 2013.

[81] Sirah. *EagleEye, Optical Spectrum Analyzer*. URL: http://www.sirah.com/tools/eagleeye/unit (visited on 08/27/2019).

[82] Chen, Y.-C. *A tutorial on kernel density estimation and recent advances*, Biostatistics & Epidemiology **1**., 161–187 (2017). DOI: 10.1080/24709360.2017.1396742.

[83] *Sys DC 110 Diode Laser Supply Electronics*. 10th ed. Toptica Photonics AG. 2015.

[84] David W. Allan Neil Ashby, C. C. H. *The Science of Timekeeping*. Tech. rep. Hewlett Packard, 1997.

[85] Riley, W. J. *Handbook of Frequency Stability Analysis*. NIST Special Publication 1065. 2008. URL: https://www.nist.gov/publications/handbook-frequency-stability-analysis.

Acknowledgements

First and foremost I would like to thank my supervisor, Dr. Sebastian Blatt. His knowledge and dedication inspired me to go beyond what I thought possible at the outset of this thesis. He was responsible for taking a Bachelor student with no prior experimental experience to speak of and giving him the tools necessary to work independently in the lab.

I would also like to thank Prof. Dr. Immanuel Bloch for giving me the opportunity to work and be part of his group.

A special thanks goes to Dr. Neven Šantić for his tireless support, invaluable advice, endless patience and the rare ability to explain complicated ideas in an understandable fashion. This thesis simply would not have been possible without him and I am extremely grateful to have had his help along the entire way.

From one master student to another, my thanks goes to Rudi Haindl, for challenging me to come to a better understanding of the physics I was conducting and for his honest advice and support when it counted.

I also want to thank André Heinz for his help throughout my thesis and for providing me with many a challenging and fun conversation.

My thanks also goes to Annie Park for always taking the time to listen and think about any problems that I had in the lab and for her kind words of support which I could always count on.

Thanks also to Jan Trautmann for providing some much needed level-headed thinking when I was stuck with a problem and for teaching me how to work with the plumping for the lab.

I would also like to thank Dr. Stepan Snigirev for his mentoring during my initial internship at the MPQ and the beginning of my Masters thesis. I also want to thank Fabian Finger for bringing some levity to daily lab life when things threatened to become a grind.

Another great thank you goes to Anton Mayer, without whose limitless experience regarding mechanical engineering this thesis would not have been possible. I particularly want to thank him for always taking the time not just to help me with my designs but to explain the underlying manufacturing processes. Additionally, I would like to extend my thanks to the entire workshop. Without their manufacturing skills this thesis would not have developed as speedily as it did.

I also want to thank all the members of the Bloch group for their advice and friendship. It has made working in this group a truly wonderful experience!

Finally, I want to thank my family, for all their love and support throughout the writing of this thesis. Particularly, on days when things didn't go so smoothly.

Appendix A

Atom Flow through Differential Pumping Tubes

In this Appendix we will illustrate the effect that the differential pumping tubes in our current vacuum system have on the efficiency of our oven. To this end, we will derive an analytic expression for the fraction of atoms that make it through these tubes as a function of the position of the capillary from which the atoms originated. The differential pumping tubes are necessary to regulate the pressure between the oven section of our vacuum system and the MOT chamber. If these did not exist, the pressure in the MOT chamber would be on the order of 10^{-5} mbar and the lifetime of our atoms would be too short to be useful in any experiments.

To begin, we consider the construction shown in Figs. A.1 and A.2.

These figures are designed to illustrate the following scenario: Beginning in the center of the nozzle we want to know what fraction of atoms passes through the differential pumping tube without any wall collisions. To this end, we project the final aperture of the tube onto the initial one (as illustrated by the grey circles in the side view). The size and position of the projection is determined by the position of the capillary. In the case of the central capillary, for example, $\theta_{max} = \theta_{crit}$. As we move up the nozzle to the next capillary in the row, θ_{max} increases and θ_{crit} decreases. The limiting case is achieved when we arrive at a capillary whose center is exactly in line with the edge of the differential pumping tube. In this case $\theta_{max} = \arctan\left(\frac{5}{168}\right)$ and $\theta_{crit} = 0$.

Next we turn our attention to the ϕ degree of freedom. All atoms emerging from a capillary at an angle $\theta < \theta_{crit}$ will make it through the differential pumping tube (DPT) and hence for θ's in this range it is irrelevant at which ϕ they emerge from the capillary. This means that for $\theta < \theta_{crit}$ we can integrate over 2π. This limit is indicated by the solid magenta line in the above construction. However, for atoms emerging from the capillary with a $\theta > \theta_{crit}$, this is not the case and only a fraction make it through the DPT.

As we increase θ, the dashed magenta circle increases. The intersection of this circle with the projection of the final aperture (point C on the front view) limits the range of ϕ for a given θ. As θ increases further, the point C will traverse the circumference of the projection until it reaches D, at which point $\phi = 0$.

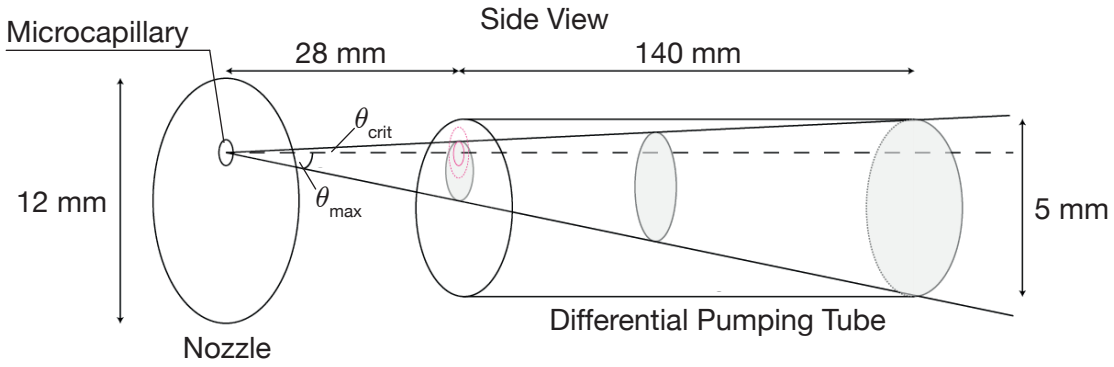

Figure A.1 Atoms emerging from different capillaries in our nozzle will see the back aperture of the differential pumping tube projected onto its front face in different ways. This effectively sets the angular integration limits for the calculation of the fraction of atoms to make it through the tubes. The height h is determined by the critical angle $\theta_{textcrit}$ under which atoms still make it through the tubes without collisions. The counterpart of this angle for the other side of the tube is θ_{max}.

We can translate this behavior into a mathematical description of ϕ as a function of θ in the following manner: First, we define all relevant quantities

$$\begin{aligned} \theta_{crit} &= \arctan\left(\frac{h}{168}\right) \\ \theta_{max} &= \arctan\left(\frac{5-h}{168}\right) \\ AB &= 28\tan(\theta_{crit}) = \frac{h}{6} \\ AC &= 28\tan(\theta) \\ OC &= 28\left(\frac{2.5}{168}\right) = \frac{5}{12} \end{aligned} \tag{A.1}$$

where h is the distance of the capillary center from the edge of the DPT (as indicated in the side view above). Furthermore

$$OA = OC - AB = \frac{5}{12} - \frac{h}{6}. \tag{A.2}$$

Thus, according to the cosine rule

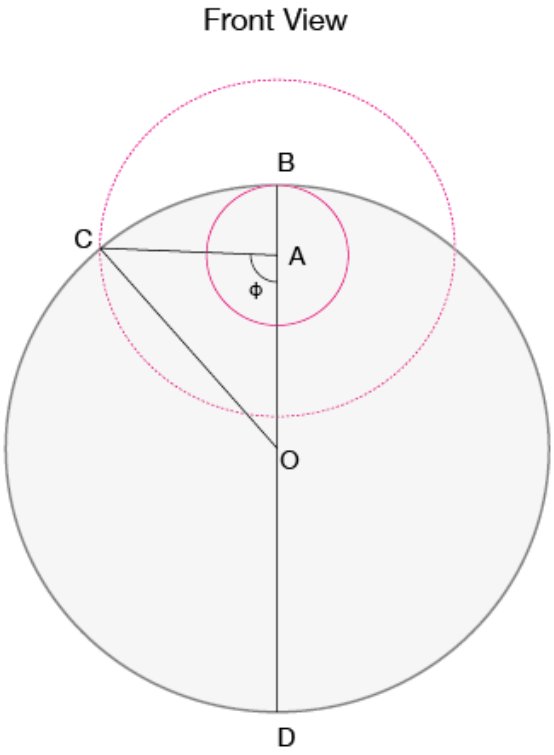

Figure A.2 A schematic representation of the projection of the final differential pumping tube aperture. The solid magenta circle represents the boundary of θ values for which we can still integrate the ϕ degree-of-freedom over 2π. Beyond this boundary, the range of ϕ values over which we can integrate is given by the intersection of the dashed magenta circle with the boundary of the projection.

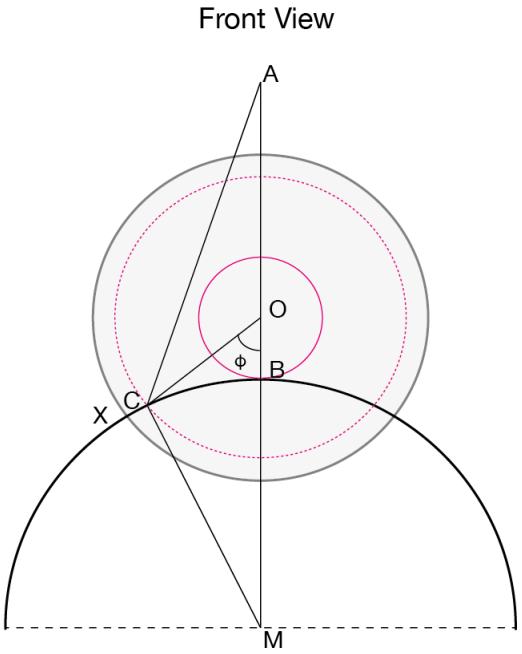

Figure A.3 A modified geometry for those atoms originating at capillaries lying outside the edge of the differential pumping tube.

$$\begin{aligned}\phi(\theta,h) &= \arccos\left(\frac{AC^2+OA^2-OC^2}{2ACOC}\right)\\ &= \arccos\left(\frac{(28tan(\theta))^2+\left(\frac{5}{12}-\frac{h}{6}\right)^2-\left(\frac{5}{12}\right)^2}{56\tan(\theta)\left(\frac{5}{12}-\frac{h}{6}\right)}\right).\end{aligned} \tag{A.3}$$

This is description is valid up to the limiting case of a capillary whose center is exactly in line with the edge of the differential pumping tube. Beyond this point, that is to say, for capillaries whose center lie outside the initial DPT aperture, we need to modify our model slightly. The situation now looks like this:

This construction places severe limits on the range of θ values, since only atoms between the point B and the edge of the aperture projection will not collide with the wall of the DPT. Taking A as the origin we define

$$\begin{aligned}\widetilde{\theta}_{crit} &:= \arctan\left(\frac{h}{28} - \frac{2.5+h}{168}\right) = \arctan\left(\frac{5h-2.5}{168}\right)\\ \widetilde{\theta}_{max} &:= \arctan\left(\frac{5+h}{168} - \frac{2.5+h}{168}\right) = \arctan\left(\frac{2.5}{168}\right)\end{aligned} \tag{A.4}$$

where $\widetilde{\theta}_{crit} \leq \theta \leq \widetilde{\theta}_{max}$.

As before, the solid magenta circle indicates the critical point beyond which we have to place restrictions on the ϕ degree of freedom. As we increase θ, the dashed magenta circle increases and C travels along the circumference of the DPT (black half-circle with center M), starting at B and ending at the intersection of the DPT with the projection of the final aperture, X.

In order to determine an expression for ϕ we again want to use the cosine rule on the triangle COM. We therefore define the following lengths:

$$\begin{aligned}AM &= 2.5 + h\\ AO &= 28\left(\frac{2.5+h}{168}\right) = \frac{2.5+h}{6}\\ OC &= 28tan(\theta)\end{aligned} \tag{A.5}$$

and hence

$$OM = AM - AO = \frac{25}{12} + \frac{5h}{6}. \tag{A.6}$$

Via the cosine rule, we obtain

$$\begin{aligned}\widetilde{\phi}(\theta, h) &= \arccos\left(\frac{OM^2 + OC^2 - CM^2}{2OMOC}\right)\\ &= \arccos\left(\frac{\left(\frac{25}{12} + \frac{5h}{6}\right)^2 + (28\tan(\theta))^2 - 2.5^2}{56\tan(\theta)\left(\frac{25}{12} + \frac{5h}{6}\right)}\right).\end{aligned} \tag{A.7}$$

The fraction of atoms passing through the differential pumping tube therefore takes the following form:

For BM$\geq$OM:

$$p(h) = \begin{cases} \frac{1}{\pi W}\left(\int_0^{2\pi} d\phi \left(\int_0^{\arctan(\beta)} d\theta \sin(\theta) j_{q\leq 1}(\theta) + \int_{\arctan(\beta)}^{\arctan\left(\frac{h}{168}\right)} d\theta \sin(\theta) j_{q\geq 1}(\theta)\right)\right. & \\ \left. + \int_{-\phi(\theta,h)}^{\phi(\theta,h)} d\phi \int_{\arctan\left(\frac{h}{168}\right)}^{\arctan\left(\frac{5-h}{168}\right)} d\theta \sin(\theta) j_{q\geq 1}(\theta)\right) & \text{if } \beta \leq \frac{h}{168} \\ \frac{1}{\pi W}\left(\int_0^{2\pi} d\phi \int_0^{\arctan\left(\frac{h}{168}\right)} d\theta \sin(\theta) j_{q\leq 1}(\theta)\right. & \\ \left. + \int_{-\phi(\theta,h)}^{\phi(\theta,h)} d\phi \left(\int_{\arctan\left(\frac{h}{168}\right)}^{\arctan(\beta)} d\theta \sin(\theta) j_{q\leq 1}(\theta) + \int_{\arctan(\beta)}^{\arctan\left(\frac{5-h}{168}\right)} d\theta \sin(\theta) j_{q\geq 1}(\theta)\right)\right) & \text{if } \frac{h}{168} \leq \beta \leq \frac{5-h}{168} \\ \frac{1}{\pi W}\left(\int_0^{2\pi} d\phi \int_0^{\arctan\left(\frac{h}{168}\right)} d\theta \sin(\theta) j_{q\leq 1}(\theta) + \int_{-\phi(\theta,h)}^{\phi(\theta,h)} d\phi \int_{\arctan\left(\frac{h}{168}\right)}^{\arctan\left(\frac{5-h}{168}\right)} d\theta \sin(\theta) j_{q\leq 1}(\theta)\right) & \text{if } \beta \geq \frac{5-h}{168} \end{cases}$$

For BM≤OM:

$$p(h) = \begin{cases} \frac{1}{\pi W} \int_{-\widetilde{\phi}(\theta,h)}^{\widetilde{\phi}(\theta,h)} d\phi \int_{\widetilde{\theta}_{crit}}^{\widetilde{\theta}_{max}} d\theta \sin(\theta) j_{q\geq 1}(\theta) & \text{if } \beta \leq \frac{5h-2.5}{168} \\ \frac{1}{\pi W} \int_{-\widetilde{\phi}(\theta,h)}^{\widetilde{\phi}(\theta,h)} d\phi \left(\int_{\widetilde{\theta}_{crit}}^{\arctan(\beta)} d\theta \sin(\theta) j_{q\geq 1}(\theta) + \int_{\arctan(\beta)}^{\widetilde{\theta}_{max}} d\theta \sin(\theta) j_{q\leq 1}(\theta)\right) & \text{if } \frac{5h-2.5}{168} < \beta \leq \frac{2.5}{168} \\ \frac{1}{\pi W} \int_{-\widetilde{\phi}(\theta,h)}^{\widetilde{\phi}(\theta,h)} d\phi \int_{\widetilde{\theta}_{crit}}^{\widetilde{\theta}_{max}} d\theta \sin(\theta) j_{q\leq 1}(\theta) & \text{if } \beta > \frac{2.5}{168} \end{cases}$$

Plotting $p(h)$ at $\beta = 0.02, R_{cap} = 100\mu m$ gives:

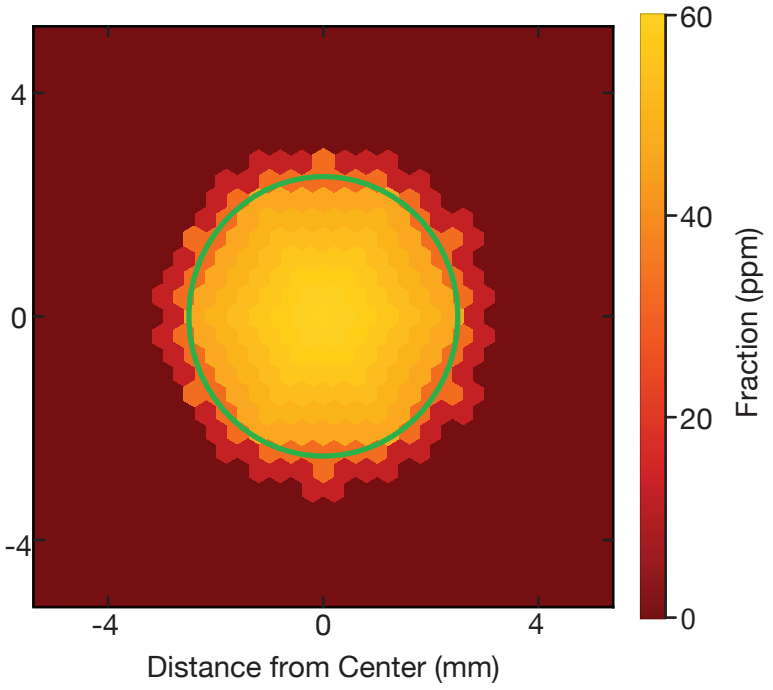

Figure A.4 A density plot showing the fraction of atoms that make it through the differential pumping tube, whose front face is indicated by the green circle. As expected we observe a steep decline in the atomic fraction beyond the edge of the differential pumping tube. From this we can conclude that a nozzle larger than the diameter of the differential pumping tube does very little to increase the flow of usable atoms.

As we would expect, there appears to be a steep drop in the fraction of atoms for values of h beyond the boundary of the DPT (indicated in the right-hand side plot by the green circle).

Using our previous capillary model, we calculate a total capillary number of 768, which in turn gives a total fraction of $\approx 0.105\%$ With this fraction we calculate the flow-rate after the DPT to be:

$$\Phi_{TC} = 0.00105 \times \Phi_{tot} \approx 4.9 \times 10^{12} \text{atoms/s}. \tag{A.8}$$

Increasing the value of β has the effect of decreasing the maximum fraction and of flattening the distribution into a 'top-hat' shape. This is consistent with our intuition, since for an increasing aperture size (or decreasing tube length), the probability of atoms closer to the edge of the tube making it through the aperture increases. It is also worth noting that Φ_{TC} is independent of the number of capillaries in the nozzle, since $p_{tot} \sim \frac{1}{N_{cap}}$ and $\Phi_{tot} \sim N_{cap}$.

Appendix B

ECDL Mode-Hop Free Tuning Range

Initially, the mode-hop-free tuning range of our linear ECDL was limited to ≈ 1.2 GHz. Upon checking the feedforward and piezo offset on our scan control independently, we realized that these two variables were working against each other, that is to say, the feedforward was shifting the internal modes of LD in such as way as to oppose the movement of the external cavity modes caused by tuning the piezo offset voltage. This is a consequence of the Toptica Scan control which is designed for a range of Toptica lasers in the Littrow configuration. We assume, that the piezo in these Littrow lasers is mounted behind the grating, such that an expansion of the Piezo causes a contraction of the external cavity (rather than an expansion as in our linear laser design).

Here we would like to gratefully acknowledge Dr. Ahmed Omran, who discovered this problem after an afternoon of work on our laser and who promptly suggested the following solution: Since we needed to reverse the polarity of the feedforward signal and the scan control had no external switch for this purpose, we decided to extract the feedforward signal via the analog interface, invert it and feed it back directly into the current modulation input of the current control unit. For this we also disabled the internal feedforward from the scan control to the current control.

This was done by changing the jumper setting on the analog interface to take the feedforward signal from the scan control unit. The factory default channel for this signal is specified as "DA#0".

Next we disabled the internal connection between the scan control feedforward signal and the current control unit. This was done by removing the jumper from the "DA#0" channel on the current control board.

Finally, we needed to invert the signal. This was done by simply feeding the signal into an inverting op-amp (OPA 211) with a gain of one. For this purpose we used one of our summing amplifier boards, but left out one of the two op-amps. We also looked for an alternative solution on the board of the scan control unit. However, a simple flipping of the feedforward sign switch had no effect.

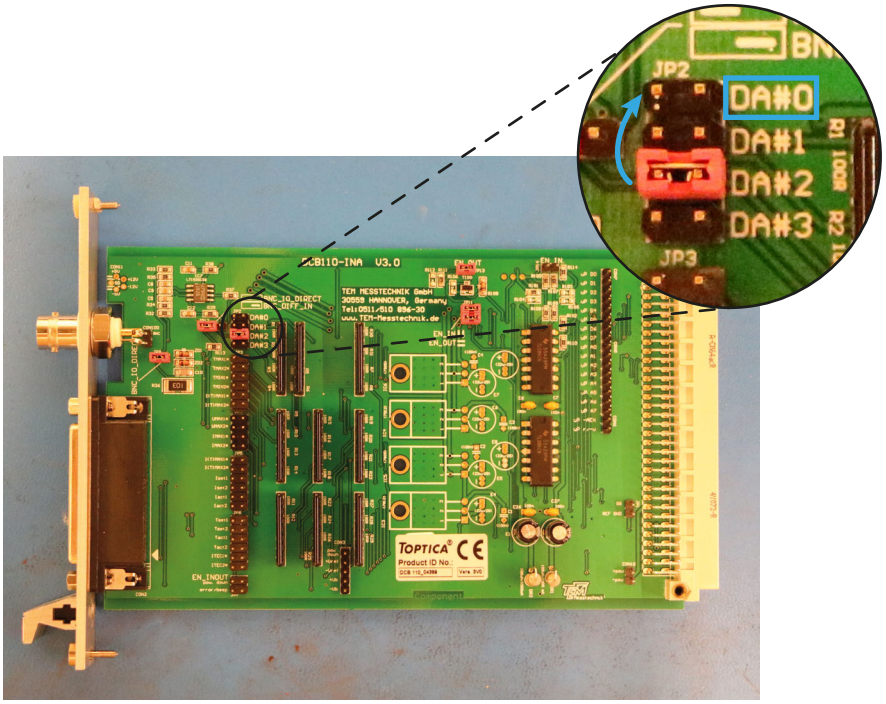

Figure B.1 Changing the jumper on the analog interface board of a Toptica DL Pro from "DA#2" to "DA#0".

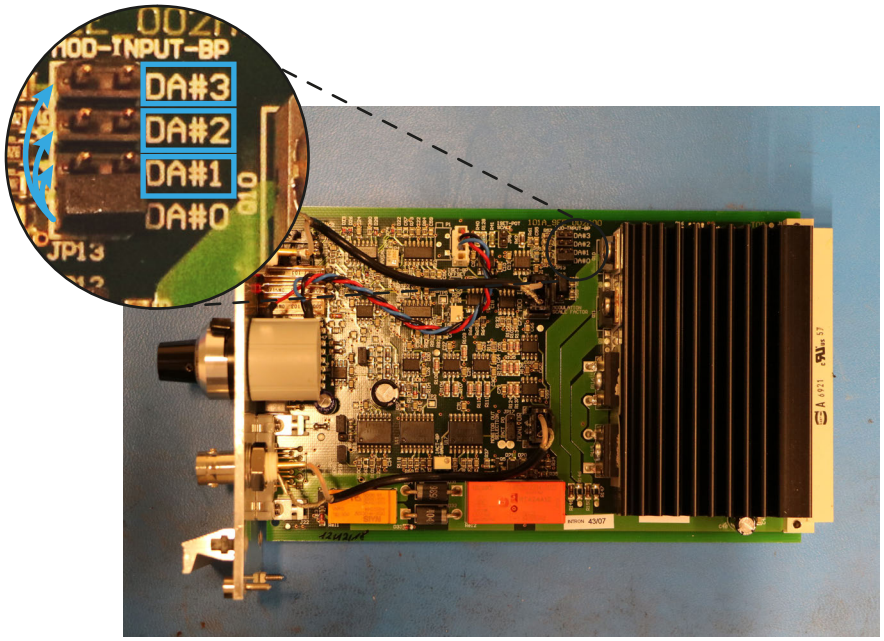

Figure B.2 Removing the jumper on the current control board of a Toptica DL Pro from the "DA#0" position.

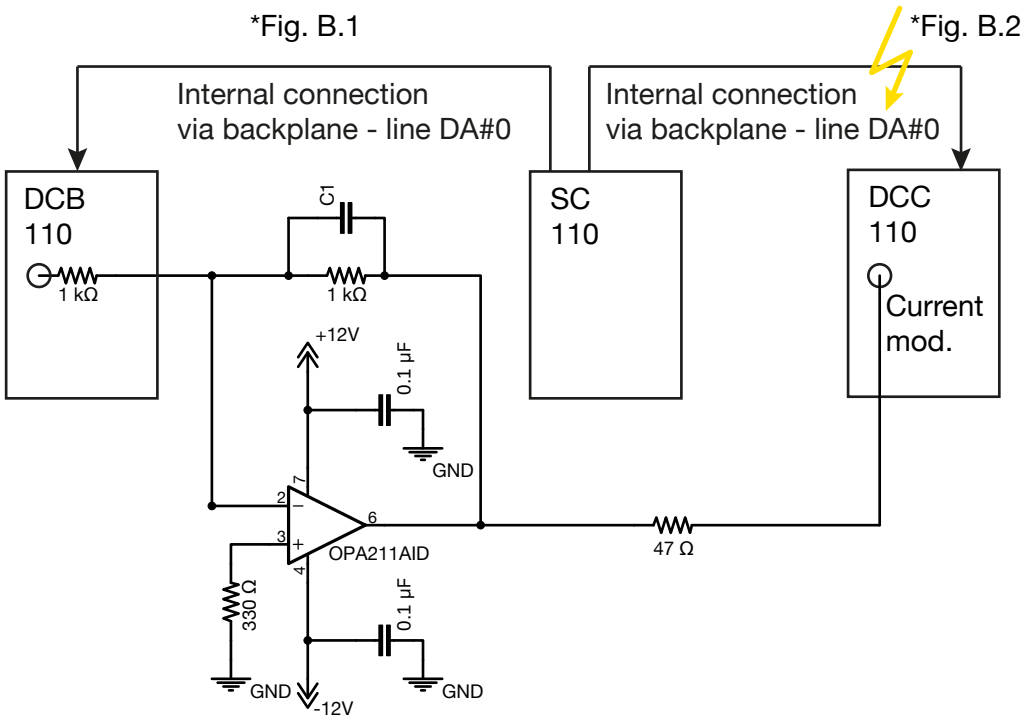

Figure B.3 A schematic of our feedforward inversion solution for the optimization of the mode-hop free tuning range of our linear ECDL.

Appendix C

ECDL Parts List

Table C.1 A table containig all non-standard, commercially available parts necessary to build a linear ECDL at 461 nm.

Type	Part Name	Quantity	Manufacturer	Part Number
Electronics	Peltier element	2	RS	490-1480
	Piezo ring chip	1	Piezomechanik GmbH	HPCh 150/15-8/3
	10 kΩ NTC Thermistor	1	EPCOS	B57861S0103F040
Optics	Aspheric lens	2	Thorlabs	C280TMD-A
	Laser diode	1	Nichia	NDB4216
	Laser diode collimator	1	Schäfter-Kirchhoff	20C-A4.5-03
	Interference filter	1	Iridian	473 nm BPF
	Vertical drive mount	2	Newport	HVM-05R
	Wedged Window	1	Thorlabs	WW11050-A

Eidesstattliche Erklärung

Erklärung:

Hiermit erkläre ich, die vorliegende Arbeit selbständig verfasst zu haben und keine anderen als die in der Arbeit angegebenen Quellen und Hilfsmittel benutzt zu haben.

_____

München, Datum der Abgabe

_____

Unterschrift